Final Report
Rohini International Subcontract
WPAFB Contract Number: F33615-96-C-3204
Georgia Tech Project Number: E16-N32

F-15 TAIL BUFFET ALLEVIATION: A SMART STRUCTURE APPROACH

By

School of Aerospace Engineering
Georgia Institute of Technology
Atlanta, Geogia 30332

Principal Investigator: **S. Hanagud, Professor**
hanagud@ae.gatech.edu

DISTRIBUTION STATEMENT A
Approved for Public Release
Distribution Unlimited

19990719 197

DTIC QUALITY INSPECTED 4

Home of the 1996 Olympic Village
Georgia Institute of Technology

Office of Contract Administration
Contracting Support Division
Atlanta, Georgia 30332-0420 U.S.A.
PHONE 404•894•6944
FAX 404•894•5285

December 2, 1998

In reply refer to: E-16-N32

Dr. S.K. Nagaraja
Rohini International
3354 South Field Drive
Beavercreek, OH 45434-5752

Subject: **Final Report**
Project Director(s): **Dr. Sathyanaraya Hanagud**
Telephone No.: **(404)894-3040**
Contract No.: **AGREEMENT DATED 18 NOV 1997**
Prime No.: **F33615-96-C-3204**
Period Covered: **960619 through 981031**

The subject report is forwarded in conformance with the contract/grant specifications.

Should you have any questions or comments regarding this report(s), please contact the Project Director or the undersigned at 404-894-4764.

/TW

Sincerely,

Wanda W. Simon /TW
Wanda W. Simon
Reports Coordinator

Distribution: **1 copy**

Executive Summary

I Introduction-Background
I.1 F-15 Aircraft
I.2 First Vertical Tail
I.3 F-15 Vertical Tail Problems and Solutions
I.4 Analysis of F-15 Vertical Tail Design Modifications
I.5 Effect of Tail Buffet
I.6 Tail Buffet Alleviation
I.7 Smart Structure Approach to Tail Buffet Alleviation

II Objectives

III Development of Mathematical Models
III.1 Model Reconstruction from Experimental Modal Analysis (EMA) for Noise Control

IV Choice of Actuator
IV.1 Piezoceramic Stack Actuators for Vibration Control
IV.2 Model of a Fixed, Mass-Spring Piezoceramic Stack using Modal Expansion

V Curvature Modal Survey for Optimal Actuator Placement

VI Acceleration Feedback Control Compensators Designs
VI.1 Single Degree Of Freedom Representation of the Acceleration Feedback Control
VI.2 Cross-Over Design for the Compensator Parameters
VI.3 H_2 Optimal Design for the Compensator Parameters
VI.4 Validation of the $\omega_C = \omega_S$ Assumption
VI.5 Multi-Mode Acceleration Feedback Control With a Single Actuator

VII Validation on Vertical Tail Sub-Assembly
VII.1 Plant Model for the Vertical Tail
VII.2 Vertical Tail Acceleration Feedback Controller Design
VII.3 Experimental Setup for the Acceleration Feedback Control of the Vertical Tail Sub-Assembly
VII.4 Results

VIII Structural Dynamic Scale Model, Finite Amplitude Vibration Control and Nonlinear Effects
VIII.1 One-Sixteenth Structural Dynamic Scale Model Construction
VIII.2 Finite Amplitude Vibration Control of the 1/16 Scale Model under Excitations due to Air Flow
VIII.3 Nonlinear Studies

IX Aeroelastic Scale Model Design and Construction
IX.1 Rigid Body Part of Scale Model: Fuselage and Wings

IX.2 Frequency Matched Model (1 to 1 frequency ratio)
IX.3 Froude Scale Model (4 to 1 frequency ratio)
IX.4 Final Assembly
IX.5 Structural Integrity Test

X Wind Tunnel Tests for Control Authority Study
X.1 1/16th Scale Model Installation in the Wind Tunnel and Experimental Setup
X.2 Study of the Buffet Effects on the Vertical Tails
X.3 Instrumentation for Estimating the Control Authority Needed
X.4 Experimental Investigation of the Control Authority Needed to Alleviate the Buffet Induced Vibrations

XI Wind Tunnel Tests for Active Tail Buffet Alleviation
XI.1 Design and Building of Final Aeroelastic Scaled Model
XI.2 Wind Tunnel Validation of the New Scaled Model
XI.3 Control Sensor Placement
XI.4 Wind Tunnel Buffet Response Study
XI.5 Actuators Placement and Mounting
XI.6 Control Plant Model and Control Parameters Extraction
XI.7 Actuator Arrays Authority Assessment
XI.8 Control Design using Acceleration Feedback Control
XI.9 Controller Implementation using a Digital Signal Processor
XI.10 Active Buffet Alleviation Validation

XII Conclusions

Appendix 1: References

EXECUTIVE SUMMARY

EXECUTIVE SUMMARY

1. Introduction

In high performance twin-tail aircraft fighter aircraft (HPTTA), tail buffet was first noticed through its destructive effects of induced fatigue cracks in the F-15 aircraft. The fatigue cracks were noticed shortly (less than six months) after the F-15 was placed in service and many high angles of attack maneuvers were executed. After repeated temporary structural fixes, a thorough investigation of the conditions leading to the crack confirmed that tail buffet is the cause of these effects. There are two significant effects of the buffet induced tail vibrations. These vibrations can restrict the flight maneuvering capability by restricting the angles of attack and speeds at which maneuvers such as the wind-up and wind-down turns can be executed. The second effect is caused by fatigue cracks and the resulting corrosion due to moisture absorption through the cracks. Because of this, a significant amount of maintenance efforts are spent on the F-15 vertical tails in logistic centers like the Warner-Robins Air Logistics Center.

W-RALC processes about 90 to 120 F-15s per year, 80% of which show vertical tail damage. In addition to this normal maintenance, about one-fourth to one-third of all structural trouble reports on the F-15 involve vertical tail cracking. Repairing each vertical tail costs $28K in-house and $50-70K under contract. Some vertical tails cannot be repaired; about 5 or 6 tails are completely replaced each year, at $400K each. The total cost of repairing and replacing the F-15 vertical tails due to fatigue damage is therefore about $5-6M per year, in addition to the loss of flight readiness to the Air Combat Command.

As a result, the effect of buffet-induced vibrations of the fins of HPTTA has been studied by many researchers. Tail buffet occurs when unsteady pressures associated with separated flow excite the changing modes of the vertical fin structural assemblies. This type of buffet is severe during high angle of attack maneuvers such as the wind-up and wind-down dog-fighting maneuvers. At high angles of attack, flow separates at the leading edge of the wings and is convected by the geometry of the wing-fuselage interface toward the vertical tails. This phenomenon, along with the aeroelastic coupling of the tail structural assembly, results in vibrations that can shorten the fatigue life of the empennage assembly and limit the flight envelope due to the large amplitude of the fin vibrations.

The set of high performance twin-tail aircraft includes the F-14, F-15, F/A-18, F-22 and F-117. Most of these aircraft must maneuver at high angles of attack to perform their roles. However, since the characteristic of the separated flow depends upon the geometry of the wing, the fuselage and the empennage, different kinds of tail buffet exist. Vibrations of the vertical tails of the F/A-18 are attributed to broadband excitations resulting from the bursting of strong vortices. On the other hand, the tail buffet problem of the F-15 is associated with a separated flow containing a narrow band of frequencies that engulfs the tail assembly. This narrow band of frequencies contains the frequency of the first torsion mode of the vertical tails. Finally, it has been shown during this project that, in some cases, the buffet phenomenon can include both aerodynamic and structural nonlinear effects.

2. Tail Buffet Alleviation

Many different approaches to tail buffet alleviation of HPTTA have been investigated. Some of the approaches, such as wing leading edge blowing or adding fences on the wings, or on the fuselage, are related to flow control. Other approaches to addressing the problems are through structural passive designs. Examples of such approaches include the reinforcement of the fin assembly with patches, both to repair existing defects and to stiffen the assembly, or the introduction of passive damping materials in the design of the vertical tails. Finally, more recently, active structural control means have been investigated. A combination of advanced feedback controllers and the use of the rudders was first evaluated. Nowadays, techniques based on smart structure concepts, which use active structural actuators, such as piezoceramic wafers or stack assemblies, and controllers, are leading in this area.

The objective of this work is to describe the results of our work in the area of buffet alleviation by the use of piezoceramic stack actuator assemblies.

3. Models for Controller Designs

To develop active vibration controllers for a given structure, we need a mathematical model to represent its structural dynamic behavior. In control terminology, this mathematical model is also known as the "Plant Model". Depending on the procedure used for the design of the controllers, the plant model can be:

A finite element model in the configuration space:

$$M\ddot{x} + C\dot{x} + Kx = f \qquad (1)$$

A finite element model in the modal space:

$$\ddot{\xi} + \text{diag}(2\zeta_i\omega_i)\dot{\xi} + \text{diag}(\omega_i^{\,2})\xi = F \qquad (2)$$

A finite element model in the state-space:

$$\dot{x} = Ax + Bu \qquad (3)$$

Or a transfer function matrix model:

$$\bar{x} = [TF]\bar{f} = (s^2M + sC + K)^{-1}\bar{f} \qquad (4)$$

Our objective is to design vibration controllers that can reduce the amplitude of vibration in the range of 8 to 80Hz. We would like to provide a selected amount of damping in the closed loop by using active control techniques that use piezoceramic stack actuator assemblies. On the basis of our preliminary work in Phase I, we would like to design acceleration feedback controllers with actuators placed at optimal locations. The desired plant model is the modal space model, equation 2, or the transfer function matrix model. equation 4.

NASTRAN Finite Element Model

For the F-15 vertical tail sub-assembly, a NASTRAN finite element model was initially used. This model had 600 nodes and approximately 32,000 degrees of freedom. The types of elements used in the model were QUAD4, SHEAR, CONROD, TRIA3, rigid elements, non-structural masses and many spring supports. The model was originally developed to calculate stresses in the forward box near the tip pod. A fine mesh was created in that region which resulted in the very large number of degrees of freedom. The model has the form:

$$[M]\{\ddot{x}\}+[K]\{x\}=\{f\} \qquad (5)$$

The model is not ideally suited for designing smart structure based vibration controllers. The model does not provide the damping matrix [C]. In real life, no two vertical tails have the same natural frequencies and mode shapes. Thus, the model, to be used in the controller design, should accommodate these changes with relatively little effort.

Bu using the NASTRAN model and appropriate truncation procedures, we computed the first nine non-zero natural frequencies and their associated mode shapes. The purpose of these calculations was to use these mode shapes, natural frequencies and assumed modal damping to transform equation (5) into a form of equation (2) in the modal space.

Full Scale Tests for Finite Element Validation and Updating

To validate the NASTRAN finite element model, tests were then performed on a full scale F-15 aircraft to obtain an experimental representation of the structure. This modal test was performed using multiple shaker locations and 37 nodal locations on the left vertical tail plus a few on other parts of the aircraft. The results include the natural frequencies, ω_i, the mode shapes, ϕ_i, and the modal damping ratios, ζ_i.

These experimental results did not agree closely with the finite element model. By tweaking the model with non-structural masses and springs, very good agreements between the experimental natural frequencies and the ones from the NASTRAN finite element model results were not obtained.

Experimental Modes, Frequencies and Damping Models

The next step in the model development was to use the experimentally identified modes, natural frequencies and damping ratios as well as a reliable mass matrix of the structural system to develop a mathematical model in the form of equations (1) or (2) to design the active vibration controllers. Repeated experimental modal testing on a full-scale aircraft was not possible in the program because of the cost and the availability of the F-15 aircraft.

However, a full-scale laboratory vertical tail sub-assembly of the F-15 aircraft was available to us at Georgia Tech. This vertical tail assembly consisted of one vertical tail, one horizontal tail and a part of the aft-fuselage. The assembly was mounted on a specially designed framework and supports. These supports were designed such that the natural frequencies and mode shapes of the laboratory sub-assembly were nearly the same as those obtained during the full-scale aircraft tests.

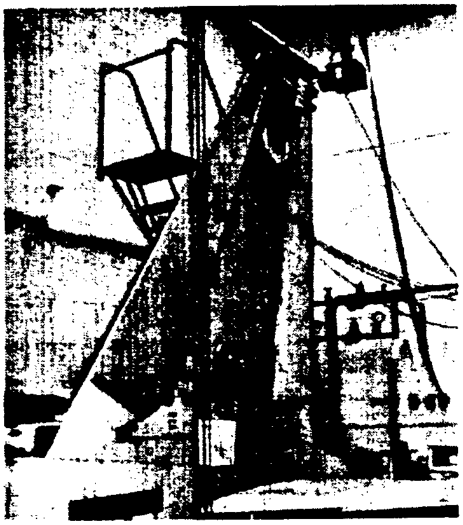

Figure 1. Vertical Tail Sub-Assembly

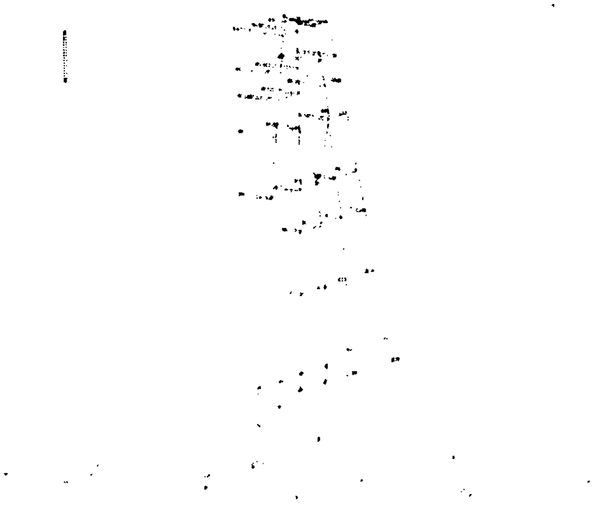

Figure 2. Mode Shape of the First Bending Mode of the Laboratory Vertical Tail Sub-Assembly

Detailed experimental modal analysis of the laboratory vertical tail sub-assembly was performed. During this test, a 25-pound-force shaker was attached to the outboard trailing edge of the tip of the vertical tail and 41 sensor locations were selected for the vertical tail, in addition, nine locations were also selected on the horizontal tail.

From this experiment, we obtained a new experimental model for the vertical tail in the form of a transfer function vector yielding the natural frequencies, the mode shapes and the damping ratios of the sub-assembly. The first 14 modes of the structure were obtained so that a 14 by 41 mode shape matrix was available. Using the mass data from the original NASTRAN finite element model and reducing it to the 41 experimental nodal coordinates, experimentally recomposed stiffness and damping matrices were developed based on the procedure described in Appendix 2. As a result, we obtained three types of models, similar to equations (1), (2) and (4), from the experimental data and the original NASTRAN finite element mass matrix.

These models are used in the design of our active vibration controller. For future work in buffet vibration control and buffet load predictions, it is desirable to have a reliable structural dynamic finite element model instead of the current stress model. The model should be able to yield reasonably accurate natural frequencies and mode shapes. Furthermore, the mode should be easily modifiable to accommodate for different F-15 vertical tail sub-assemblies. Such model can be developed using MATLAB, ANSYS, ASTROS or NASTRAN.

4. Actuator and Actuator-Assembly Choice: Piezo-Stack Actuators.

The selection criteria for the choice of a piezoelectric actuator usually involve mechanical properties, electrical properties and cost. For the purpose of alleviating the buffet-induced vibrations on an HPTTA, the primary concern is with the control authority that can be generated by the actuator. To obtain maximum control authority, the resultant forces that the actuator develops should be as large as possible. Then, for large amplitude vibration actuation, the elongation properties of the actuator should also be maximized.

Lead zirconate titanate (PZT) ceramic wafers are generally considered for these actuators. However, the control authority of PZT wafer actuators, unless used in large quantities, is usually not sufficient for most real world applications. In addition, in an environment of large amplitude vibrations, the PZT wafer can debond from its host structure. Stack actuators can increase the control authority through a more efficient use of the piezoceramic material properties. This increase is obtained by the use of the longitudinal d_{33} coefficient instead of the transverse d_{31} and d_{32} coefficients generally used with wafers. Furthermore, the increased stack forces result from the addition of the effective piezoelectric reactions by using the accumulation of reaction from each PZT in series and the design of the actuator sub-assembly, as is illustrated by the free elongation ΔL and blocked force, F_b, which are:

$$\Delta L = n d_{33} V \tag{6}$$

$$F_b = n d_{33} V E_{33} L w / h \tag{7}$$

Where d_{33} is the PZT longitudinal piezoelectric charge constant; L, w and t are the length, width and thickness, respectively, of the each piezoceramic element; E_{33} is the longitudinal short-circuit Young's Modulus of the piezoceramic element; V is the voltage applied across the actuator and n is the number of piezoceramic element that form the stack.

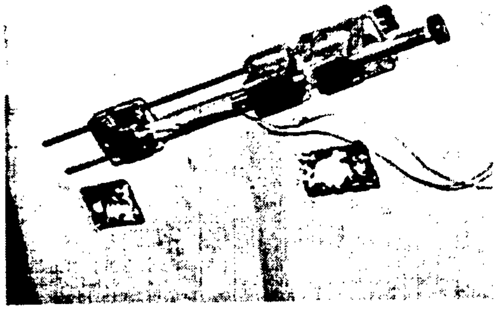

Figure 3. Actuator Assembly

The main challenge, associated with the use of such active elements in alleviating the buffet-induced vibrations on an HPTTA, is that the piezoceramic stack produces only longitudinal motion or forces. An assembly must be designed to transform the longitudinal motion of the stack into moments that will produce the control actuation. Such a transformation can be achieved by placing the piezoceramic stack parallel to the controlled structure at a distance from its neutral axis and at a selected orientation. This distance will create a lever arm so that the longitudinal forces will result in local moments on the structure. The resulting assembly is illustrated by figure 3.

5. Actuator Placement (Curvature Modal Survey Approach)

The second major task in optimizing the control authority of actuators is the placement of these actuators. The optimization of the actuator locations is obtained by performing a curvature modal survey. The principles of this survey are based on reciprocity theory as illustrated by figure 4. The optimization is performed such that local moment resultants acting on the structure resulting from the piezo-stack actuator assembly produce maximum transverse motion at the sensor location. This survey was performed in two perpendicular directions so that the actuator locations are optimized for both bending and torsion modes.

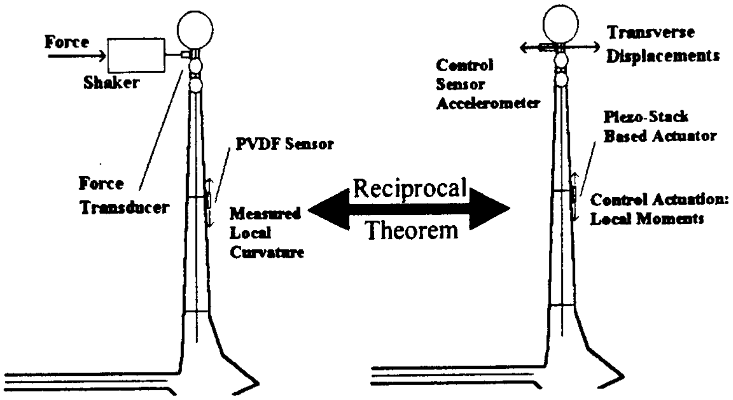
Force
Shaker
Force Transducer
PVDF Sensor
Measured Local Curvature
Reciprocal Theorem
Control Sensor Accelerometer
Transverse Displacements
Piezo-Stack Based Actuator
Control Actuation: Local Moments

Curvature Modal Survey

Control Actuation

Figure 4. Principles of Curvature Modal

6. Controller Design (Acceleration Feedback Control Compensators)

In classical approaches to control of flexible structures, system equations are usually rewritten in a state space domain. But these transformations to state space domain often lose insight into the physics of the problem from the point of view of a structural dynamicist. Furthermore, these representations are not unique. Since the work of Goh and Caughey and the introduction of the PPF controller, which was later experimentally applied to structures using piezoceramic actuators, the second-order compensators enable the designers to keep the system equations of motion in their second order form. But control schemes such as the PPF and the SRF are not unconditionally stable. A second order compensator using acceleration feedback was later developed. The main advantage of this control scheme was its unconditional stability for single degree of freedom systems with collocated pairs of sensors and actuators. Goh and Yan developed a method of assigning the damping ratios and scalar gains to pairs of collocated sensors and actuators.

Then, Bayon de Noyer and Hanagud have shown that the acceleration feedback control can also be applied to non-collocated actuators and sensors. They further developed two methods to obtain the parameters of the compensators for both single mode and multi-mode control using a single actuator, one based on crossover point design and one based on H_2 optimization. Both these approaches are shown to be more effective than the previously proposed designs. Finally, Bayon de Noyer and Hanagud have shown that with a proper choice of compensator design and appropriate selective spillover effects, the coupled controlled dynamic system can be reduced in the modal space into a subset of single degree of freedom uncoupled acceleration feedback controlled modes and a subset of uncontrolled and uncoupled structural vibration modes. As a result, each compensator can be designed independently using a selective single degree of freedom design.

For cases where nonlinear effects are important, the use of either linear controllers or saturation nonlinear controllers are proposed.

7. Validation on Vertical Tail Sub-Assembly

The usefulness of acceleration feedback control and piezo-stack actuator assembly for full-scale structural sub-assemblies was demonstrated with the vibration control of the vertical tail sub-assembly of an HPTTA shown in figure 1. For this experiment, the sensor was located on the inboard trailing edge tip of the vertical tail so that it had a maximum sensing of bending and torsion modes. The piezo-stack actuator assembly was mounted on the inboard side of the tail, at two third of its span, on the leading edge side of the elastic axis.

The design of the vertical tail vibration controller using an AFC scheme is set up such that it will increase the damping of three modes (i.e. all significant modes between 20 and 80 Hz) using a single actuator. The three modes that are chosen are the first torsion, a plate mode with diagonal node line and the second bending mode of the vertical tail. Each of the compensator is designed independently following the results discussed before. The type of single degree of freedom AFC is chosen to be the crossover design for all three modes.

The compensator parameters are computed with an initial choice of compensator damping ratio of about 10 times the modal damping coefficient of the associated mode of the open loop structure. The results illustrated by figure 5 demonstrate the ability of acceleration feedback control to reduce the vibrations in multiple modes using a single piezo-stack actuator assembly by as much as a factor of ten.

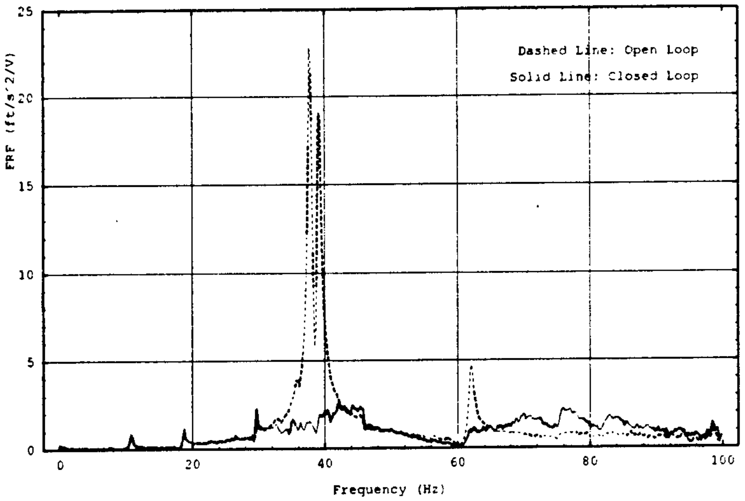

Figure 5. Comparison of Experimental Open and Closed Loop Transfer Functions

8. Wind Tunnel Tests for Control Authority Study

To validate the use of AFC in reducing the buffet-induced vibrations of the vertical tails of an HPTTA, a 1/16th-scale wind tunnel model, shown on Figure 6, was designed and built. This model consisted of a rigid fuselage and wings with an aeroelastically scaled empennage. Two arrays of piezoceramic wafers were bonded on both the scaled vertical tails. For each tail, the first array was located at its root to control the bending modes. This array was made of two pairs of piezoceramic wafers in a bender configuration. The second array was optimized to control the torsion modes and was located above the first array. This array was made of a pair of piezoceramic wafer in bender configuration. Finally, an accelerometer was mounted on the inboard trailing edge of the tip of each vertical tail. Figure 7 illustrates the configuration of the wind tunnel model.

To determine the modes that should be controlled on the 1/16th scale model, a wind tunnel experiment was designed. This experiment was performed with the wind tunnel dynamic pressure set at q = 7 psf and the scale model was mounted at an angle of attack $\alpha = 22°$. The results of this experiment demonstrated that modes with frequencies between 25 and 90 Hz are dominant, as is illustrated by figure 8. These correspond to the first torsion mode, a plate mode with diagonal node line and the second bending mode. The first bending mode has a natural frequency below the range of dominant frequencies. However, this mode was also considered in the active vibration control experiment.

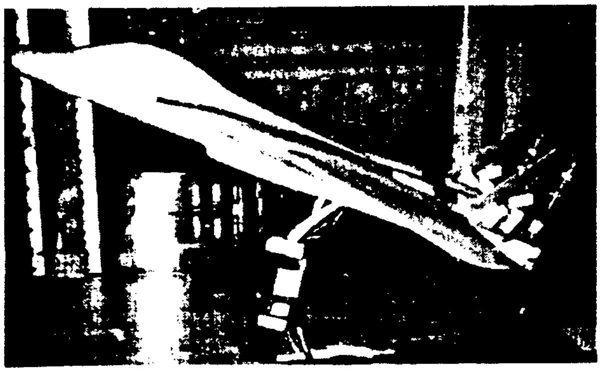

Figure 6. 1/16th Scale Model of the HPTTA mounted in the Wind Tunnel

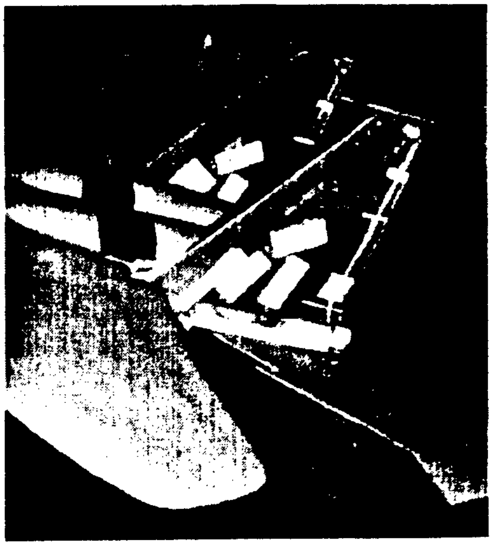

Figure 7. Instrumented Vertical Tails Mounted on the Scale Model

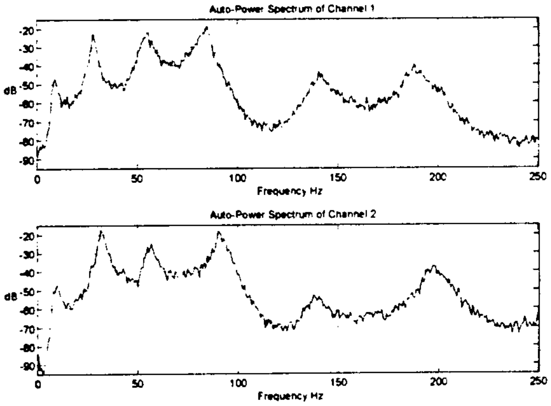

Figure 8. Auto-Power Spectrums of the Left Vertical Tail (Channel 1) and Right Vertical Tail (Channel 2) at q = 7 psf and α = 22°

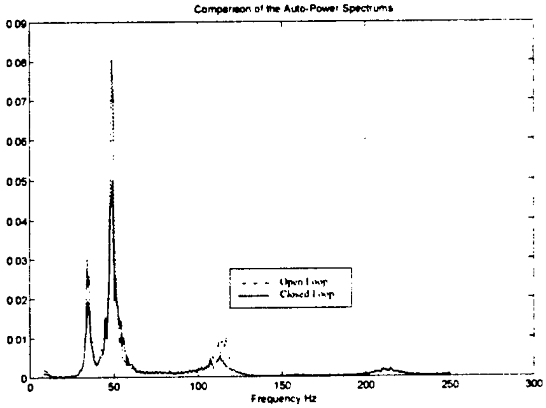

Figure 9. Comparison of Open Loop and Closed Loop Auto Power Spectrum of the Acceleration of the Tip of the Vertical Tail

The next task was to proceed with a buffet alleviation experiment using AFC. It was decided to control the left vertical tail only to assess the control authority needed to alleviate the vibrations induced by the buffet flow in the first four modes of that vertical tail. The first and fourth modes were controlled using the actuator array at the root and the second and third modes were controlled using the upper wafer pair.

First, the transfer function between the lower array and the accelerometer mounted on the inboard trailing edge tip of the vertical tail was determined. Then, a controller was designed with two compensators in parallel. Each compensator follows the theory of AFC with a crossover point based design. Once this control was designed, it was implemented with no airspeed. Then, a second transfer function was obtained by vibrating the vertical tail using the upper actuator pair while controlling the first and fourth modes with the lower wafers. This transfer function was taken between the upper piezoceramic actuators and the accelerometer sensor. Also using AFC with cross-over condition, a controller was designed to damp the vibrations of the second and third modes. Then, both controllers were implemented simultaneously without any airspeed.

These controllers were designed such that the amplitude of reduction in each mode would be about a factor of two. The result of the wind tunnel validation of these controllers at a dynamic pressure of $q = 7$ psf is shown on figure 9. For this experiment, the model was mounted at a 22° angle of attack. All four controlled modes were reduced by a factor close to two. The maximum voltage at the input of the piezo driver was reached more than once during the experiment.

9. Wind Tunnel Tests for Active Tail Buffet Alleviation

Results from our control authority wind tunnel tests, MacAir experiments reported by Triplett and earlier Georgia Institute of Technology tests reported by Komerath et al. showed that there exists a characteristic frequency associated with the maximum buffet load and that its associated reduced frequency is constant for every models. Hence, we determined that it was very important for the active tail buffet alleviation tests to scale the model such that the reduced frequencies are conserved. To operate in the middle of the optimal range for the Georgia Tech Research Institute wind tunnel, the scale model of the empennage was designed to have natural frequencies 2.25 time larger than the full-scale tail sub-assembly. This model would then operate at a free stream dynamic pressure of 9 psf to conserve the reduced frequencies of the flow and structure. This dynamic pressure is equivalent to a free stream velocity of 26.9 m/s that translates to a free stream velocity of 191.5 m/s for the full-scale aircraft or about Mach 0.6 at 20,000 ft.

The first task of the wind tunnel tests was to validate our new scaled model. First, buffet load and dynamic response measurements were taken. The results of this experiment showed that the frequency associated with the maximum buffet load evolves linearly with free stream velocity, which confirmed that the reduced frequency associated with the maximum buffet load remains constant. Then, a flow visualization experiment involving tufts attached to the model was performed and showed that seen from the rear a counter-clockwise vortex immersed the left vertical tail with its core outboard of it.

The following task of the tests was to locate the sensor for the control experiments. Three conditions dictated the placement. First, the vertical tails of our model behaves as a cantilever tapered plate. Second, the sensor, which is used for acceleration feedback control, is an accelerometer. Third, minimum flow disturbance should be obtained. As a result, the optimum location for the sensor was on the trailing edge tip of the vertical tail. The placement was validated experimentally to check that all modes in the control range were observable.

The next phase was to determine at which attitude the worse disturbances are encountered. Since we assume linearity of the structure, the dynamic response of the vertical tail was measured instead of the pressure. First, a fine survey was conducted for angles of attack ranging from 0 to 23 degrees, which showed that the angle of attack that displays the maximum tip response is about 20 degrees. Then, a second survey was conducted for different angles of attack and free stream dynamic pressures in the neighborhood of the worse buffet conditions to obtain the buffet dynamic response envelop illustrated by Figure 10.

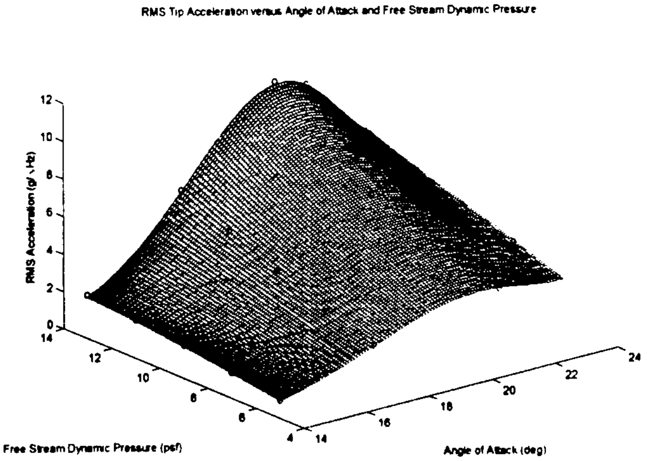

Figure 10. Envelope of Root Mean Square of the Trailing Edge Tip Acceleration versus Angle of Attack and Free Stream Dynamic Pressure.

At this point, the left vertical tail was instrumented with two pairs of piezoceramic stack based actuators. The first pair of actuators was located to obtain large bending actuation authority and was bonded at the root of the vertical tail along its mid-chord line. The second pair of piezoceramic stack actuators was placed for torsion control and was bonded at 35degrees with respect to the mid-chord line above the first pair. This configuration is illustrated in Figure 11.

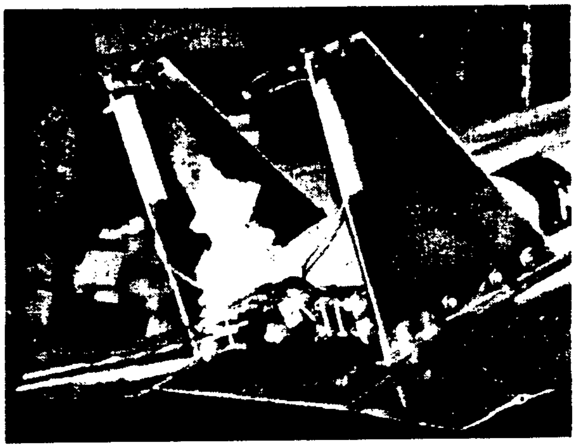

Figure 11. Active Buffet Alleviation Experiment Vertical Tails

The first task associated with designing a controller is to obtain a mathematical representation of the system to be controlled. This representation is usually referred to as a "plant". To obtain the plant model, first experimental transfer functions were obtained between the input voltage to each actuator array and the control sensor response voltage. Then using a combination of system identification techniques such as single pole fitting and complex circle fitting around the poles, the parameters of each of the transfer functions were extracted.

Then, to assess the authority of the actuator arrays, the auto-power spectrum of the dynamic response of the control sensor excited by the buffet vortices was compared with the auto-power spectrums of the actuator arrays converted from experimental transfer functions of the plant for a flat maximum input voltage. This operation showed that enough actuator authority was attained.

Once the plant model has been developed and the actuator authority checked, the controllers themselves must be designed. For this experiment, the type of controller that was selected was acceleration feedback control (AFC). And the type of design for AFC that was retained was the H_2 optimal design. Two different controllers were designed, one for the bending array and one for the torsion array. A single degree of freedom compensator was designed for each mode using the parameters extracted earlier. Since only one parameter is needed for each compensator. In order to avoid clipping of the control signal, the damping of each compensator was chosen to be seven times larger than the damping of the associated mode. Once the controllers were designed, their stability and effects on other modes were checked using root locus plots. Since root locus plots did not show any instability and each controller did not affect the parameters of the other controller, the controllers could be implemented simultaneously.

The controllers are implemented on a dSPACE system based on a digital signal processor (DSP). The coding of the overall control experiment is done using block programming with the Matlab extension called Simulink. The file is then converted to the DSP machine language and downloaded to the dSPACE system. Once the system starts, the controllers are active.

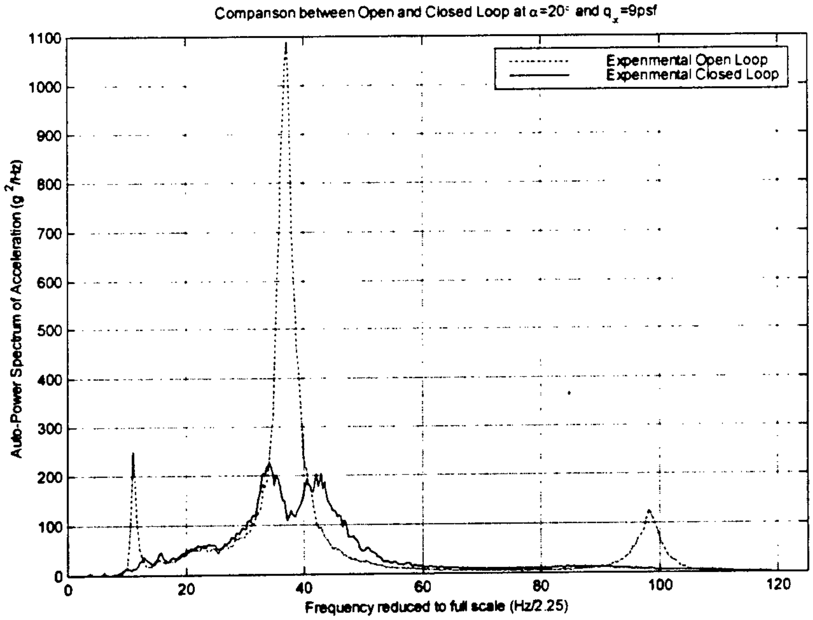

Figure 12. Comparison Between Open and Closed Loop Auto-Power Spectrum of Trailing Edge Tip Acceleration at $\alpha=20°$ and $q_\infty=9$psf.

To validate the controllers, three different experiments were carried out. First, a control experiment was run at the predetermine operating condition of 20 degrees angle of attack and 9 psf of free stream dynamic pressure. The auto-power spectrums of the uncontrolled and controlled trailing edge tip acceleration are illustrated in Figure 12. This figure shows that each of the controlled frequency has its auto-power spectrum reduced by a factor of at least 5. Furthermore, in the case of the first bending mode and second torsion mode, the responses are suppressed to a level equivalent to the one that would be obtained in the absence of the modes.

Once the controller had been validated at its operating point, its effectiveness had to be checked at different conditions. For the second experiment, the operating free stream dynamic pressure of 9 psf was kept. However, the angle of attack was varied from 0 to 23 degrees. This control experiment showed that the root mean square of the trailing edge tip acceleration was reduced by up to 30% below 15 degrees and by about 20% at 20 degrees. This experiment also showed that the controllers were effective on the whole range of angles of attack.

Finally, four different angles of attack were selected. 14, 17, 20 and 23 degrees angles of attack cover the different regimes that the scaled model was encountering. For each angle of attack, the free stream dynamic pressure was varied from 5 to 13 psf. As before, the results showed that as the disturbance increases the effectiveness of the controllers decreases. However, even at a free stream velocity 25% higher than the operating free stream velocity, the minimum RMS reduction was still 17%. These results prove that the controllers were stable and effective over the full buffet domain which means angles of attack ranging from 14 to 23 degrees and free stream velocity ranging from –25% to +25% of the full-scale equivalent to Mach 0.6 at 20,000 ft.

I. INTRODUCTION - BACKGROUND

I.1. F-15 Aircraft

Currently, there are several high performance twin-tail aircraft in operation. Some of the well-known twin tail aircraft are F-15, F-18 and F-22. The capability of these aircraft to perform wind-up and wind-down turns is a very desirable feature of these aircraft. During a wind-up or wind-down turn, these aircraft are subjected to very high angles of attack. From the point of view of the performance of the aircraft, it is very desirable to have a wide range of high angles of attack that the aircraft can sustain. F-15 was one of the aircraft that offered high angle of attack performance in early seventies.

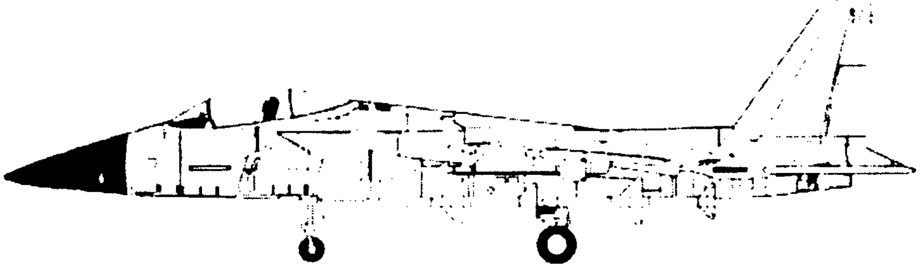

Figure 1.1. Side View of the F-15 Aircraft

The history of F-15 (Figure 1.1) can be traced back to the developmental funding by the Unites States Air Force to Fairchild Hiller, McDonnell Aircraft Company (Mc-Air) and North American Rockwell Corporation during 1965. In 1969, Mc-Air was selected to provide 20 F-15A and two TF-15 aircraft. The first flight of F-15A was on 27th July 1972. The first F-15A was delivered to the Luke Air Force base during late 1974. In 1979, F-15C and F-15D with improved gross weight design, were initiated. The design and development of the F-15E, with improved fuel capacity and fatigue life, was initiated during 1984. Currently there is a very large number (over 2,000) number of F-15 series of aircraft in operation around the world.

I.2. First Vertical Tail

The design of the F-15 vertical tail was initiated during 1970. The F-15 vertical tail configuration is shown in Figure 1.2. The structural details are as shown in Figure 1.3.

Each vertical tail consists of a forward box, an upper aft box, a rudder and a tip pod. The forward box and lower aft box are made of aluminum skin and aluminum honeycomb core with an aluminum closure. The torque box structural components include boron-epoxy skins over aluminum honeycomb core enclosed in titanium forward and rear spare. The upper aft box is made of a rib-skin structure of aluminum alloy with tail lights and antenna assembly.

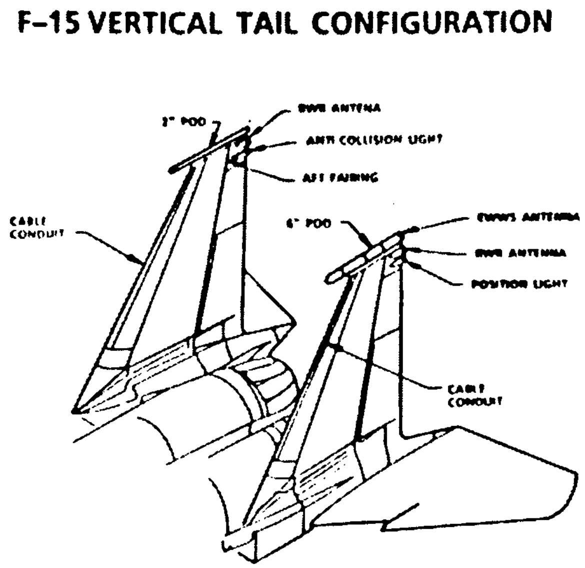
F-15 VERTICAL TAIL CONFIGURATION
3" POD
RWR ANTENA
ANTI COLLISION LIGHT
AFT FAIRING
CABLE CONDUIT
6" POD
EWWS ANTENNA
RWR ANTENNA
POSITION LIGHT
CABLE CONDUIT

Figure 1.2. F-15 Vertical Tail Configuration

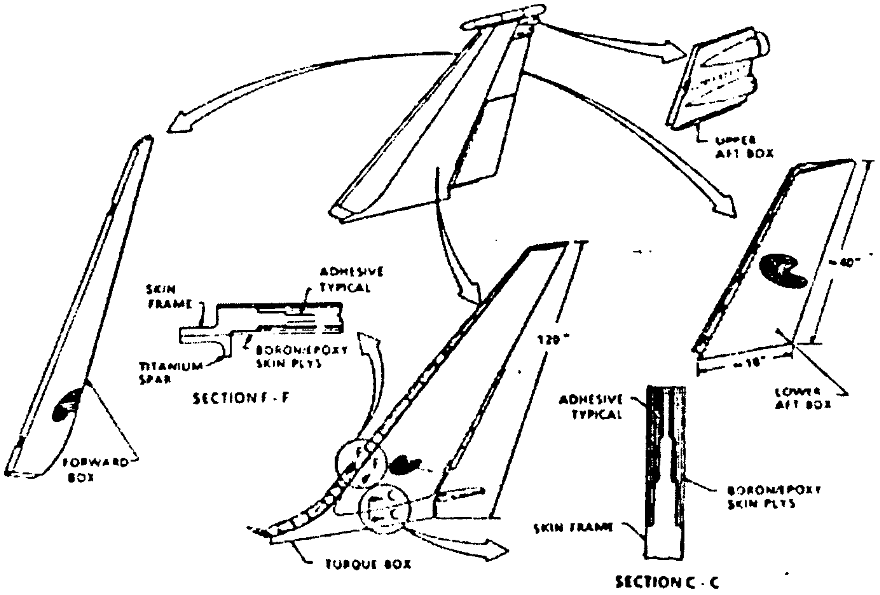
UPPER AFT BOX
ADHESIVE TYPICAL
SKIN FRAME
BORON/EPOXY SKIN PLYS
TITANIUM SPAR
SECTION F - F
120"
~40"
~18"
LOWER AFT BOX
FORWARD BOX
F
F
C
C
ADHESIVE TYPICAL
BORON/EPOXY SKIN PLYS
SKIN FRAME
TORQUE BOX
SECTION C - C

Figure 1.3. Details of the F-15 Vertical Tail Structure

I.3. F-15 Vertical Tail Problems and Solutions

The first F-15A was delivered in late 1974. The first fatigue damage was detected in the vertical tail with the two inch tip pod in mid 1975. The damage was in the torque box near the two inch tip pod. This was repaired by strengthening the region. This was followed by the observation and repair of many other fatigue cracks during the next few years. These cracks were located in different areas of the vertical tail assembly. First major design change of the vertical tail was initiated in 1976. Even with the design changes, additional cracks were detected in both vertical tails. This resulted in a major design modification (TCT0 641) in 1980. Even with TCT0 641, new fatigue cracks were observed in the vertical tail of the aircraft. This resulted in another major vertical design modification in 1986 with a predicted fatigue life of 8000 hours. However a fatigue crack was detected in the vertical tail after only 771 hours of operation in Langley Air Force Base. This was followed by the formation of other similar fatigue cracks in the vertical tail.

In 1988, the Air Force requested Georgia Tech to evaluate the cause of the fatigue failure of the vertical tail and suggest solution strategies to solve the problem including the possibility of a re-design of the vertical tail assembly with prescribed specifications. Shortly, thereafter, Mc-Air initiated another major design modification known as the "exo-skin" patch design modification in 1993. The exo-skin design modification also predicted a fatigue life of 8000 hours.

I.4. Analysis of F-15 Vertical Tail Design Modifications

The fatigue damage is the result of vibrations induced in the vertical tail assembly due to air loads. In 1988, two different types of airloads were proposed as candidates for the cause of the fatigue damage. The first was the tail buffet resulting from high angle of attack maneuvers like wind-up turns. The second was the low altitude high Mach number flights. The Georgia Tech analysis concluded that the tail buffet resulting from the high angle of attack maneuver is the most likely cause of the observed fatigue damage in the F-15 vertical tail subassembly.

After narrowing the cause of the fatigue damage, the next Georgia Tech analysis was to explain the cause of fatigue damage sequence from 1975 to 1990. As explained by

Hanagud et al. (1995), all design modifications of the F-15 vertical tail assembly are centered around the approach of modifying the stiffness of the vertical tail structural systems. As is familiar to aerospace structural engineers, the stiffening alone may not solve the fatigue problem if the exciting load spectra is broad enough to excite the structural natural frequencies of the modified vertical tail. In other words, a "stiffening structural modification" can chase the cracks to non-stiffened areas depending on the exciting load frequencies. The design changes that include only stiffness modifications usually move high (fatigue prone) stress areas to regions away from the stiffened areas. This can be considered to be the cause of new fatigue cracks in the F-15 vertical tail assembly following each design change or design modification. This effect is also confirmed by Ferman et al (1993). In this 1993 paper by Ferman et. al describe their exo-skin patch design modification to provide a fatigue life of 8000 hours.

In their paper, Ferman et al. (1993) have discussed flight tests and laboratory tests of the F-15 vertical tail assembly with and without the addition of the exo-skin patch. The stresses in the vertical tail subassembly without the exo-skin patch is defined here as the stress distribution in the base-line or the reference configuration. Test results reported by Ferman et al. (1993) indicate that (Figure 1.4) the stresses in the vertical tail assembly increased from the base-line or reference configuration in regions away from the exo-skin patch that was used to stiffen the vertical tail subassembly.

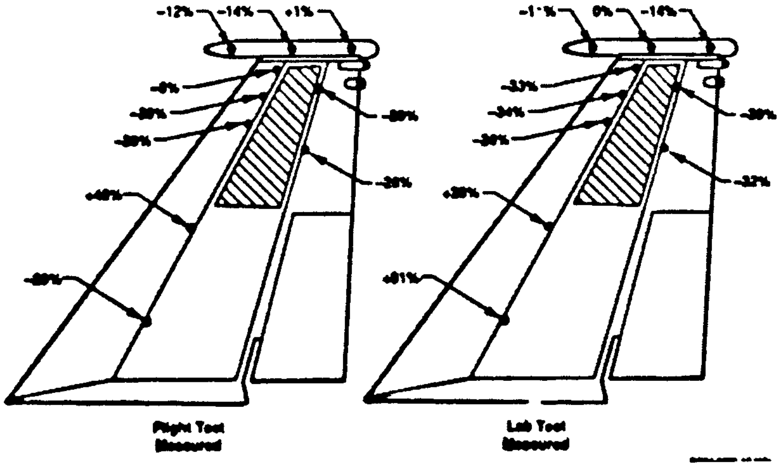

Figure 1.4. Stresses in the Vertical Tail with the Exo-Skin Patch

The changes of natural frequencies due to exo-skin patches are minimal and all new critical natural frequencies are still in the band of frequencies excited by the buffet air loads.

I.5. Effect of Tail Buffet

In summary the F-15 vertical tail subassembly is subjected to oscillating air loads due to buffet during certain high angle of attack maneuvers. The effect of the buffet induced vibrations are the fatigue damage and oscillating control loads developed by the vertical tail. Many design modifications have been introduced to minimize the fatigue damage. All design modifications are based on the concept of increasing the stiffness of the structures locally. These stiffness modifications have resulted in higher stresses in regions of the vertical tail away from the stiffened regions. This has resulted in additional fatigue cracks in different areas of the vertical tail at a small fraction of the projected design life of the vertical tail.

Another effect of the fatigue cracks in the vertical tail is the moisture absorption. The moisture absorption causes the corrosion of the honey-comb structure. As can be seen in Figure 3, the maintenance of the aircraft requires that these honey combs be removed and replaced from the "narrow top" of the forward box. This, very often, forces the replacement of the entire forward box resulting in a significant amount of increase in the cost ownership of the vehicle. The induced fatigue cracks in the lower part of the vertical tail are very critical from the point of view of safety.

The aerodynamic effect of the oscillation of the vertical tail is the oscillating control loads. This results in restriction to the maneuver envelope.

I.6. Tail Buffet Alleviation

As discussed in previous sections, fatigue cracks are observed in the vertical tail subassembly of the F-15 aircraft, at a very small fraction of the projected (or designed) fatigue life of the structure. Theses fatigue cracks are the result of buffet induced vibrations of the vertical tail during high angle of attack maneuvers. Thus, the fatigue life of the vertical tail assembly can be increased and the cost of ownership reduced if the buffet induced vibrations of the vertical tail subassembly are reduced. A reduction of the oscillating of the vertical tail can also improve the maneuver envelope of the aircraft. The buffet induced vibrations of the vertical tail are caused by (a) the oscillating air loads generated during the high angle of attack operations of the aircraft and by the structural dynamic characteristics of the vertical tail subassembly at its supports. Thus the tail buffet effects can be minimized by the following possible approaches.

(1) Flow Control: In this approach, the aerodynamic flow is controlled to change the characteristics of the tail buffet. The objective is to minimize or eliminate the oscillating air loads that excite has usually used (a) passive devices like fences on the wing or the fuselage, or (b) devices to blow at wing leading edges.

(2) Active Flow Control: Another option is the active flow control instead of the passive flow control. Current options are to use smart structure devices (piezoelectric actuators) to achieve a flow that minimizes the oscillating air loads.

(3) Passive Structural Modifications: In this approach, the structural design of the vertical tail subassembly is modified to place the natural frequencies of the structure away from the frequency content of the exciting air loads. The structure is also strengthened to provide a longer fatigue life. Passive damping materials or passive electronics damping can also be incorporated to minimize the buffet induced vibrations.

(4) Active Rudder Control: In this approach, the rudder is oscillated actively to change the characteristics of the flow to minimize the vibrations of the vertical tail subassembly during high angle of attack maneuvers. This approach can also be considered as an "active flow control".

(5) Smart Structures Approach: The buffet induced structural vibrations are actively controlled by the smart actuators like piezoelectric actuator assembling and active control principles.

(6) Re-Design: A sixth option is to re-design the vertical tail subassembly such that it meets a specific set of specifications. These specifications include specific levels of (vertical tail) vibrations during high angle of attack maneuvers, a specified fatigue life and a ceiling on the cost of ownership. In practice, however, any redesign will have to consider options (1) to (5) that are described in this section.

I.7. Smart Structure Approach to Tail Buffet Alleviation

Active and passive flow control techniques are currently active research areas. To date, these approaches have resulted in limited success. The passive structural design options have been explored from 1975 to the present time. These passive designs are centered around stiffness modifications. Such an approach has not solved the problem. Vibrations are still experienced by the vertical tail and new fatigue cracks are observed in regions that are away from the regions of added stiffeners. This leaves us with the option of active structural control and active rudder control.

The oscillations of the rudder are discussed by Ashley et al. (1994). The approach is shown to be promising in some cases. For other cases like F-15 aircraft, the technique needs further improvements.

In this report, the option of the use of smart structures to actively control the buffet induced vibrations of the vertical tail is discussed. In this approach, instead of redistributing the energy into different areas of the structure, the energy is damped in the smart structures based active control loop. This has the potential of avoiding the creation of new fatigue cracks in different regions of the vertical tail (similar to passive structural modification).

II. OBJECTIVES

The objectives of the Phase II SBJR program are as follows.

(1) Develop methods of obtaining structural dynamic models for the F-15 vertical tail subassembly with its supports. These models are to be developed in a manner that are suitable for the design of smart structure based vibration controllers.

(2) Select a smart structure actuator and design the actuator subassembly to provide the needed control authority.

(3) Develop and implement a procedure to optimally place the sensors and actuators on the laboratory full scale subassembly and structural dynamically scaled models of the F-15 vertical tail subassembly.

(4) Develop controller design procedures that are suitable for tail buffet alleviation using smart structures.

(5) Design and validate controller, to reduce vibrations in the laboratory full scale F-15 vertical tail subassembly.

(6) Develop structural dynamically similar scale models of the vertical tail subassembly.

(7) Develop a wind tunnel model with aeroelastically scaled (reduced frequency scaled) vertical tail subassembly.

(8) Conduct wind tunnel tests to approximately obtain the exciting airloads and their frequency content by using the model with aeroelastic tails.

(9) Conduct wind tunnel tests to control the buffet induced vertical tail vibrations, of the [illegible] scale model of the F-15 aircraft with aeroelastically vertical tail. The control is to be implemented to reduce vibrations at selected natural frequencies of the vertical tail in the range of 5-100 Hz. The forward speed of the aircraft is to be scaled to correspond to approximately 110 m/sec. The angle of attack for control should be in the range 0-25°.

(10) Develop plans to control large amplitude buffet induced vibrations in the structural dynamically scaled models, laboratory full scale subassembly of the F-15 vertical tail and in the vertical tail subassembly attached to a full scale aircraft assembly and associated supports.

III. Development of Mathematical Models

Usually structural dynamic models are developed in the form of a finite element model. The linear finite element model is of the form

$$[M]\{\ddot{x}\}+[C]\{\dot{x}\}*[K]\{x\}=\{f\} \tag{1}$$

Realistic damping matrices [C] are not provided in the usual finite element model development. A model with damping is developed by first converting equation (1) in to a modal space representation with C=0,

$$\{\ddot{\xi}\}+[\varpi]\{\xi\}=\{Q\} \tag{2}$$

and then adding a modal damping

$$\{\ddot{\xi}\}+[\hat{C}]\{\hat{q}\}+[\varpi^2]\{\xi\}=\{\varpi\} \tag{3}$$

The finite element model developed in this manner is not always accurate. Errors are caused by the approximation, in the representation of the structure in the finite element space and by the approximate representation of the structures that support the vertical tail in a real aircraft. Additional errors are introduced during the estimation of the modal damping.

On the other hand, if an actual structural assembly is available, we can obtain modes, natural frequencies and damping ratios from experimental modal analysis. These models can be reconstructed in the form (1) or (3) from the experimental data. At Georgia Tech, we have a full scale F-15 vertical tail subassembly. This subassembly is mounted on a framework to simulate the structural dynamic characteristics of a full scale aircraft. The full scale aircraft data was obtained by testing (reference 1). In the next section, procedures for obtaining the model from experimental modal analysis is described.

III.1. Model Reconstruction From Experimental Modal Analysis (EMA) for Noise Control

From experimental modal analysis (EMA), we can get a model represented by the identified mode shapes ϕ_I matrix, frequencies ω_I, and damping ratios ζ_i. Sometimes, for example in noise control or structural dynamic characteristic adjustments, a model represented by mass matrix M, stiffness K, and damping matrix C is required. Traditionally, these matrices can be obtained through finite element method (FEM). Due to the complexities from the structures, materials and boundary conditions, such as in modern airplanes, the FEM model may not be able to predict a dynamic response that can match the experimental data. Sometimes a local vibration dominated mode shape., which can be detected by Experimental Modal Analysis (EAM) but not in FEM, can be a key issue in the vehicle interior noise reduction.

Though the EMA test can be calibrated so that the measuring signals have engineering units, the EMA mode shapes can still be relative quantities due to different estimation methods. The normalization of the EMA mode shapes is necessary before the mode shapes can be used in model reconstruction.

As accepted by many FEM engineers, the mass matrix produced by FEM usually has higher confidence factor than that of the stiffness matrix. Thus, it is reasonable to use FEM mass matrix in EMA mode shape normalization. After the mass normalization, the EMA mode shapes have the following properties:

$$\phi_i^T M \phi_i = 1$$

In an ideal case, using the normalized EMA mode shapes, we can construct the C and K matrices through the following expressions:

$$C = \left(\Phi^T\right)^{-1} diag\left(2\varpi_i \zeta_i\right)\Phi^{-1}$$

and

$$K = \left(\Phi^T\right)^{-1} diag\left(\varpi_i^2\right)\Phi^{-1}$$

where

$$\Phi = \{\phi_1, \phi_2, \quad ...\phi_m\}$$

and m is the number of modes available from EMA.

Unfortunately, these are not necessarily true. First of all, the orthogonality of the normalized mode shapes is not guaranteed. Without the orthogonality, the reconstructed model is unable to predict the measured dynamic response. And second, the number of modes obtained from EMA is usually smaller than the number of the measuring locations. Then, the mode shape matrix is a rectangular matrix.

One way to conduct the mass orthogonalization is to modify the EMA modal data. In this process, it is assumed that the mass matrix is accurate. The inaccuracy in the EMA data caused the off diagonal nonzero element in the orthogonality check matrix. The EMA modal data will be modified to satisfy the mode shape mass orthogonality conditions.

Assume the mass normalized EMA mode shape matrix is

$$\Phi \in R^{n \times m}$$

And it singular value decomposition is

$$M = UDV^T$$

Where D is the singular value matrix,

$$D = \begin{bmatrix} \Delta & 0 \\ 0 & 0 \end{bmatrix}, \quad \Delta = \mathrm{diag}\,(\alpha_1, \quad \alpha_2, \quad \ldots \quad , \alpha_1)$$

here $\alpha_1 \geq \alpha_2 \geq \ldots \geq \alpha_r > \alpha_{r+1} = \ldots = \alpha_m$ are singular values of Φ.

U and V are the orthonormal matrices and U 0 E^{nxn}, V 0 E^{mxm}

It is proven (Huang, Algebraic Linear Control, 1984) that if n>m, we have

$$\underset{w \in E^{n \times m}}{Min}\{\|\Phi - w\|_F^2\} = \left\|D - \begin{pmatrix} I \\ 0 \end{pmatrix}\right\|_F^2$$

And the minimum is reached when $w = U_1V^T$, where U_1 is the first m columns of the U matrix. And further, when r = m<n, the solution is unique.

The orthogonality is guaranteed in the modified mode shape w. A reconstructed M. C. K model based on the modified w and generalized inverse is able to predict the dynamic response obtained from the test. Thus a noise control strategy can be efficiently applied to the structure.

IV. CHOICE OF ACTUATOR [✦]

IV.1. Piezoceramic Stack Actuators for Vibration Control

Lead zirconate titanate (PZT) ceramic wafers are generally considered for vibration control applications. However, the control authority of PZT patch actuators, unless used in large quantities, is usually not sufficient for most large-scale real world applications. In addition, in an environment of large amplitude vibrations, the PZT wafers can debond from its host structure.

Piezoceramic stack actuators can increase the control authority through a more efficient use of the piezoceramic material properties. This increase is obtained by the use of the longitudinal d_{33} coefficient instead of the transverse d_{31} and d_{32} coefficients generally used with wafers. Furthermore, the increased stack forces result from the addition of the effective piezoelectric reactions by using the accumulation of reaction from each PZT in series as is illustrated by the free elongation ΔL and blocked force, F_b, which are:

$$\Delta L = nd_{33}V \tag{4.1}$$

$$F_b = nd_{33}VE_{33}Lw/h \tag{4.2}$$

Where d_{33} is the PZT longitudinal piezoelectric charge constant of the stack. L, w and t are the length, width and thickness, respectively, of the each piezoceramic element. E_{33} is the longitudinal short-circuit Young's Modulus of the piezoceramic element. V is the voltage applied across the actuator. Finally, n is the number of piezoceramic elements that form the stack.

[✦] Significant part of the work performed in this chapter are the result of in-house research at Georgia Tech

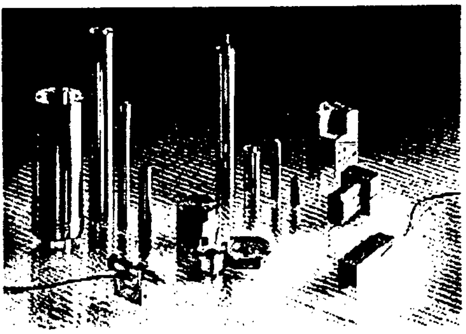

Figure 4.1. Variety of PZT Stack Actuators from Physik Instrumente (PI).

The main challenge, associated with the use of such active elements in alleviating the buffet-induced vibrations on an HPTTA, is that the piezoceramic stack produces only longitudinal motion or forces. An assembly must be designed to transform the longitudinal motion of the stack into moments that will produce the control actuation. Such a transformation can be achieved by placing the piezoceramic stack parallel to the controlled structure at a distance from its neutral axis and at a selected orientation. This distance will create a lever arm so that the longitudinal forces will result in local moments on the structure. The resulting assembly, as illustrated by Figures 4.2, is made of two mounts bonded to the host structure with a piezoceramic stack actuator attached in the middle.

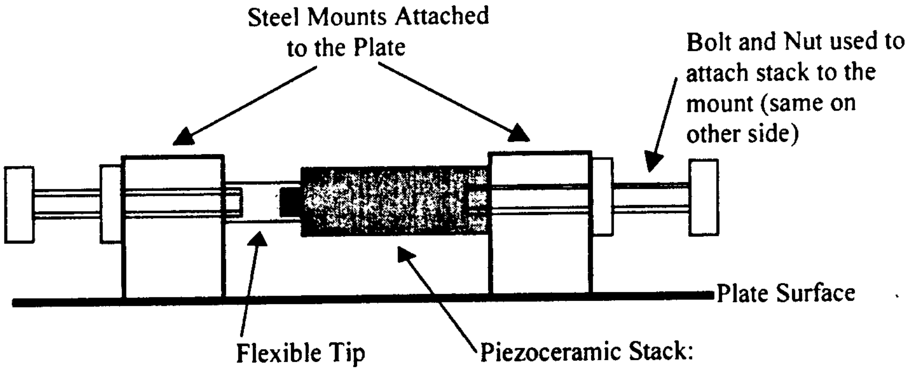
Steel Mounts Attached to the Plate
Bolt and Nut used to attach stack to the mount (same on other side)
Plate Surface
Flexible Tip
Piezoceramic Stack:

Figure 4.2. Sketch of Piezo-Stack Actuator Assembly

The added requirement that the active element, the piezoceramic stack, must be removable while the mount is attached to the structure results in different assembly designs depending on the type of piezoceramic stack used. For a regular piezo-stack, the assembly is made of three elements. As illustrated by Figure 4.2, the two external blocks are bonded to the host structure while a third block can be move longitudinally to allow the easy removal of the stack. The second type of design illustrated by Figure 4.3, uses a pre-compressed piezo-stack fixed between two blocks bonded to the host structure. In this design, the need for a flexible tip between the stack and one of the mounts is due to the low strength of the stack in bending.

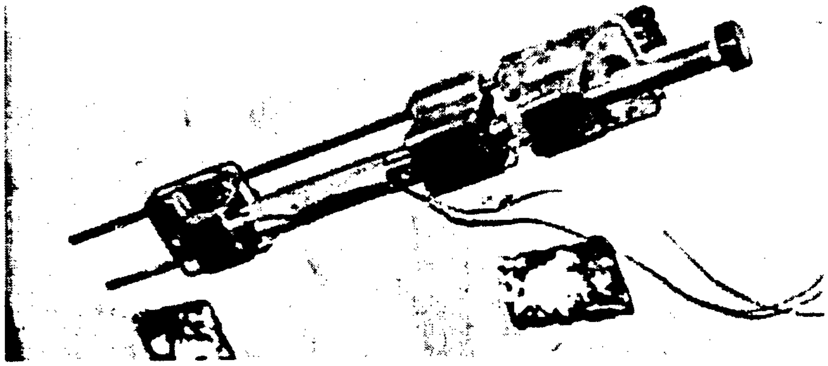

Figure 4.3. Example of Piezoceramic Stack Actuator Assembly.

IV.2. Model of a Fixed, Mass-Spring Piezoceramic Stack using Modal Expansion

Some initial work has been done in modeling piezoceramic stack actuators using modal expansion techniques. This technique is more useful when using second order equation based controllers than previously existing methods like finite element models or impedance based approaches.

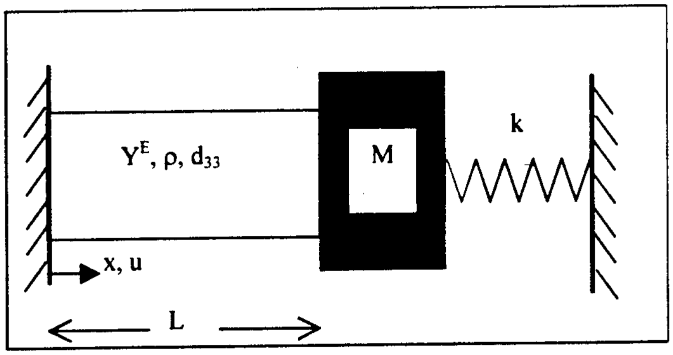

Figure 4.4. Fixed, Mass-Spring Piezoceramic Stack

The differential equation governing the piezoceramic stack system is given by:

$$Y^E \frac{\partial^2 u}{\partial x^2} = \rho \frac{\partial^2 u}{\partial t^2} \tag{4.3}$$

Where, Y^E and ρ are the Young's modulus and the density of the piezoceramic stack respectively. The longitudinal displacement of the stack is u positive in the x direction.

The boundary conditions associated with the problem are given by:

$$u(0,t) = 0 \tag{4.4}$$

$$-aY^E \left.\frac{\partial u}{\partial x}\right|_{x=L} - M \left.\frac{\partial^2 u}{\partial t^2}\right|_{x=L} - ku\big|_{x=L} = aY^E d_{33} E \tag{4.5}$$

Where a and L are the cross sectional area and the length of the stack respectively. The properties of the mass spring system are M, the mass, and k, the stiffness of the spring. Finally, d_{33} and E are the longitudinal piezoelectric charge constant of the stack and the electric field through the piezoceramic stack respectively. The above equation (4.5) does not represent a homogeneous boundary condition.

In order to apply modal expansion techniques, the problem must be transformed into a homogeneous boundary conditions problem. This transformation can be effectuated by assuming that $u(x,t) = \tilde{u}(x,t) + g(x)\Lambda(t)$, where the function $\tilde{u}(x,t)$ satisfies homogeneous boundary conditions. Let us choose the following functions:

$$g(x) = d_{33} x \left(-\left(\frac{2k_s - k}{M} \alpha + \beta \right) + \left(\frac{k_s - k}{M} \alpha + \beta \right) \frac{x}{L} \right) \tag{4.6}$$

$$\overline{\Lambda} = \frac{\overline{E}}{(\alpha s^2 + \beta)} \tag{4.7}$$

Where α and β are computational parameters. k_s is the equivalent spring stiffness of the piezo-stack and is given by $k_s = aY^E/L$. Furthermore, $\overline{\Lambda}$ and $\overline{E}$ are the Laplace transforms of the function Λ and the electric field across the stack respectively. For the purpose of simplicity and without loss of generality, let us choose:

$$\alpha = 1, \quad \beta = -\frac{k_s - k}{M} \tag{4.8}$$

With these functions, the differential equation (4.3) governing the system becomes:

$$\frac{\partial^2 \tilde{u}}{\partial x^2} - \frac{\rho}{Y^E}\frac{\partial^2 \tilde{u}}{\partial t^2} = \frac{\rho}{Y^E} d_{33} \frac{k_s}{M} x\ddot{\Lambda}(t) \tag{4.9}$$

and the boundary conditions are:

$$\tilde{u}(0,t) = 0 \tag{4.10}$$

$$k_s L \left.\frac{\partial \tilde{u}}{\partial x}\right|_{x=L} - M \left.\frac{\partial^2 \tilde{u}}{\partial t^2}\right|_{x=L} = 0 \tag{4.11}$$

Using separation of variables in the form of $\tilde{u}(x,t) = U(x)T(t)$, a solution of the differential equation with homogenous boundary conditions can be obtained. The form of the general solution for U(x) is:

$$U(x) = A\sin\left(\lambda \frac{x}{L}\right) + B\cos\left(\lambda \frac{x}{L}\right) \tag{4.12}$$

Were the non-dimensional parameter λ is given by $\lambda = \omega L \sqrt{\rho / Y^E}$.

The boundary condition and the condition that the solution is non-trivial yields to the following two conditions:

$$B = 0 \tag{4.13}$$

$$\frac{\tan(\lambda)}{k_s \lambda} = \frac{1}{k - M\omega^2} \tag{4.14}$$

It is to be noted that λ depends on ω. Furthermore, it is very important to note that the left-hand side of equation (4.14) only depends on the stack properties while the right hand side only depends on the properties of the driven system.

The solutions ω_i's of equation (4.14) are the natural frequencies of the complete system made of the stack, the mass and spring. Associated with these natural frequencies, we have the system mode shapes:

$$\phi_i(x) = \sin\left(\lambda_i \frac{x}{L}\right), i = 1, 2, 3, \ldots \tag{4.15}$$

Where the non-dimensional parameter λ_i is given by $\lambda_i = \omega_i L\sqrt{\rho/Y^E}$.

The last step of the modeling is to obtain the solution of the non-homogeneous boundary conditions problem by modal expansion. Using modal expansion theory, we can write:

$$\tilde{u}(x,t) = \sum_{i=1}^{\infty}\phi_i(x)\eta_i(t) \tag{4.16}$$

Using this result in the differential equation (4.9) and simplifying, we obtain:

$$\sum_{i=1}^{\infty}\phi_i\left(\ddot{\eta}_i + \omega_i^2\eta_i\right) = -d_{33}\frac{k_s}{M}x\ddot{\Lambda}(t) \tag{4.17}$$

By pre-multiplying by $\phi_j(x)$ and integrating over the domain, the system can be uncoupled, so that we have:

$$\ddot{\eta}_j + \omega_j^2\eta_j = d_{33}L\frac{k_s}{M}\frac{4(\lambda_j\cos(\lambda_j) - \sin(\lambda_j))}{\lambda_j(2\lambda_j - \sin(2\lambda_j))}\ddot{\Lambda}(t),\ j = 1, 2, 3, \ldots \tag{4.18}$$

By taking the Laplace transforms of Equations (4.18), replacing $\overline{\Lambda}(s)$ by its expression from Equation (4.7), using the result into $u(x,t) = \tilde{u}(x,t) + g(x)\Lambda(t)$ and, finally, replacing the Laplace transform parameter s by jω, the frequency response function of the system is given by:

$$\frac{\overline{u}}{\overline{E}}(x, j\omega) = d_{33}L\frac{k_s}{k_s - (k - M\omega^2)}\left(\sum_{i=1}^{\infty}B_i\phi_i(x)\frac{-\omega^2}{\omega_i^2 - \omega^2} + \frac{x}{L}\right) \tag{4.19}$$

Where the non-dimensional modal amplitude parameter B_i is given by:

$$B_i = \frac{4(\lambda_i\cos(\lambda_i) - \sin(\lambda_i))}{\lambda_i(2\lambda_i - \sin(2\lambda_i))},\quad i = 1, 2, 3, \ldots \tag{4.20}$$

There are two main advantages associated with the use of a modal expansion technique to obtain the transfer function between the displacement of the piezoceramic stack actuator and the electric field across it. The first one is directly related to type of control that is presented in this research. The transfer function obtained using this method is in the form of a partial fraction expansion that can be used directly to compute for the parameters of the controller. This form is more useful to the control designer than the result of the same problem using Laplace transforms:

$$\frac{\bar{u}}{\bar{E}}(x, j\omega) = d_{33}L\frac{k_s}{k_s\tilde{\lambda}\cos(\tilde{\lambda}) - (k - M\omega^2)\sin(\tilde{\lambda})}\sin\left(\tilde{\lambda}\frac{x}{L}\right) \qquad (4.21)$$

Where the non-dimensional parameter $\tilde{\lambda}$ is given by $\tilde{\lambda} = \omega L\sqrt{\rho/Y^E}$. It is to be noted that the impedance approach yields a resulting transfer function of the form of equation (4.21).

The second advantage associated with the modal expansion approach to model the piezoceramic stack actuator is that equation (4.19) can be easily be transformed to accommodate for modal damping. This latest change would result in the following equation:

$$\frac{\bar{u}}{\bar{E}}(x, j\omega) = d_{33}L\frac{k_s}{k_s - (k - M\omega^2)}\left(\sum_{i=1}^{\infty} B_i\phi_i(x)\frac{-\omega^2}{-\omega^2 + 2\zeta_i\omega_i\omega j + \omega_i^2} + \frac{x}{L}\right) \qquad (4.22)$$

The equation above can be updated using any type of experimental data. The natural frequencies ω_i's, the damping ratios ζ_i's and the mode shapes ϕ_i's can be tuned using experimental modal analysis results.

V. CURVATURE MODAL SURVEY FOR OPTIMAL ACTUATOR PLACEMENT[✦]

Besides the inherent control authority, the control effectiveness of an actuator also depends on the optimal actuator location. For this research, we developed a procedure of optimal actuator location based on "curvature modal survey." In the curvature modal survey, a Polyvinylidene Fluoride (PVDF) film is used as the sensor and a shaker is used as a vibration exciter. Once the curvature modal survey was conducted for the vertical tail, the curvature modes were visualized through a dynamic three dimensional animation

---

[✦] Significant part of the work performed in this chapter are the result of in-house research at Georgia Tech program. A more quantitative procedure was constructed to locate an optimal actuator location for the actuator.

V.1. PVDF Curvature Sensor

Typical PVDF film thickness ranges from 20 to 100 μm, thus, in practice, the sensor thickness can be neglected without introducing significant amount of error. With the assumptions that all in-plane strains are negligible, we have a general charge-deformation relation for a plate as

$$q(t) = -Gh \int_S \left(e_{31} \frac{\partial^2 w}{\partial x^2} + e_{32} \frac{\partial^2 w}{\partial y^2} + 2e_{36} \frac{\partial^2 w}{\partial x \partial y} \right) dxdy \tag{5.1}$$

Where q is the signal received by the A/D converter; G is the total electronic circuit gain: h is the distance form the sensor surface to the structure local neutral plane; S is the sensor area; w is the flexural displacement of the plate; e_{ij}'s are the piezo constants of the PVDF film.

Usually, in PVDF e_{36} is negligibly small, and in most cases the PVDF piezoelectric properties are made non-uniform (e.g. $e_{31}/e_{32} \approx 10$), thus equation (5.1) can be simplified as

$$q(t) = -Ghe_{31}\kappa_{xx}S \tag{5.2}$$

where κ_{xx} and is the averaged local curvatures in x (sensor length) directions. Equation (5.2) indicates that the sensor output is proportional to the local curvatures.

V.2. Instrumentation for Curvature Modal Survey

As shown in Figure 5.1, the PVDF film modal survey instrumentation in this program includes the following instruments:

a) Signal generator: Wavetek Model 132

b) Power amplifier: MB Dynamics Model SS250

c) Vibration shaker: MB Dynamics Modal 50A Exciter

d) Force transducer: PCB Model 208A02

e) Signal conditioner: PCB Model 482A04

f) Anti-alias filters: Krohn-Hite Model 3343

g) PVDF film sensor: ATM LDT2-052K

h) Oscilloscope: Tektronix Model 2236

i) A/D converter: dSPACE DSP Board DS1102

j) PC computer: DELL Optiplex 466/Le

The interested frequency range in the first survey is 0-50Hz (A broader frequency 0-100 range analysis was conducted later). To reduce the sampling deviation, the sampling frequency was selected to be 200Hz. The random signal generated from the signal generator has a bandwidth of 0-100Hz. The generated signal is then amplified by the power amplifier before feeding to the vibration shaker. A force transducer is used to detect the force transmitted to the F15 vertical tail by the shaker. The detected force signal is conditioned by the signal conditioner. A PVDF film sensor was attached to the F15 vertical tail by a double sided tape to pick up the local curvature response due to the excitation. Both the force signal and response signal are passed through anti-aliasing filters to increase signal/noise ratio. The signals are digitized by an A/D converter built in the DSP board. The signal processing is conducted on a PC computer.

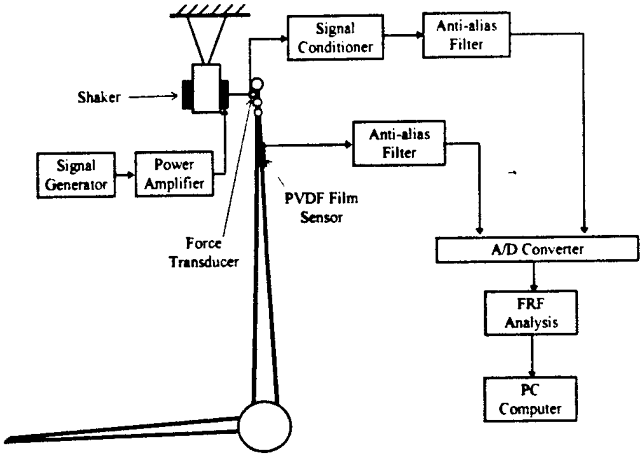
Signal Conditioner
Anti-alias Filter
Shaker
Anti-alias Filter
Signal Generator
Power Amplifier
PVDF Film Sensor
Force Transducer
A/D Converter
FRF Analysis
PC Computer

Figure 5.1 Curvature Modal Survey Instrumentation

The modal survey was concentrated on the main torque box of the vertical tail. Seventy-nine nodes, as shown in Figure 5.2, were utilized to discretize the structure.

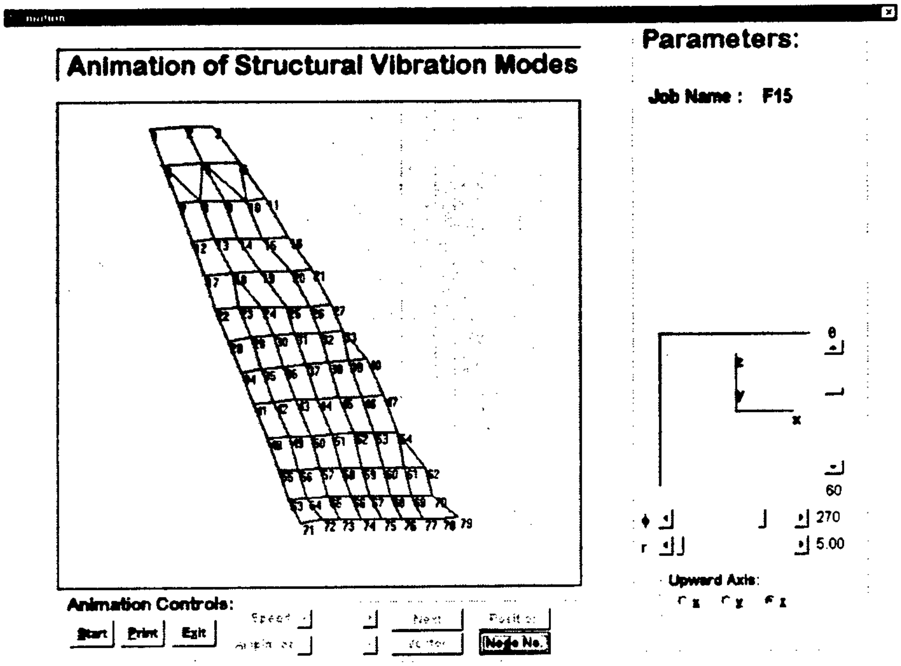
Animation of Structural Vibration Modes

Parameters:

Job Name : F15

Figure 5.2 Discretization of the structure

V.3. Z-Direction Curvature Modal Survey

Modal survey was first conducted in the z-direction, that is, the PVDF film sensor is placed in z-directions. A total of 79 frequency response functions (FRFs) between the curvature response and the force transducer were collected. For each location, the data sampling lasted 40.5 second, thus a total of 8,100 data points were available for FRF analysis. The FFT range was selected to be 1024 time data points. To get a high confidence factor in the random signal processing, 35 over-lap averaging was used to get an FRF. The overlap moving window is automatically calculated such that the averaging evenly covered all the time data.

The frequency and damping parameters were identified from the overall FRF (see Figure 5.3), which is the summation of the 79 FRFs. In this way, we were able to remove the bias by using a single FRF identification, and thus get frequency and damping parameters with high precision. As is well-known, modal parameters, especially the damping ratio parameters may vary from location to location. The parameters identified from a single location FRF are biased. The parameters identified from the overall FRF reflect the overall characteristics of the structure.

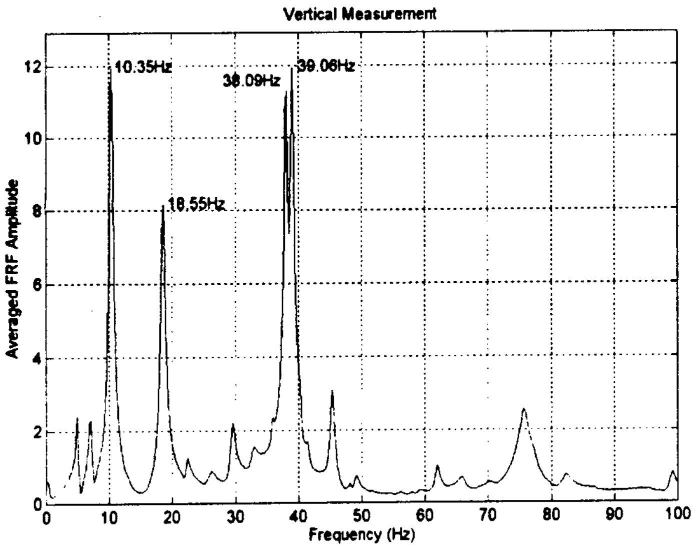

Figure 5.3 Overall FRF, z-direction

From the overall FRF, the frequency and damping parameters of the first four structural modes are identified and listed in Table 5.1.

Table 5.1 Frequencies and damping ratios, z-measurement

	Mode 1	Mode 2	Mode 3	Mode 4
Frequency (Hz)	10.35	18.55	38.09	39.06
Damping (%)	4.83	2.99	1.44	1.39

The corresponding four mode shapes are identified and their vector displays are shown in Figures 5.4 to 5.7.

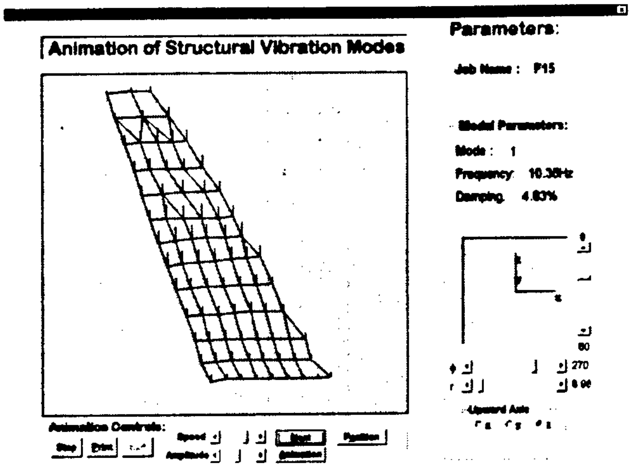
Animation of Structural Vibration Modes
Parameters:
Animation Controls:
Step
Print
Speed
Amplitude
Next
Animation
Position
90
270
Upward Axis:
x
y
z

Job Name : F15

Modal Parameters:

Mode : 1

Frequency 10.38Hz

Damping 4.83%

Figure 5.4 Mode 1, vector display, z-direction

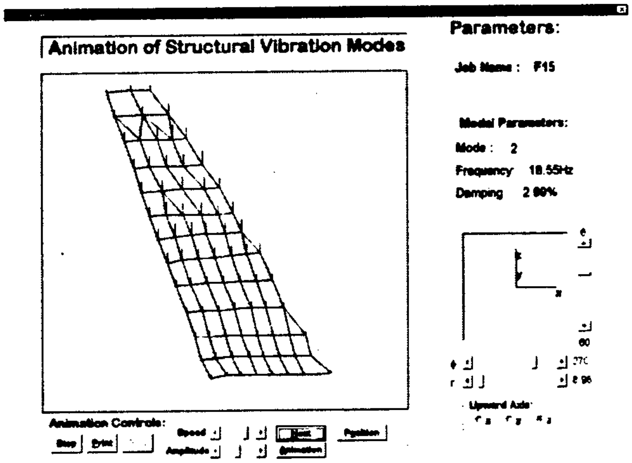
Animation of Structural Vibration Modes
Parameters:
Animation Controls:
Step
Print
Speed
Amplitude
Next
Animation
Position
90
270
Upward Axis:
x
y
z

Job Name : F15

Modal Parameters:

Mode : 2

Frequency 18.55Hz

Damping 2.90%

Figure 5.5 Mode 2, vector display, z-direction

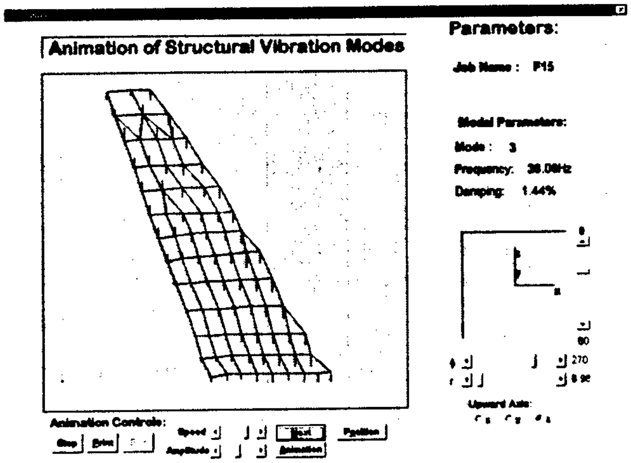
Animation of Structural Vibration Modes
Parameters:
Animation Controls:
Step
Print
Speed
Amplitude
Next
Animation
Position
90
270
Upward Axis:
x
y
z

Job Name : F15

Modal Parameters:

Mode : 3

Frequency: 38.08Hz

Damping: 1.44%

Figure 5.6 Mode 3, vector display, z-direction

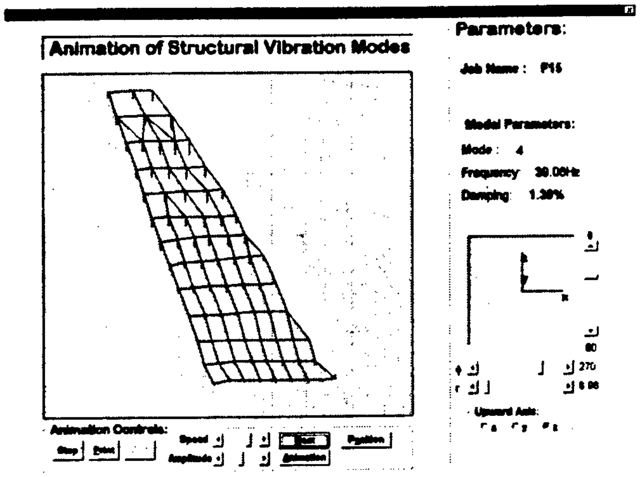

Animation of Structural Vibration Modes

Parameters:

Job Name : P15

Model Parameters:

Mode : 4

Frequency 30.00Hz

Damping: 1.30%

Animation Controls:
Stop
Print
Speed
Amplitude
Animation
Position
80
270
Upward Axis:

Figure 5.7 Mode 4 vector display, z-direction

The vector display and animation of a vibration mode give a very good qualitative image of the modes. To get a more quantitative understanding of each mode, which is important in optimal actuator location, we have shown a barplot of the first four curvature modes in Figures 5.8 to 5.11, where the horizontal axes list the structural measuring locations.

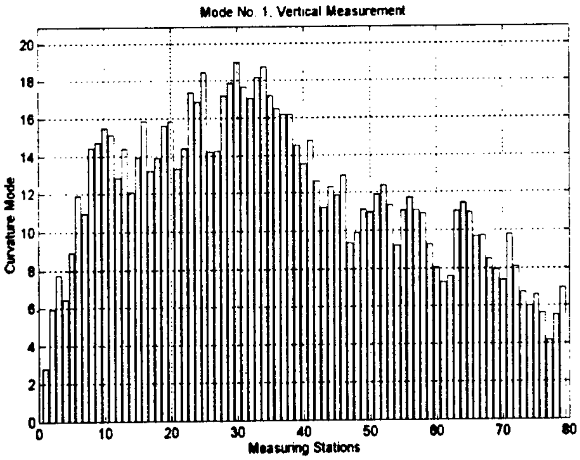

Figure 5.8 Mode 1, barplot, z-direction

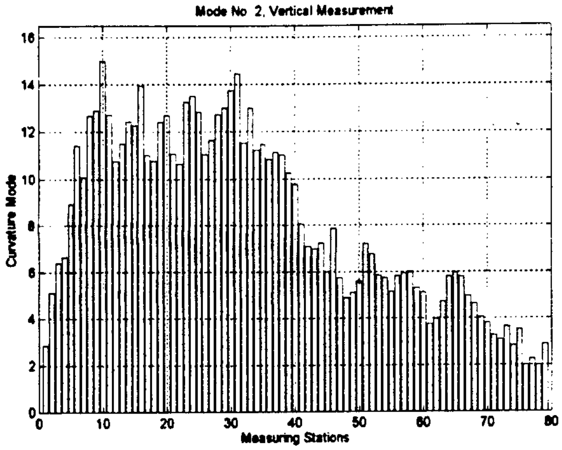

Figure 5.9 Mode 2, barplot, z-direction

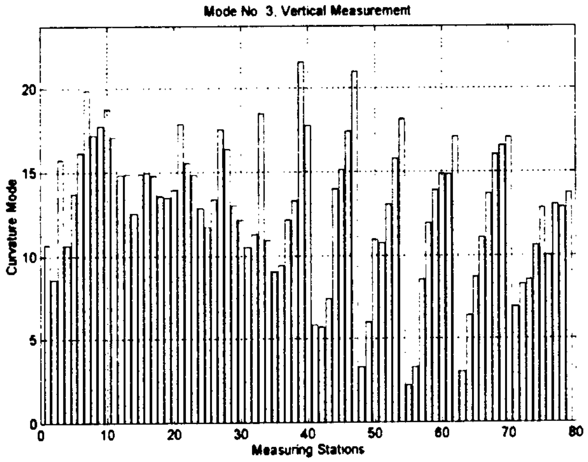

Figure 5.10 Mode 3 barplot, z-direction

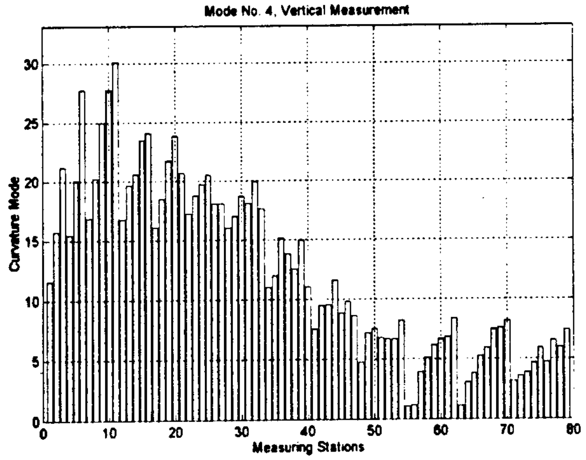

Figure 5.11 Mode 4 barplot, z-direction

V.4. X-Direction Curvature Modal Survey

Similar to the z-direction modal survey, an x-direction modal survey was also conducted. The results are as follows: Figure 5.12 is the overall FRF. Based on the overall FRF, the frequency and damping parameters were identified and listed in Table 5.2. Figures 5.13 to 5.16 display the first four modes vector display. Figures 5.17 to 5.20 are the corresponding bar plot of the four modes.

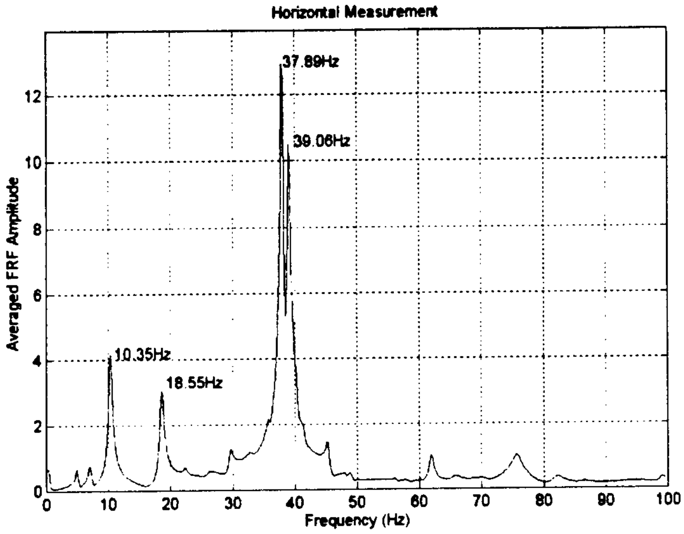

Figure 5.12 Overall FRF, x-direction

Table 5.2 Frequencies and damping ratios, x-direction measurement

	Mode 1	Mode 2	Mode 3	Mode 4
Frequency (Hz)	10.35	18.55	37.89	39.06
Damping (%)	4.81	2.76	1.39	1.29

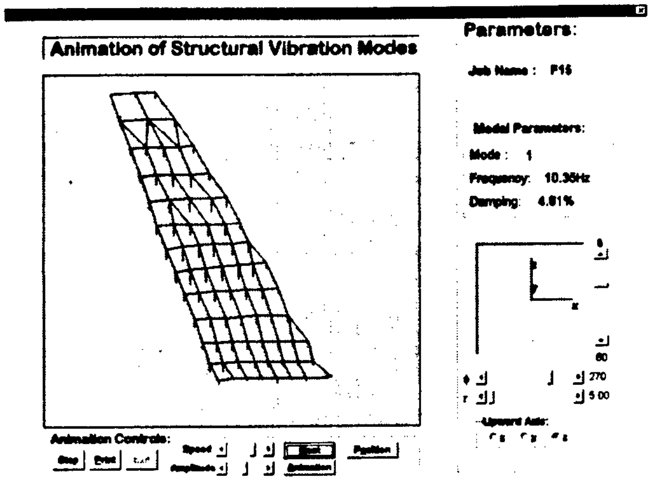
Animation of Structural Vibration Modes
Parameters:
Animation Controls:
Stop
Print
Exit
Speed
Amplitude
Next
Animation
Position
60
270
5.00
Upward Axis:

Job Name : F15

Modal Parameters:

Mode : 1

Frequency: 10.35Hz

Damping: 4.81%

Figure 5.13 Mode 1, vector display, x-direction

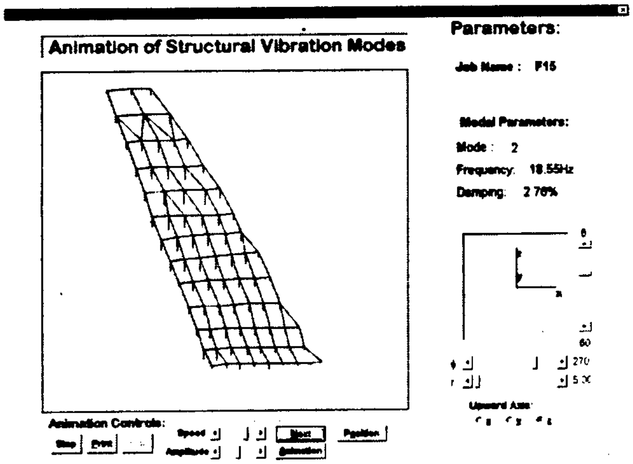
Animation of Structural Vibration Modes
Parameters:
Animation Controls:
Stop
Print
Speed
Amplitude
Next
Animation
Position
60
270
5.00
Upward Axis:

Job Name : F15

Modal Parameters:

Mode : 2

Frequency: 18.55Hz

Damping: 2.76%

Figure 5.14 Mode 2, vector display, x-direction

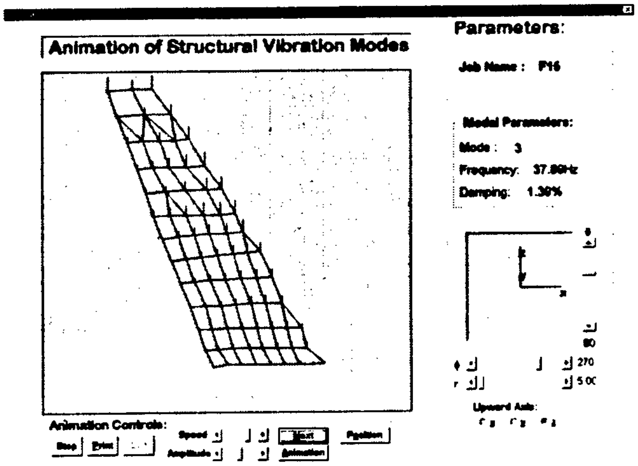
Animation of Structural Vibration Modes
Parameters:
Animation Controls:
Stop
Print
Speed
Amplitude
Next
Animation
Position
60
270
5.00
Upward Axis:

Job Name : F15

Modal Parameters:

Mode : 3

Frequency: 37.80Hz

Damping: 1.30%

Figure 5.15 Mode 3, vector display, x-direction

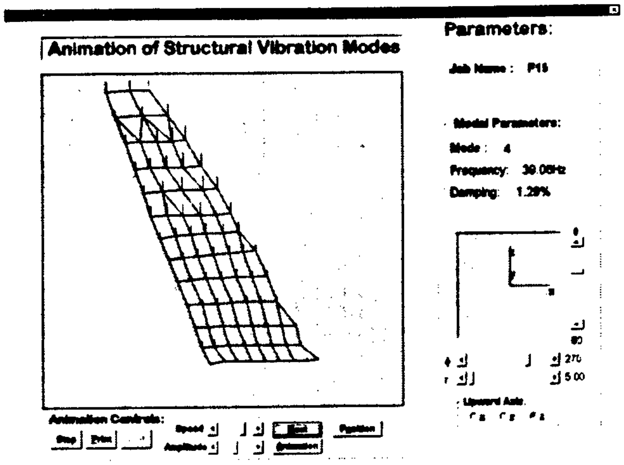
Animation of Structural Vibration Modes
Animation Controls:
Stop
Print
Speed
Amplitude
Quit
Animation
Position
Upward Axis:
x
y
z
270
5.00
80

Parameters:

Job Name : P15

Modal Parameters:

Mode : 4

Frequency: 39.06Hz

Damping: 1.29%

Figure 5.16 Mode 4, vector display, x-direction

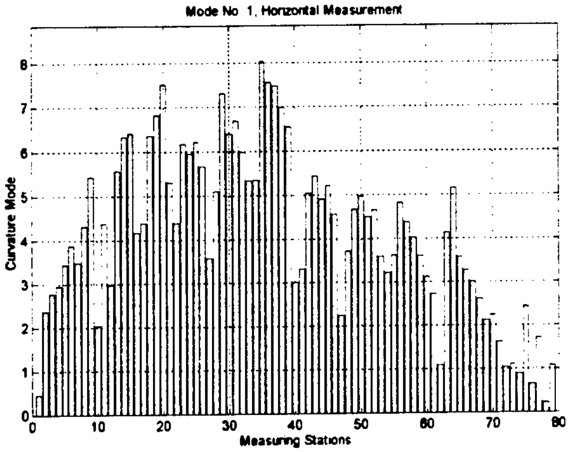

Figure 5.17 Mode 1, bar plot, x-direction

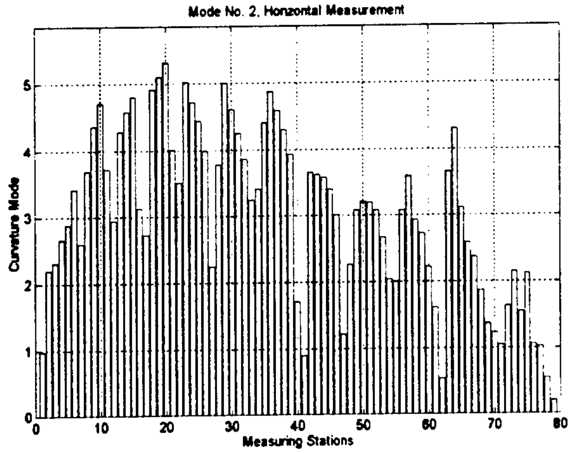

Figure 5.18 Mode 2, bar plot, x-direction

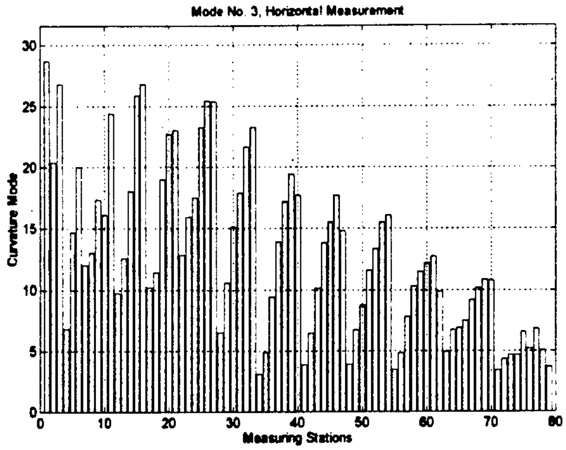

Figure 5.19 Mode 3, bar plot, x-direction

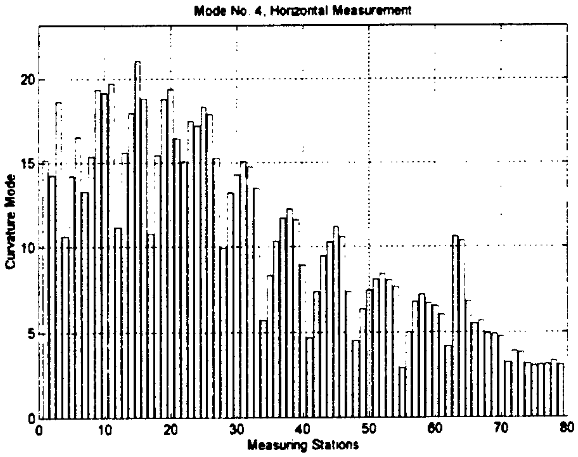

Figure 5.20 Mode 4, bar plot, x-direction

V.5. Results and Control Authority Analysis

From the results of the z- and x-directional modal surveys, several observations were made:

a) From Tables 5.1 and 5.2, we can see the high repeatability of frequency and damping ratio parameters obtained from the two surveys. It indicates the modal surveys are reliable. In Tables 5.1 and 5.2, most of the frequency parameters are repeated. The third mode frequency has about 0.2 Hz difference between x- and z-directional modal surveys. This difference is in the range of the analysis resolution, which is 200/1024 Hz.

b) By comparing the overall FRF of the z-directional modal survey in Figure 5.3 and that of the x-directional modal survey in Figure 5.12, we can see that for modes 1 and 2, it is more efficient to control the vibrations by actuating in z-direction, while for certain modes (e.g. third mode), control in x-direction may provide as good or more efficient vibration suppression. The combination of x- and z-direction will provide much improved control authority in vibration suppression of these modes.

The mode vector displays provide a qualitative estimation of the most effective actuator location, while the bar plots are able to give a more quantitative estimation for a given mode. To locate the optimal location for a given mode, we can first check the vector display and barplot to figure out candidate locations for optimal control. A more careful comparison can then be conducted on these candidate locations.

As an example, in the following, we use the guidelines stated above to locate the optimal actuator locations for third mode vibration control. As a first step, we checked the vector display and barplot. The z-directional optimal actuator location should be along the line joining discrete nodes 33-40-47-54. A further refined modal survey was conducted in that area (see Figure 5.21). By comparing the refined survey results (Zoom results are shown in Figure 5.21), we were able to identify that V1 location (which is between node 46 and 47) as the best actuator location for the third mode vibration control in z-direction.

In a similar way, we found that the optimal x-directional actuator location to be in the area of nodes 11-16-21-27. The refined modal survey is displayed in Figure 5.22 and a zoomed view is shown in Figure 5.23. Finally the optimal actuator location is found to be H3 location which is close to nodes 15 and 16.

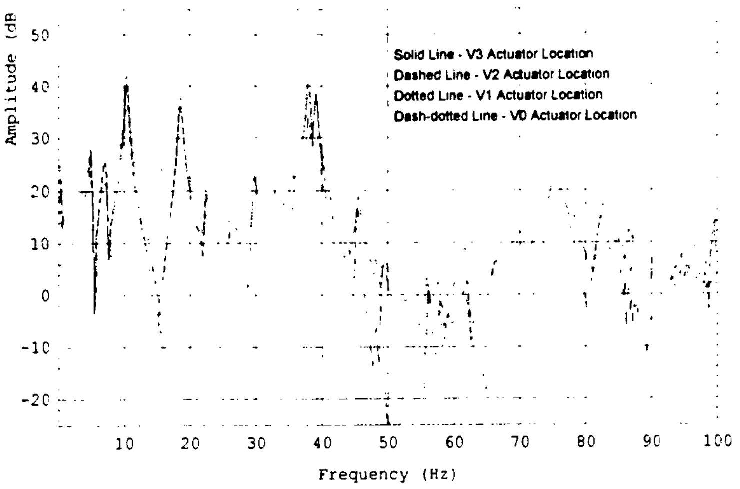

Figure 5.20 Refined modal survey, z-direction

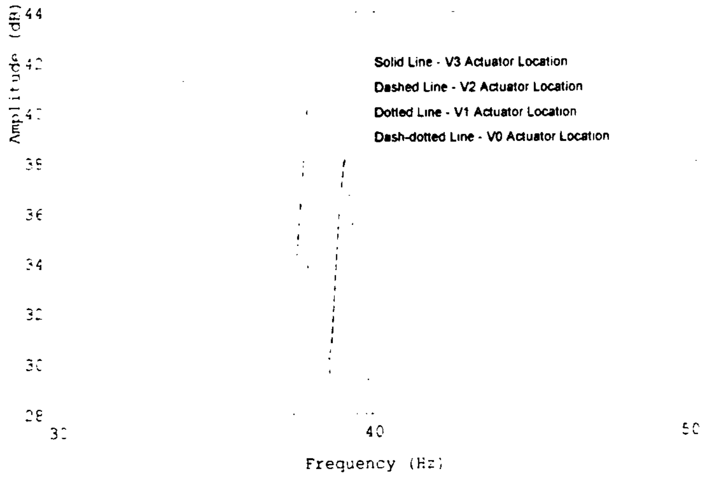

Figure 5.21 Zoomed view of the refined modal survey, z-direction

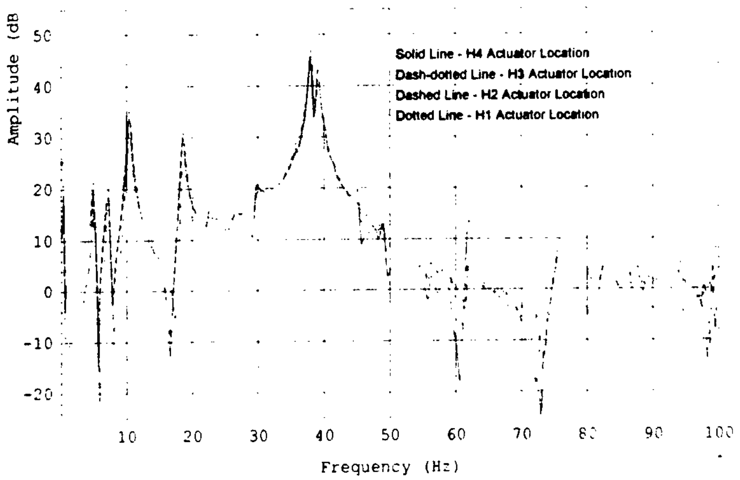

Figure 5.22 Refined modal survey, x-direction

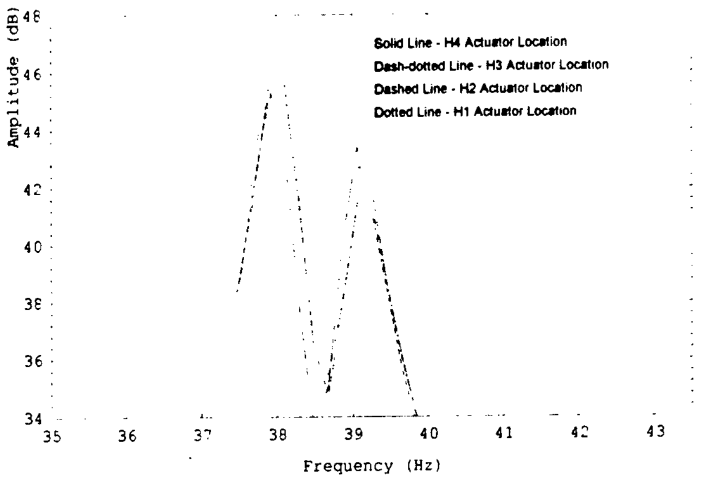

Figure 5.23 Zoomed view of the refined modal survey, x-direction

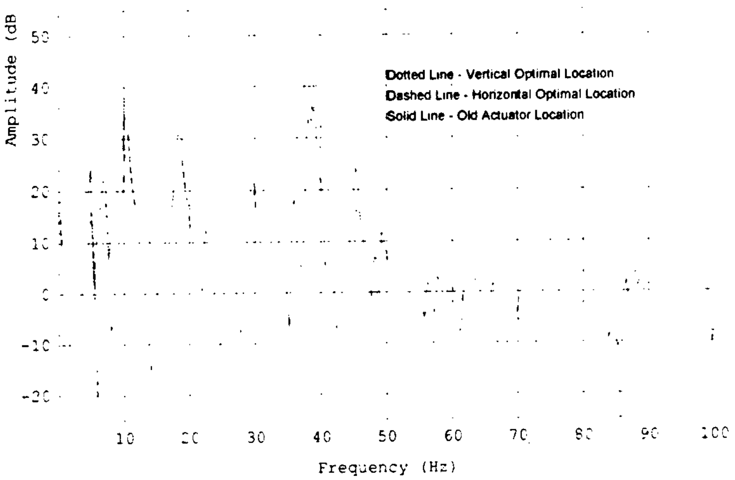

Figure 5.24 Optimal actuator locations

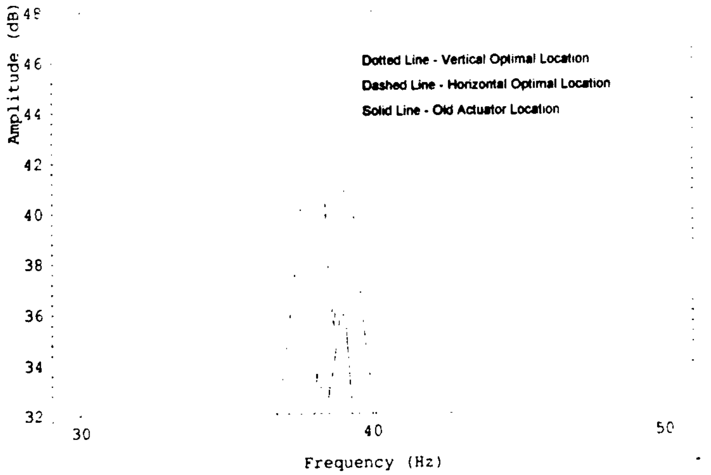

Figure 5.25 Zoomed view of the optimal actuator locations

The actuator locations determined by this process should have much better control authority in vibration suppression. As shown in Figure 5.24, both the x-and z-direction control authorities are compared with the actuator location near nodes 28-29-34-35, which is the optimal actuator location from a previous coarse grid modal survey. In the zoomed view in Figure 5.25, we can see that using either z-directional actuator location or an x-directional actuator location we have better control authority than the previously determined optimal actuator location through a coarse modal survey. By using a combination of the z-directional and x-directional actuator locations we can get an improved control authority than before.

VI. ACCELERATION FEEDBACK CONTROL COMPENSATORS DESIGNS[✦]

VI.1. Single Degree Of Freedom Representation Of The Acceleration Feedback Control

The equations describing the active damping of a single degree of freedom system using Acceleration Feedback Control (AFC) consist of a structural modal equation with feedback force due to the actuator and a disturbance force; and a compensator modal equation with acceleration sensing component. These equations are:

$$\begin{cases} \ddot{\xi} + 2\zeta_s \omega_s \dot{\xi} + \omega_s^2 \xi = -a_1 \gamma \omega_c^2 \eta + f \\ \ddot{\eta} + 2\zeta_c \omega_c \dot{\eta} + \omega_c^2 \eta = a_2 \ddot{\xi} \end{cases} \tag{6.1.a-b}$$

where ξ and η are the modal coordinates of the structure and of the compensator, respectively; ω_s, ω_c, ζ_s and ζ_c are the natural frequencies and the damping ratios of the structure and the compensator, respectively; γ is a scalar gain applied to the feedback signal; and a_1 and a_2 are the sensitivity constants of the actuator and of the sensor, respectively.

[✦] Significant part of the work performed in this chapter is the result of in-house research at Georgia Tech

It is to be noted that the use of an acceleration sensing device is not a necessary condition for the implementation of AFC. If one uses a velocity sensing device, the following equations are used:

$$\begin{cases} \ddot{\xi} + 2\zeta_s\omega_s\dot{\xi} + \omega_s^2\xi = -a_1\gamma\omega_c\dot{\eta} + f \\ \ddot{\eta} + 2\zeta_c\omega_c\dot{\eta} + \omega_c^2\eta = a_2\omega_c\dot{\xi} \end{cases} \qquad (6.2.a\text{-}b)$$

Similarly, if one uses a position sensing device, the following equations could be used:

$$\begin{cases} \ddot{\xi} + 2\zeta_s\omega_s\dot{\xi} + \omega_s^2\xi = -a_1\gamma\ddot{\eta} + f \\ \ddot{\eta} + 2\zeta_c\omega_c\dot{\eta} + \omega_c^2\eta = a_2\omega_c^2\xi \end{cases} \qquad (6.3.a\text{-}b)$$

All these formulations result in the same closed-loop transfer function between the structural modal parameter and the disturbance force.

Without loss of generality, by taking the Laplace Transforms of equations (6.1.a) and (6.1.b), assuming zero initial conditions, and solving for η in the second equation, one can obtain the transfer functions of the closed loop system and the controller, namely:

$$\begin{cases} G_s(s) = \dfrac{\overline{\xi}}{\overline{f}} = \dfrac{\left(s^2 + 2\zeta_c\omega_c s + \omega_c^2\right)}{\left(s^2 + 2\zeta_s\omega_s s + \omega_s^2\right)\left(s^2 + 2\zeta_c\omega_c s + \omega_c^2\right) + a_1 a_2\gamma\omega_c^2 s^2} \\ G_c(s) = \dfrac{\omega_c^2\gamma\overline{\eta}}{a_2 s^2\overline{\xi}} = \dfrac{\omega_c^2\gamma}{\left(s^2 + 2\zeta_c\omega_c s + \omega_c^2\right)} \end{cases} \qquad (6.4.a\text{-}b)$$

The stability of such a system can be studied by applying the Routh-Hurwitz criterion to the closed loop characteristic equation:

$$\left(s^2 + 2\zeta_s\omega_s s + \omega_s^2\right)\left(s^2 + 2\zeta_c\omega_c s + \omega_c^2\right) + a_1 a_2\gamma\omega_c^2 s^2 = 0 \qquad (6.5)$$

The Routh-Hurwitz criterion states that a necessary and sufficient condition for stability is that all the principal minors of the corresponding Routh-Hurwitz array be greater than zero. In this case the principal minors are:

$$
\begin{aligned}
M_1 &= \beta_s + \beta_c \\
M_2 &= \frac{\beta_s\omega_s^2 + \beta_c\omega_c^2 + \left(\beta_s\beta_c + a_1a_2\gamma\omega_c^2\right)\left(\beta_s + \beta_c\right)}{\beta_s + \beta_c} \\
M_3 &= \frac{\beta_s\beta_c\left(\left(\omega_s^2 - \omega_c^2\right)^2 + \left(\beta_s + \beta_c\right)\left(\beta_s\omega_c^2 + \beta_c\omega_s^2\right)\right) + a_1a_2\gamma\omega_c^2\left(\beta_s + \beta_c\right)\left(\beta_s\omega_c^2 + \beta_c\omega_s^2\right)}{\beta_s\omega_s^2 + \beta_c\omega_c^2 + \left(\beta_s\beta_c + a_1a_2\gamma\omega_c^2\right)\left(\beta_s + \beta_c\right)} \\
M_4 &= \omega_s^2\omega_c^2
\end{aligned}
\tag{6.6}
$$

where $\beta_s = 2\zeta_s\omega_s$ and $\beta_c = 2\zeta_c\omega_c$. The first conclusion that one can make about stability is that if a_1 and a_2 have the same signs, meaning that the mode is seen with the same phase by both the sensor and the actuator, a sufficient condition for stability is that γ is positive. On the other hand, if a_1 and a_2 have opposite signs, meaning that the mode is seen out of phase by the sensor compared with the phase of the actuator, a sufficient condition for stability is that γ is negative. Since only the only term depending on γ has always the form $a_1a_2\gamma$, a sufficient condition for stability is that $a_1a_2\gamma$ be positive.

VI.2. Cross-Over Design For The Compensator Parameters

The design of the parameters of the compensator is usually determined by the closed-loop damping of the system. In the design proposed by Goh and Yan, the damping of the compensator is set to unity, and thus obtaining a critically damped compensator. However, in such a design, spillover may result.

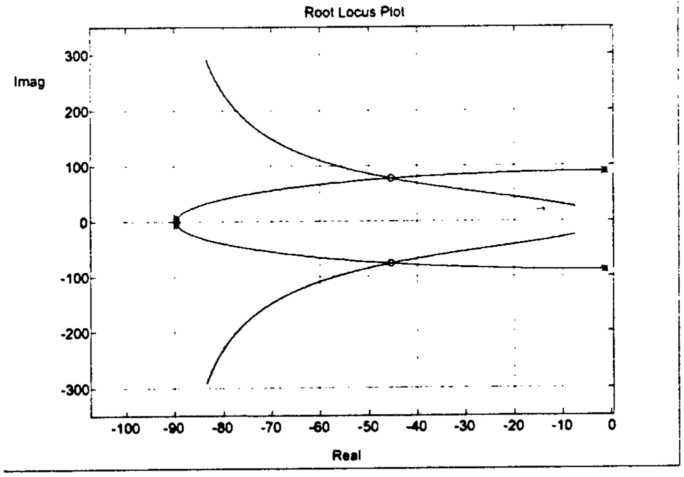

Figure 6.1. Single Degree of Freedom System under AFC Root Locus Plot and Cross Over Point (o)

If one looks at the root locus of an AFC, as shown on Figure 6.1, a particular point of interest is the crossover point. At this point, the closed-loop poles of the structure and of the compensator coincide. This means that in the response of the closed-loop system, a single peak would appear. A single peak design would be important in the case of a relatively dense pack of modes or if one does not want to add new modes to the controlled structure, in a single or multi degrees of freedom system. The crossover point is obtained when the roots of the closed-loop characteristic equation are repeated complex conjugate pairs.

$$\left(s^2+2\zeta_s\omega_s s+\omega_s^2\right)\left(s^2+2\zeta_c\omega_c s+\omega_c^2\right)+a_1a_2\gamma\omega_c^2 s^2=\left(s^2+2\zeta_f\omega_f s+\omega_f^2\right)^2 \tag{6.7}$$

In this equation, ω_f and ζ_f are the natural frequency and the damping ratio of the closed-loop system, respectively. By expanding both sides of the equation and equating the terms of same power of s, four conditions are obtained to operate at the crossover point. These are:

$$\begin{cases} 2\zeta_f\omega_f=\zeta_s\omega_s+\zeta_c\omega_c, \\ 2\omega_f^2+4\zeta_f^2\omega_f^2=\omega_s^2+4\zeta_s\omega_s\zeta_c\omega_c+\omega_c^2+a_1a_2\gamma\omega_c^2, \\ 2\zeta_f\omega_f^3=\omega_s^2\zeta_c\omega_c+\omega_c^2\zeta_s\omega_s, \\ \omega_f^4=\omega_s^2\omega_c^2. \end{cases} \tag{6.8.a-d}$$

Using Equations (6.8.a), (6.8.c) and (6.8.d) to find a relation between the compensator natural frequency and damping ratio and the structure natural frequency and damping ratio, we must have:

$$\omega_s\omega_c\left(\zeta_s-\zeta_c\right)\left(\omega_s-\omega_c\right)=0 \tag{6.9}$$

By inspection of Equation (6.9), we obtain the following three possible conditions:

$$\begin{aligned} \omega_c&=0, \\ \zeta_c&=\zeta_s, \\ \omega_c&=\omega_s. \end{aligned} \tag{6.10.a-c}$$

The condition (6.10.a) is not a useful condition since it would lead to $\omega_f = 0$. Further, condition (6.10.b) is not useful either since it leads to:

$$\zeta_f = \frac{\zeta_s}{2}\left(\frac{\omega_s}{\omega_f} + \frac{\omega_f}{\omega_s}\right) \tag{6.11}$$

As a result, the final closed-loop natural frequency would need to be far away from the initial structural natural frequency to increase the damping. However, the third condition, Equation (6.10.c) provides a practical design. It is taken to be the first crossover condition. Equation (6.8.d), under this condition, yields the condition that the closed-loop natural frequency will also be equal to the open-loop structural natural frequency. Furthermore, using this result and Equation (6.8.b), another crossover design condition is:

$$\gamma = \frac{(\zeta_s - \zeta_c)^2}{a_1 a_2} \tag{6.12}$$

This result means that under cross over conditions, the product $a_1 a_2 \gamma$ will always be positive so that the closed-loop system will be stable. Furthermore, the closed-loop damping ratio will be given by:

$$\zeta_f = \frac{1}{2}(\zeta_s + \zeta_c) \tag{6.13}$$

Thus, a design methodology will be to obtain the initial structure parameters ω_s and ζ_s as well as a_1 and a_2, the sensitivity constants of the actuator and of the sensor, respectively, either as a mathematical representation or by using experimental data. Then, one can choose a final closed-loop value for the damping ratio ζ_f and solve Equation (6.13) for the necessary compensator damping ratio ζ_c. Finally, using Equation (6.12), compute the necessary scalar gain γ to be at the crossover point.

VI.3. H_2 Optimal Design For The Compensator Parameters

Another way to design the single degree of freedom AFC compensator is to minimize the H_2 norm of the closed-loop system transfer function. This design would result in minimizing the average power output of the closed-loop system in the presence of white noise disturbance.

Let us assume that $\omega_c = \omega_s$ and minimizes the H_2 norm of a single degree of freedom system under acceleration feedback control. In this case, equation (6.4.a) can be rewritten as:

$$G_s(s) = \frac{\left(s^2 + 2\zeta_c \omega_s s + \omega_s^2\right)}{\left(s^2 + \lambda_1 \omega_s s + \omega_s^2\right)\left(s^2 + \lambda_2 \omega_s s + \omega_s^2\right)} \tag{6.14}$$

Where:

$$\lambda_1 = \left(\zeta_c + \zeta_s - \sqrt{(\zeta_c - \zeta_s)^2 - a_1 a_2 \gamma}\right) \tag{6.15.a}$$

And

$$\lambda_2 = \left(\zeta_c + \zeta_s + \sqrt{(\zeta_c - \zeta_s)^2 - a_1 a_2 \gamma}\right) \tag{6.15.b}$$

The H_2 norm of a transfer function $G(j\omega)$ is defined to be:

$$H_2^2(G) = \frac{1}{2\pi} \int_{-\infty}^{+\infty} G(j\omega) G^*(j\omega) d\omega \tag{6.16}$$

For our single degree of freedom system under AFC, the magnitude square of the closed loop transfer function $G_s(j\omega)$ is given by:

$$G(j\omega) G^*(j\omega) = \frac{\left(-\omega^2 + 2\zeta_c \omega_s \omega j + \omega_s^2\right)\left(-\omega^2 - 2\zeta_c \omega_s \omega j + \omega_s^2\right)}{\prod_{i=1}^{8} (\omega - p_i)} \tag{6.17}$$

In this equation, the p_i's are the roots of the characteristic equation. Then, using complex residue theory for improper integrals over $(-\infty, +\infty)$, a simple closed form expression of the H_2 norm can be obtained:

$$H_2(G_s(j\omega)) = \sqrt{\frac{a_1 a_2 \gamma + 4\zeta_c (\zeta_c + \zeta_s)}{4\omega_s^3 (\zeta_c + \zeta_s)(a_1 a_2 \gamma + 4\zeta_c \zeta_s)}} \tag{6.18}$$

To obtain the H_2 optimal parameters, γ and ζ_c, such that the H_2 norm of the closed loop transfer function is minimized, we set the derivatives of equation (6.18) with respect to γ and ζ_c equal to zero.

The derivative with respect to ζ_c gives:

$$a_1 a_2 \gamma \omega_s^3 \left(a_1 a_2 \gamma - 4\zeta_c^2\right) = 0 \tag{6.19.a}$$

And the derivative with respect to γ gives:

$$4\omega_s^3 \zeta_c^2 \left(\zeta_c + \zeta_s\right) = 0 \tag{6.19.b}$$

Equation (6.19.b) shows that there is no optimal feedback gain, γ. But equation (6.19.a) yields the result that for a particular value of γ, there is an optimal value of the compensator damping ratio, ζ_c, that will minimize the H_2 norm of the closed loop transfer function. This optimal value is given by:

$$\zeta_c = \frac{1}{2}\sqrt{a_1 a_2 \gamma} \tag{6.20}$$

This type of design yields to a value for $a_1 a_2 \gamma$ that is always positive, $4\zeta_c^2$, so that the compensator is stable. The initial steps to design an H_2 optimal controller follows the ones presented in the section about the cross-over design. In contrast to the cross-over compensator design, the H_2 compensator designer will first select a scalar gain value and then optimize the damping ratio using equation (6.20).

VI.4. Validation of the $\omega_C = \omega_S$ Assumption

The initial assumption that was made to compute the H_2 norm of the single degree of freedom system under acceleration feedback control was that the compensator natural frequency, ω_c, should be equal to the system natural frequency ω_s. This assumption was verified numerically. A typical example of this validation is a case with $\omega_s = 100$ rad/s, $\zeta_s = 0.015$ and $a_1 = a_2 = 1$.

A typical scalar gain value was selected to be $\gamma = 0.35$, then using classical optimization technique, the following compensator parameters were obtained:

$\zeta_{c,opt} = 0.296$

$\omega_{c.opt} = 100$ rad/s

This example is illustrated by Figure 6.2, which shows the values of the H_2 norm of the closed loop system about the optimal compensator parameters.

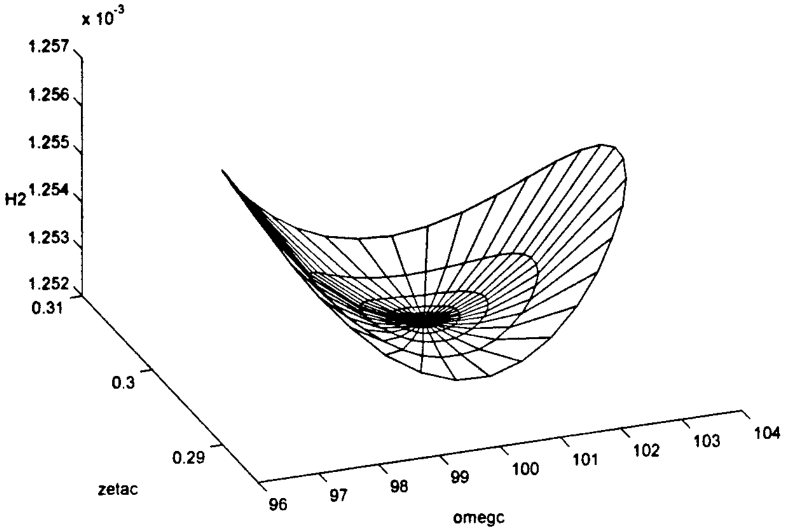

Figure 6.2. H_2 Optimal Parameters for Acceleration Feedback Control Compensator

VI.5. Multi-Mode Acceleration Feedback Control With A Single Actuator

It is often impossible to use a large array of sensors and actuators pairs to control the vibration of a structure. Furthermore, it is also often difficult to collocate these sensors and actuators exactly. In fact, for an Euler-Bernoulli cantilever beam, collocating an acceleration sensor and a piezoceramic actuator means that the location is not optimal for either the sensor or the actuator. For this beam, to obtain the maximum signal to noise ratio, the sensor should be placed at the free end of the beam. On the other hand, to obtain the best actuator authority, the actuator should be placed near the clamped end of the beam.

For a non-collocated single sensor, single actuator multi-mode acceleration feedback control, the spatial equations of motion of both the structure with feedback and external loads, and the compensator with the acceleration sensing component are:

$$\begin{cases} [M]\{\ddot{x}\}+[C]\{\dot{x}\}+[K]\{x\}=-\{\Gamma_{act}\}\lfloor G\rfloor[\Omega_c]\{\eta\}+\{f\} \\ \{\ddot{\eta}\}+[\Lambda_c]\{\dot{\eta}\}+[\Omega_c]\{\eta\}=\{1_p\}\lfloor\Gamma_{acc}\rfloor\{\ddot{x}\} \end{cases} \qquad (6.21.a\text{-}b)$$

Assuming that we only consider n locations, with n large enough so that all the necessary modes are included, $\{x\}$ is the vector of the n discretized spatial coordinates of the structure. [M], [C] and [K] are the inertia, damping and stiffness matrices, respectively. $\{\Gamma_{act}\}$ is the sensitivity and location vector of the actuator, meaning that it is zero everywhere but at the location of the actuator where it is equal to a_1. $\lfloor \Gamma_{acc} \rfloor$ is the sensitivity and location row vector of the sensor, meaning that it is zero everywhere but at the location of the sensor where it is equal to a_2. Assuming that we want to control p modes, $p \leq n$, $\{\eta\}$ are the p compensator coordinates. $[\Lambda_c] = \text{diag}(2\zeta_c\omega_c)$, $[\Omega_c] = \text{diag}(\omega_c^2)$ are the compensator damping and natural frequency matrices respectively. $\lfloor G \rfloor$ is the feedback scalar gain row vector. Finally, $\{1_p\}$ is a vector of length p with one for each entry so that all compensator are placed in parallel.

In this research, the general viscous damping [C] is not used. Instead, a modal damping $[\Lambda_s]$ is introduced after transformation into the modal space. Using the change of variable $\{x\} = [\Phi]\{\xi\}$, where $[\Phi]$ is the mass normalized mode shape matrix and $\{\xi\}$ are the n modal coordinates of the structure, and pre-multiplying the Equation (6.21.a) by $[\Phi]^T$, the modal closed-loop equations are obtained:

$$\begin{cases} \{\ddot{\xi}\} + [\Lambda_s]\{\dot{\xi}\} + [\Omega_s]\{\xi\} = -\{\tilde{\Gamma}_{act}\}\lfloor G \rfloor[\Omega_c]\{\eta\} + \{\tilde{f}\} \\ \{\ddot{\eta}\} + [\Lambda_c]\{\dot{\eta}\} + [\Omega_c]\{\eta\} = \{1_p\}\lfloor \tilde{\Gamma}_{acc} \rfloor\{\ddot{\xi}\} \end{cases} \qquad (6.22.a\text{-}b)$$

Where $[\Lambda_s] = \text{diag}(2\zeta_s\omega_s)$, is the modal damping matrix for the structure; $[\Omega_s] = \text{diag}(\omega_s^2)$ is the diagonal matrix of the structural natural frequencies; $\{\tilde{\Gamma}_{act}\} = [\Phi]^T\{\Gamma_{act}\}$ is the modal sensitivity vector of the actuator; $\lfloor \tilde{\Gamma}_{acc} \rfloor = \lfloor \Gamma_{acc} \rfloor[\Phi]$ is the modal sensitivity row vector of the sensor; and $\{\tilde{f}\} = [\Phi]^T\{f\}$ are the modal forces.

By taking the Laplace Transform of equations (6.22.a-b), assuming zero initial conditions, and solving for η which is substituted into (6.22.b):

$$\begin{cases} \left([I_n]s^2 + [\Lambda_s]s + [\Omega_s] + \{\tilde{\Gamma}_{act}\}\lfloor G \rfloor[\Omega_c]\left([I_p]s^2 + [\Lambda_c]s + [\Omega_c]\right)^{-1}\{1_p\}\lfloor \tilde{\Gamma}_{acc} \rfloor s^2\right)\{\bar{\xi}\} = \{\bar{\tilde{f}}\} \\ \{\bar{\eta}\} = \left([I_p]s^2 + [\Lambda_c]s + [\Omega_c]\right)^{-1}\{1_p\}\lfloor \tilde{\Gamma}_{acc} \rfloor s^2\{\bar{\xi}\} \end{cases} \qquad (6.23.a\text{-}b)$$

Since the second term of Equation (6.23.a) is composed of a row vector that multiplies a diagonal matrix times a column vector, it can be rewritten as:

$$\lfloor G \rfloor [\Omega_c]\left([I_p]s^2 + [\Lambda_c]s + [\Omega_c]\right)^{-1}\{1_p\}s^2 = \sum_{i=1}^{p} \frac{g_i \omega_{ci}^2 s^2}{s^2 + 2\zeta_{ci}\omega_{ci}s + \omega_{ci}^2} \tag{6.24}$$

where, g_i are the entries of the row vector $\lfloor G \rfloor$. Then, the Equation (6.23.a), which describes the closed-loop behavior of the structure, becomes:

$$\left([I_n]s^2 + [\Lambda_s]s + [\Omega_s] + \{\tilde{\Gamma}_{act}\}\lfloor \tilde{\Gamma}_{acc} \rfloor \left(\sum_{i=1}^{p} \frac{g_i \omega_{ci}^2 s^2}{s^2 + 2\zeta_{ci}\omega_{ci}s + \omega_{ci}^2}\right)\right)\{\bar{\xi}\} = \{\bar{\bar{f}}\} \tag{6.25}$$

Without loss of generality, one can rearrange the row order of the above system of equations such that the first p rows correspond to the p modes that one would want to control, we can separate the system of equations as shown by equations (6.26.a-b).

$$\begin{gathered}\left(s^2 + 2\zeta_{s,k}\omega_{s,k}s + \omega_{s,k}^2 + \frac{\Gamma_{act,k}\Gamma_{acc,k}g_k\omega_{c,k}^2 s^2}{s^2 + 2\zeta_{c,k}\omega_{c,k}s + \omega_{c,k}^2} + \Gamma_{act,k}\Gamma_{acc,k}\sum_{\substack{i=1\\ i\neq k}}^{p} \frac{g_i\omega_{c,i}^2 s^2}{s^2 + 2\zeta_{c,i}\omega_{c,i}s + \omega_{c,i}^2}\right)\bar{\xi}_k \\ + \Gamma_{act,k}\sum_{\substack{j=1\\ j\neq k}}^{n}\Gamma_{acc,j}\left(\sum_{l=1}^{p}\frac{g_l\omega_{c,l}^2 s^2}{s^2 + 2\zeta_{c,l}\omega_{c,l}s + \omega_{c,l}^2}\right)\bar{\xi}_j = \bar{\bar{f}}_k, \quad k = 1,\dots,p\end{gathered} \tag{6.26.a}$$

$$\begin{gathered}\left(s^2 + 2\zeta_{s,k}\omega_{s,k}s + \omega_{s,k}^2 + \Gamma_{act,k}\Gamma_{acc,k}\sum_{i=1}^{p} \frac{g_i\omega_{c,i}^2 s^2}{s^2 + 2\zeta_{c,i}\omega_{c,i}s + \omega_{c,i}^2}\right)\bar{\xi}_k \\ + \Gamma_{act,k}\sum_{\substack{j=1\\ j\neq k}}^{n}\Gamma_{acc,j}\left(\sum_{l=1}^{p}\frac{g_l\omega_{c,l}^2 s^2}{s^2 + 2\zeta_{c,l}\omega_{c,l}s + \omega_{c,l}^2}\right)\bar{\xi}_j = \bar{\bar{f}}_k, \quad k = p+1,\dots,n\end{gathered} \tag{6.26.b}$$

By making each compensator design selective, which means that each compensator targets a single mode and has a damping value small enough such that the spillover effects are minimal and negligible, the following equations result:

$$\begin{gathered}\left(s^2 + 2\zeta_{s,k}\omega_{s,k}s + \omega_{s,k}^2 + \frac{\Gamma_{act,k}\Gamma_{acc,k}g_k\omega_{c,k}^2 s^2}{s^2 + 2\zeta_{c,k}\omega_{c,k}s + \omega_{c,k}^2}\right)\bar{\xi}_k = \bar{\bar{f}}_k, \\ k = 1,\dots,p \\ \left(s^2 + 2\zeta_{s,k}\omega_{s,k}s + \omega_{s,k}^2\right)\bar{\xi}_k = \bar{\bar{f}}_k, \quad k = p+1,\dots,n\end{gathered} \tag{20.a-b}$$

As a result, each compensator can be designed independently using either the crossover design procedure or the H_2 design methodology. In continuous structures, due to the spillover effects, neither the crossover conditions nor the single degree of freedom H_2 optimization will be exactly satisfied when loop is closed on the actual system. However, the selectivity of each compensator ensures that the conditions are nearly satisfied.

Once each compensator is designed, the stability of the system should be checked. If the spillover effects are negligible, the system is unconditionally stable since it is made of n independent unconditionally stable systems. In practical design, this assumption is not always met. In this research, the stability is checked by using the root locus procedure.

VII. VALIDATION ON VERTICAL TAIL SUBASSEMBLY

VII.1. Plant Model for the Vertical Tail

Instead of using a finite element model for the plant, which would have required a large number of nodes, experimentally identified transfer functions are used for the mathematical model of the vertical tail . In general, we need a transfer function matrix to represent the plant model for the vertical tail subassembly because we have a distributed parameter system. In such a distributed parameter system, a reduction of tip vibration will also reduce vibrations in the rest of the system. Thus we can effectively control vibrations in the entire vertical tail assembly by using a small subset of the entire transfer function matrix provided all the important modes of the system are represented in the subject.

To obtain the experimental transfer function, a random signal is input to the actuator and the control sensor is used to measure the acceleration response. The measure of the input signal is taken from the signal generator so that the dynamics of the actuator are included in the model. The instrumentation system of this part of the experiment is illustrated in Figure 7.1.

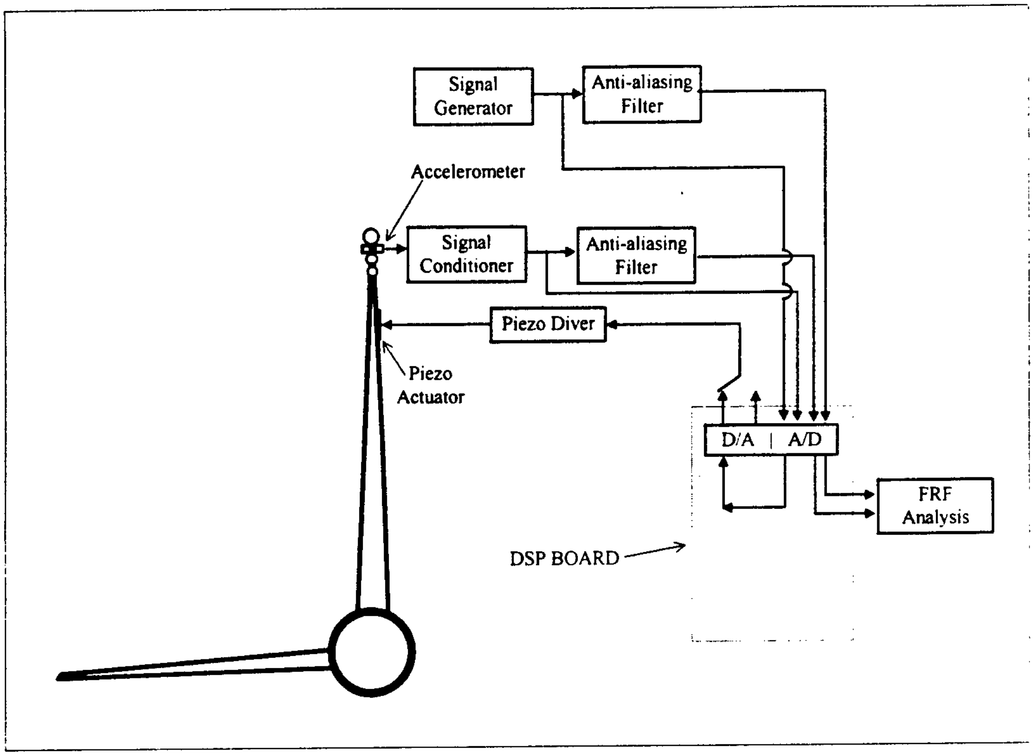
Signal Generator
Anti-aliasing Filter
Accelerometer
Signal Conditioner
Anti-aliasing Filter
Piezo Diver
Piezo Actuator
D/A
A/D
FRF Analysis
DSP BOARD

Figure 7.1. Experimental Wiring for Obtaining the Model of the Plant

The experimental data are processed through a system identification scheme to extract the modal parameters. The mathematical representation of the transfer function is in the form of a partial fraction expansion:

$$G_p(s) = \sum_i \frac{A_i s^2}{s^2 + 2\zeta_{s,i}\omega_{s,i}s + \omega_{s,i}^2} \tag{7.1}$$

The modal parameters of the plant are given in table 7.1. A comparison between the plot of experimental transfer function and the modeled transfer function is illustrated on figure 7.2.

Modes	Natural Frequency $\omega_{s,i}$ (rad/s)	Damping Ratio $\zeta_{s,i}$	Residue A_i (10^{-4})
First Bending	65.37	0.0155	1.849
Vertical/Horizontal Tails Interaction	115.36	0.0125	2.023

First Torsion	236.37	0.0055	-35.282
Plate Mode with Diagonal Node Line	244.40	0.0055	-21.876
Second Bending	388.08	0.004	-5.364

Table 7.1 Modal Parameters of the Vertical Tails

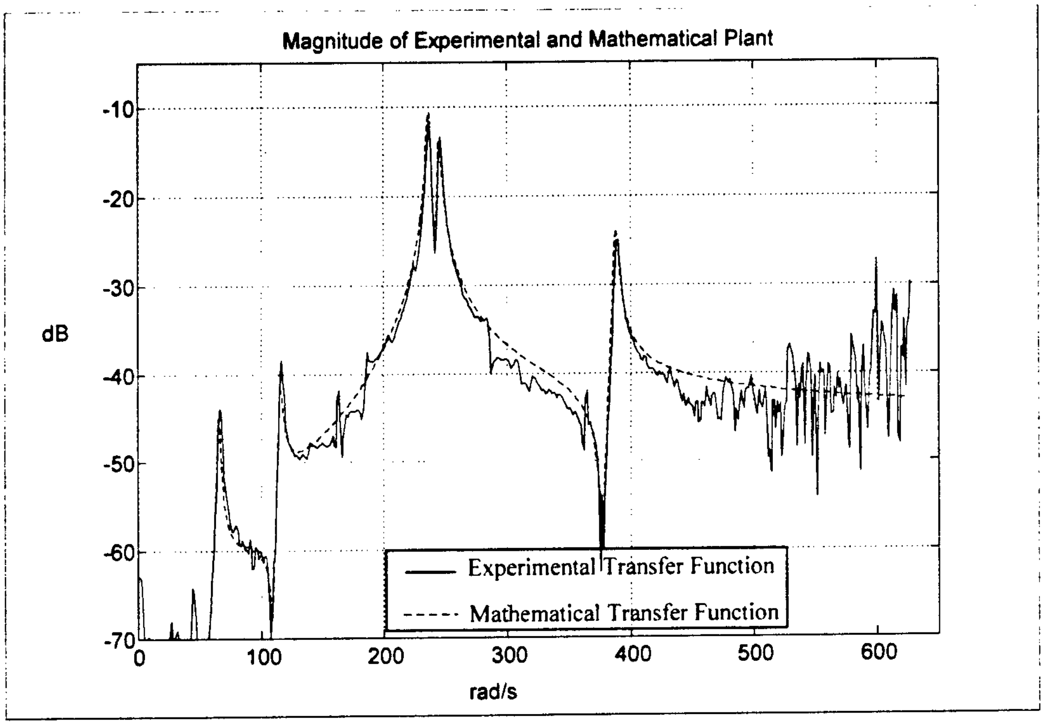

Figure 7.2. Comparison between Experimental and Modeled Plant Transfer Functions

VII.2. Vertical Tail Acceleration Feedback Controller Design

The design of the vertical tail vibration controller using an acceleration feedback control scheme is setup such that it will increase the damping in three modes using a single actuator. The three modes that are chosen are the first torsion, the plate mode with diagonal node line and the second bending mode of the vertical tail.

Each compensator is designed independently following the results discussed in Section VI. The type of single degree of freedom AFC is chosen to be the crossover design for all three modes.

The compensator parameters are computed with an initial choice of compensator damping ratio of about 10 time the modal damping coefficient of the open loop structure. Once each compensator is designed, a mathematical closed loop equation is formed following the classical feedback equation:

$$G_{cl}(s) = \frac{\displaystyle\sum_i \frac{A_i s^2}{s^2 + 2\zeta_{s,i}\omega_{s,i}s + \omega_{s,i}^2}}{1 - \left(\displaystyle\sum_i \frac{A_i s^2}{s^2 + 2\zeta_{s,i}\omega_{s,i}s + \omega_{s,i}^2}\right)\left(\displaystyle\sum_{k=1}^{3} \frac{-g_k \omega_{c,k}^2}{s^2 + 2\zeta_{c,k}\omega_{c,k}s + \omega_{c,k}^2}\right)} \tag{7.2}$$

It is noted that the A_i's are equal to the $\Gamma_{acc,i}\Gamma_{act,i}$'s so that one can design compensators using equations from Section VI. Using equation (7.2), the control effectiveness is checked and the compensators are slightly tuned to optimize their effectiveness. The resulting parameters are given in table 7.2.

Compensators	Natural Frequency $\omega_{c.k}$ (rad/s)	Damping Ratio $\zeta_{c.k}$	Scalar Gain g_k
First	226.92	0.08	-1.5731
Second	251.73	0.08	-2.5371
Third	388.08	0.05	-3.9447

Table 7.2. Compensator Parameters

The stability of the closed loop system is verified using a root locus plot, which is shown on Figure 7.3.

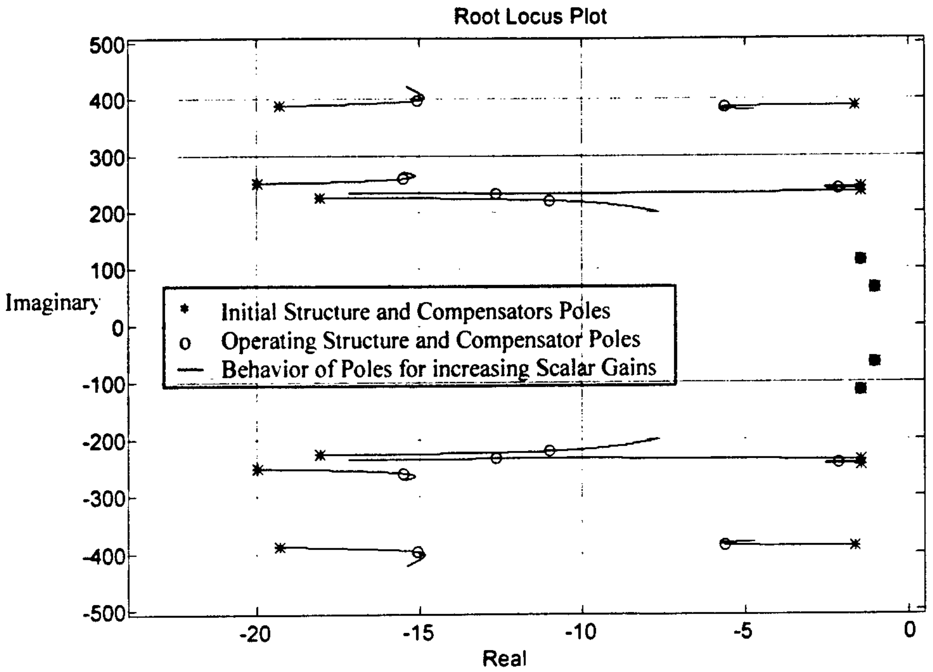

Figure 7.3 Root Locus Plot

VII.3. Experimental Setup for the Acceleration Feedback Control of the Vertical Tail Subassembly

In this experiment, the piezoceramic stack actuators are selected for the generation of both the disturbance and the control forces. The instrumentation used for the experimental control of the vertical tail is shown in figure 7.4. It includes the following equipment:

- A Waveteck Model 132 Signal Generator provides the random signal used as the disturbance source,
- Two PI P-830.40 Piezoceramic Stack Actuators, that are collocated with respect to each other and considered as a single actuator, provide the control forces, both are electrically preloaded to enable both compressive and tensile load to transmitted,
- A PI P-863 Piezo Driver conditions and amplifies the signal driving the actuators.
- A PCB 308 B14 Accelerometer senses the structure vibration and drives the feedback loop,

- A PCB 408D06 Power Unit conditions and amplifies the sensor signal,
- Two Krohn-Hite 3343 Filters set to low pass filter are used as anti-aliasing filters and condition the signal for post processing analysis,
- A dSPACE DS2001 High Resolution ADC Board digitizes the analog signals coming from the signal generator and the sensor,
- A dSPACE DS1004 Alpha Board based on a DEC Alpha AXP 21164 processor implement the controller online at a frequency of 10 kHz,
- A dSPACE DS2101 D/A Board generates the feedback control signal.

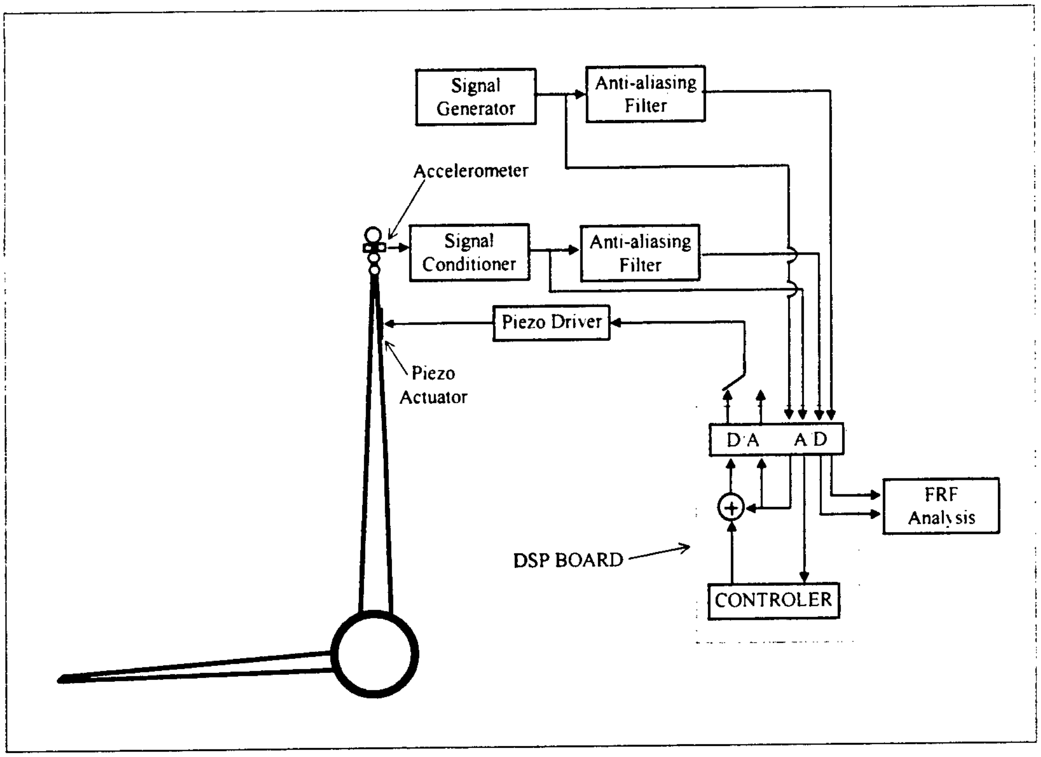
Signal Generator
Anti-aliasing Filter
Accelerometer
Signal Conditioner
Anti-aliasing Filter
Piezo Driver
Piezo Actuator
D/A
A/D
FRF Analysis
DSP BOARD
CONTROLER

Figure 7.4. Wiring of the experimental control of vertical tail

The controller is designed using Matlab and Simulink. The controller parameters having already being selected, they are introduced into block objects, such as a transfer function block, in Simulink. Then, appropriate connection are selected and drawn. Once the Simulink file is created, the Real Time Workshop and the Real Time Interface of dSPACE are used to generate a C code of the controller, which is translated to a machine language code that is download to the DSP board. Once the program is resident into the DSP memory, the controller runs by itself.

VII.4. Results

The results of the experiment are given in Figure 7.5. The reduction in amplitude of the three modes of interest are clear, the first torsion mode and the local bending mode have both been reduced by about 15 dB which translate into a reduction by more than 80%. The second bending mode has been reduced by about 10 dB, so that the peak is reduced by 70%. Simultaneously, the uncontrolled modes, namely the first bending and the vertical/horizontal tails interaction have been left unchanged by the control. The higher modes and their dynamics have not been changed.

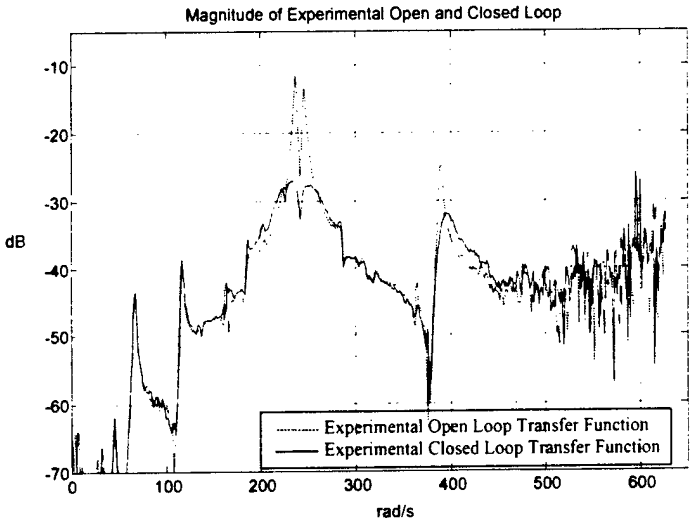

Figure 7.5. Comparison between experimental open and closed loop transfer functions

VIII. STRUCTURAL DYNAMIC SCALE MODEL, FINITE AMPLITUDE VIBRATION CONTROL AND NONLINEAR EFFECTS

VIII.1. One-Sixteenth Structural Dynamic Scale Model Construction

The structural dynamically similar one-sixteenth scale model of the subassembly consisting of the vertical tails is illustrated by Figure 8.1. The model consists of two vertical tails, two horizontal stabilators, and the aft fuselage boom structures. Materials used in the construction of this version of the model are as follows:

- The vertical tails are made from three layers of glass-fiber woven cloth and epoxy matrix composite plates. Graphite epoxy composite beams are used to represent the spars of the structure. The tip pods are simulated by using copper tubes filled with lead.

- The horizontal stabilators are made from three layers of glass fiber woven cloth and epoxy matrix composite plates. The stabilators are strengthened by a composite patch at the root. Graphite epoxy composite beams are used as spars.

- The boom structures are represented by two pieces of wood.

- The engine mounts are simulated by two PVC tubes. The tube walls are hollow to represent the framed engine supporting structures.

The model was assembled using wood screws and then mounted on a heavy vice. The structural dynamic similarity was fine-tuned by attaching non-structural masses to the structure. The current similarity between 1/16-scale model and the full-scale F-15 vertical tail subassembly is shown in Table 8.1

1/16 Scale Model	F15	Mode Properties
~ 9.50 Hz	~ 10.3 Hz	First bending of vertical tails
~ 18.5 Hz	~ 18.55 Hz	First bending of horizontal stabilators
~ 45.0 Hz	37.89-39.06 Hz	First twist of vertical tails and coupling modes

Table 8.1. Model Structural Dynamic Similarity

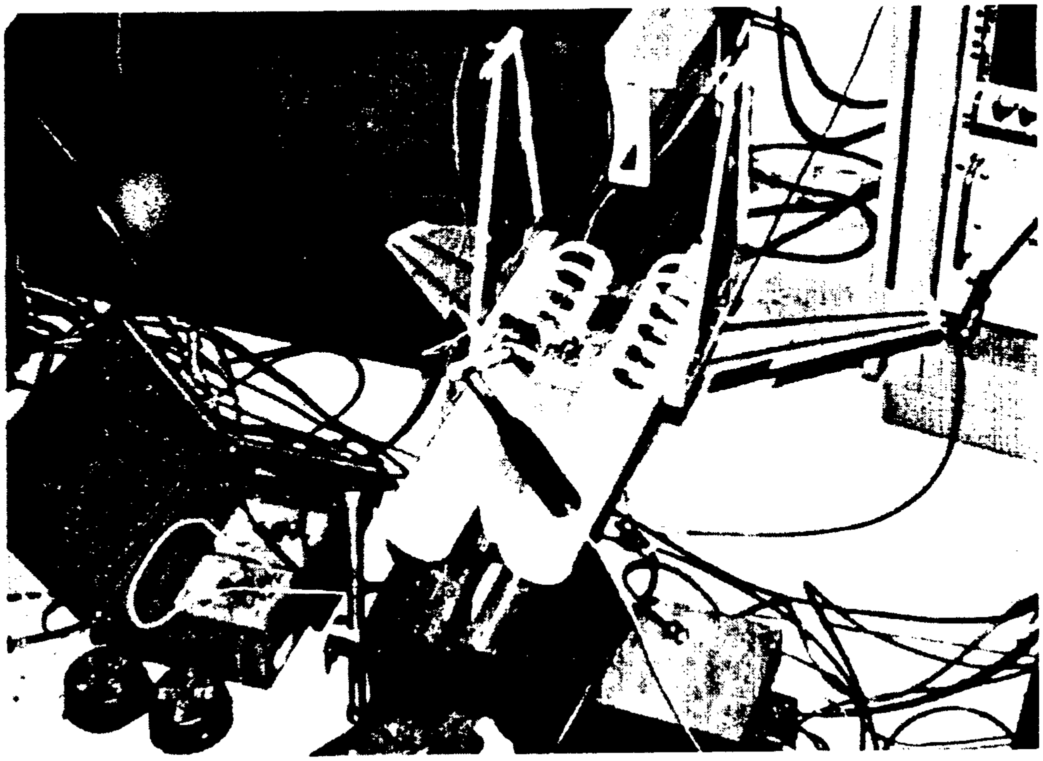

Figure 8.1. Structural Dynamic Scale Model

VIII.2. Finite Amplitude Vibration Control of the 1/16 Scale Model Under Excitations due to Air Flow

The instrumentation of the wind induced finite amplitude vibration control is shown in Figure 8.2. In the experiments, the excitation was provided by a high velocity fan. A PCB 303 A02 accelerometer was used as response sensor, which was fixed at the tip of the vertical tail. The Acceleration signal was conditioned by a PCB power unit (PCB Model 480 D06 Power Unit). The sensor signal was digitized by the A/D converter of the DSP board. Numerical compensator was implemented using Simulink programming. The controller was designed the same as the one reported in Progress Report IX. Since the response signal is dominated by first vertical tails bending modes in this wind induced vibration control, only first vertical bending modes were controlled. The numerical compensator digital signal was transferred to analog form by the D/A component of the DSP board. The analog compensation was amplified by a power amplifier (KROHN-HITE 50 watts amplifier Model DCA-50R) and then input to the piezo ceramic actuators.

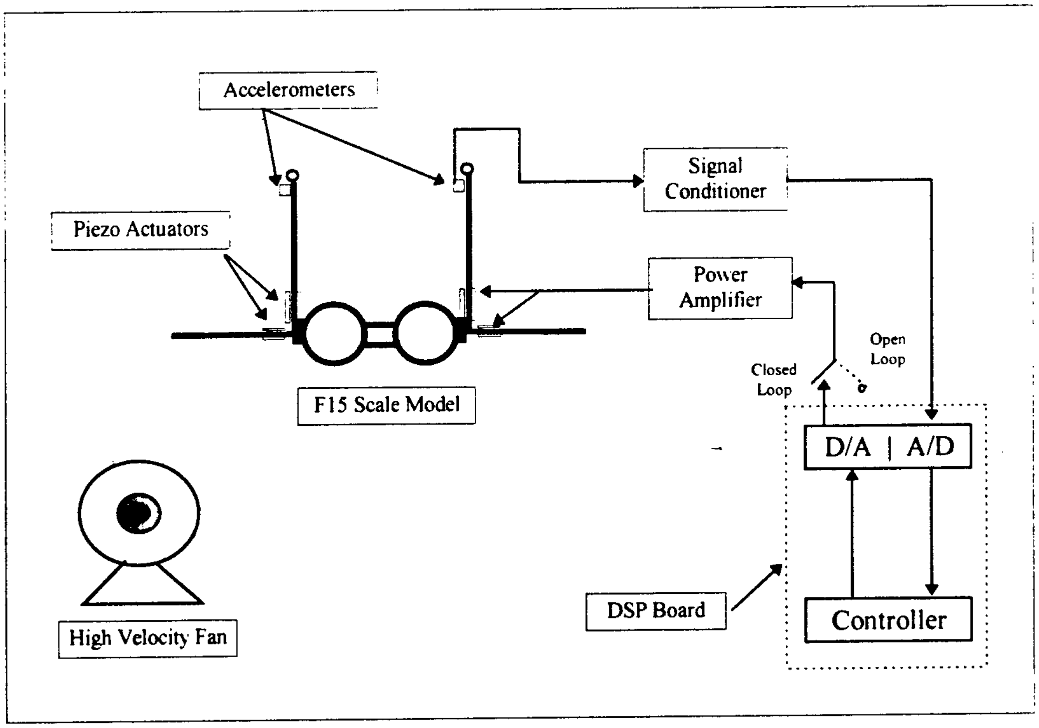
Accelerometers
Signal Conditioner
Piezo Actuators
Power Amplifier
Open Loop
Closed Loop
F15 Scale Model
D/A | A/D
DSP Board
Controller
High Velocity Fan

Figure 8.2. Instrumentation for Wind Induced Finite Vibration Control

Control Implementation and Experimental Results

1. Open loop tests:

- Turn the high velocity fan on;
- Wait for a while until the excitation and the vibrations are stabilized;
- Start the A/D converter for data acquisition;
- Save the digitized data for further analysis.

2. Closed loop tests:

- Close the control loop;
- Adjust the power amplifier gain;
- Start the A/D converter for data acquisition;
- Record the data for further analysis.

Under the high velocity wind induced excitation, the finite amplitude vibrations were excited. As shown in Figure 8.3, the open loop vibration acceleration level reached 10.0 m/s^2 peak-to-peak level with the dominate frequency at 10 Hz. This vibration level, in terms of displacement, had about 2.5mm peak-to-peak displacement amplitude.

After the control loop is closed, as can be seen from Figure 8.3, the vibration level of the first frequency component decreases significantly. It is to be noted that the time histories in Figure 8.3 reflect only the general trends of the vibration levels of open and closed control loops. The excitations were induced by the fan blowing, they can not be exactly repeated.

Control effects of the finite amplitude vibration control can be better reviewed in the frequency domain. As can be seen in the decibel scale (Figure 8.4) and linear scale (Figure 8.5). Significant control effect has been achieved in the finite amplitude vibration induced by a fan. About 20 dB (90 percent) vibration reduction has been achieved.

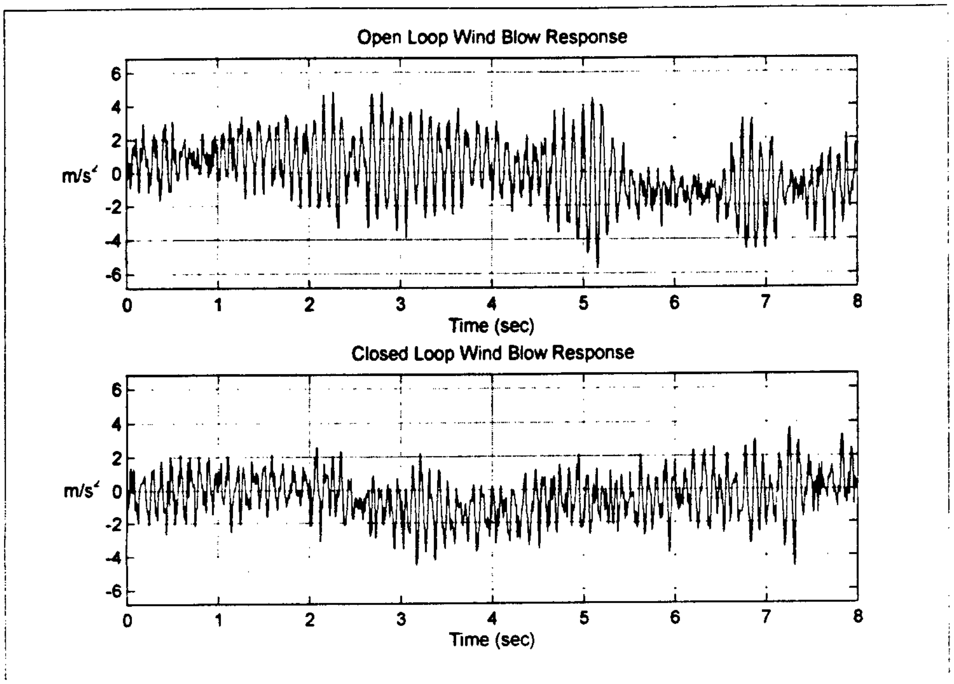

Figure 8.3. Vibration responses of open and closed control loop

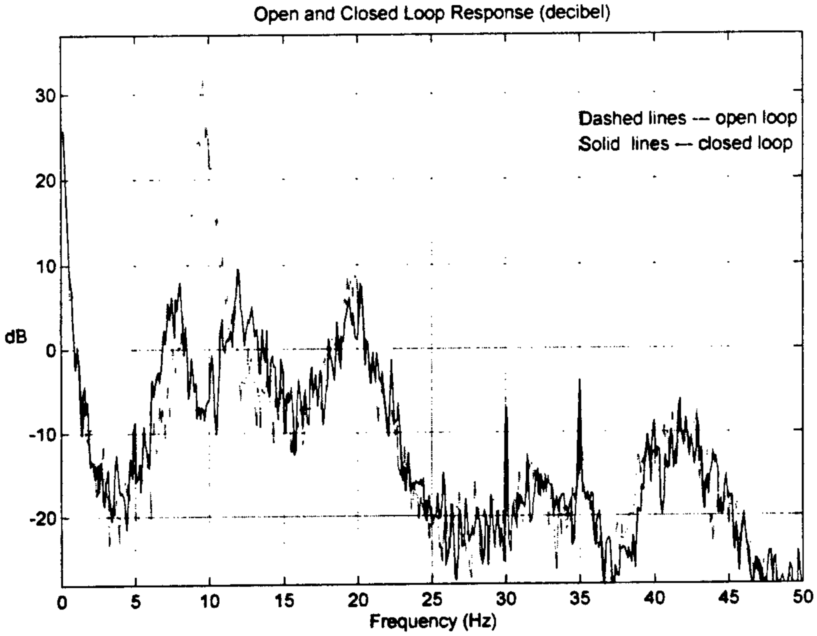

Figure 8.4. Finite amplitude vibration control effect (decibel scale)

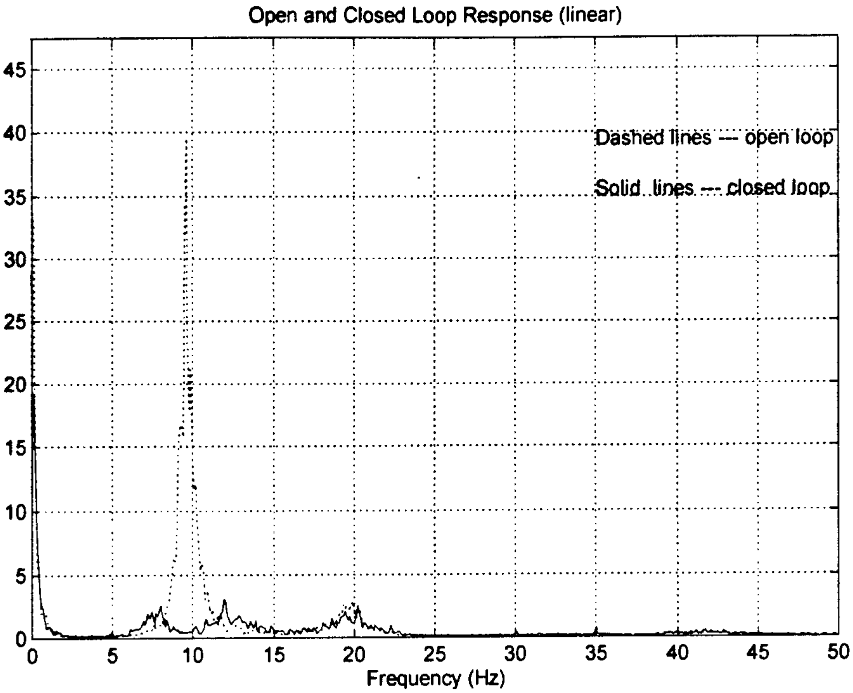

Figure 8.5. Finite amplitude vibration control effect (linear scale)

Through the experiments of controlling the finite amplitude vibration induced by a blowing fan, several conclusions can be made, which provide guidelines for future wind tunnel testing:

1. Finite amplitude vibration in a 1/16 scale model can be excited by a fan. The equivalent displacement amplitude achieved in the experiment was about 2.5mm peak-to-peak. This amplitude is equivalent to the 1.5 inch displacement in a real structure. For wind tunnel testing, the vibration amplitude are expected to be higher and the high frequency modes are expected to be excited due to the excitations from the vortex breakdown. Thus a broad band and high level excitations are expected in the wind tunnel testing.

2. The AFC controllers designed are effective in controlling the finite amplitude vibrations. The design methodology can be used to control vibrations in the wind tunnel testing.

3. The PVC tubes provide higher damping than the damping realized in a metallic structure. For wind tunnel tests, we intend to change the boom to a metallic boom.

VIII.3. Nonlinear Studies

The instrumentation of the preliminary nonlinear research is shown in Figure 8.6.

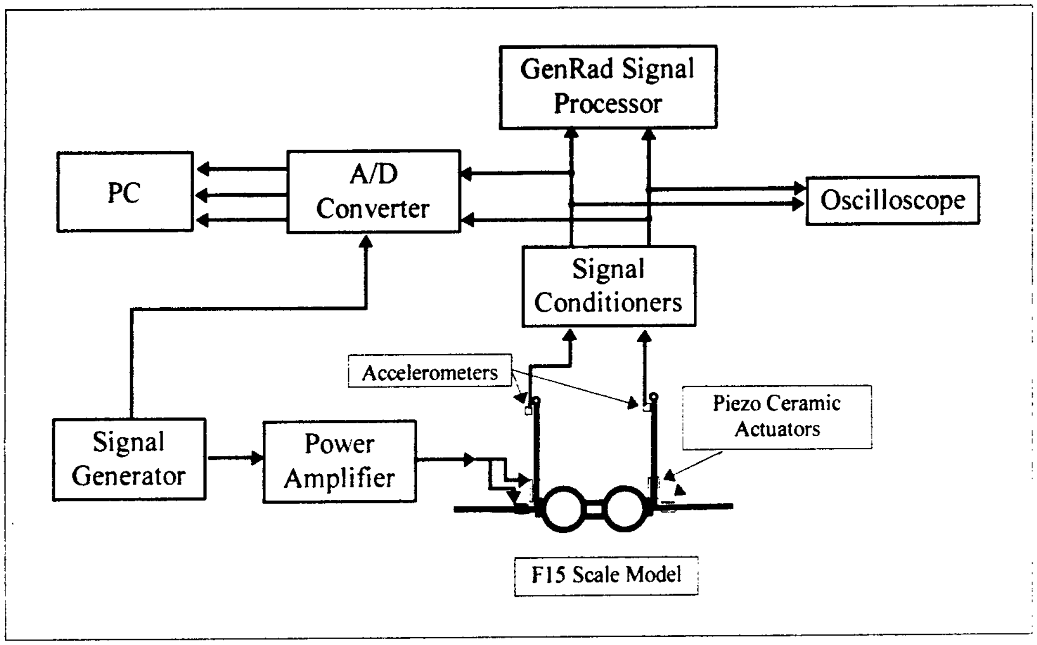
GenRad Signal Processor
PC
A/D Converter
Oscilloscope
Signal Conditioners
Accelerometers
Piezo Ceramic Actuators
Signal Generator
Power Amplifier
F15 Scale Model

Figure 8.6. Nonlinear Vibration Instrumentation

In preliminary experiments, a pure sinusoidal signal at given frequency is generated by a signal generator. The signal is then amplified by a power amplifier before it is fed to the piezoceramic actuators. The dynamic response signals of the scale model structure are detected by two PCB accelerometers mounted on the top of the vertical tails. The response signals are conditioned by PCB signal conditioners to amplify the signal. The signals can be visualized by oscilloscope. The frequency information of the response signals is analyzed by a GenRad computer aided signal processing system. The signal can also be documented in a PC following an A/D converter digitization.

Several nonlinear phenomena are observed in these experiments. For example, when a 13.0 Hz sinusoidal excitation is input to actuators on the horizontal stabilators symmetrically, the response exhibits significant nonlinear effects, as shown in Figure 8.7.

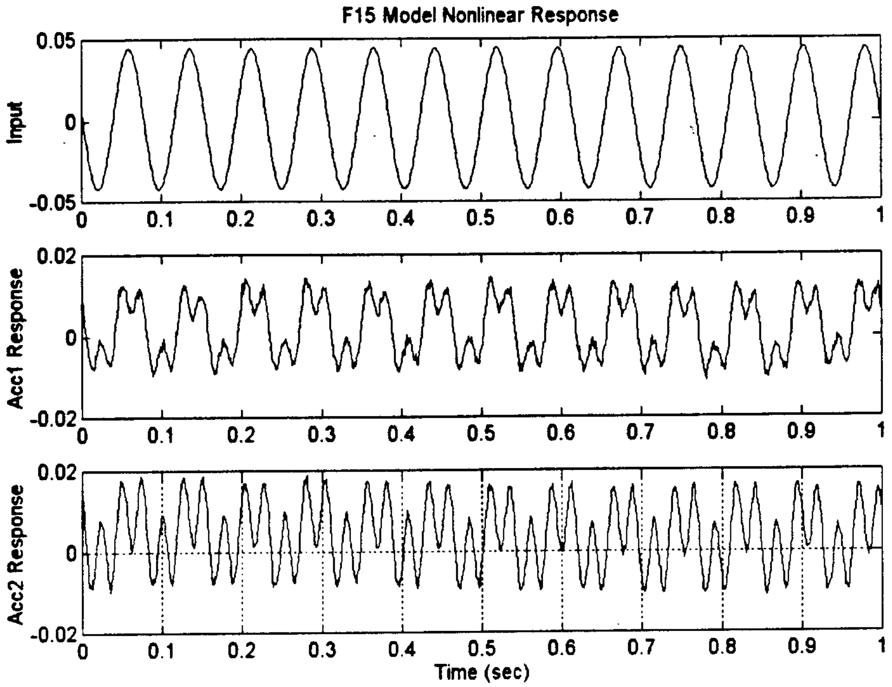

Figure 8.7. Excitation frequency f=13.0 Hz. Actuators on horizontal wings with antisymmetric excitation

In the Figure 8.7, the "Input" indicates the input signal to the actuators. The "Acc1 Response" is the response signal observed by the right (viewed from the tail to head of the plane) vertical tail accelerometer, while the "Acc2 Response" is the response signal observed by left vertical tail accelerometer. From Figure 8.7, we can see the nonlinear effects in the response.

Similarly, such nonlinearities are found in different excitation combinations. For example, when the excitation frequency is at 26.0 Hz, when both horizontal stabilators are symmetrically excited, the nonlinear effects are detected (see Figure 8.8). While the excitation is at 21.5 Hz, richer nonlinear effects are detected by exciting the left horizontal stabilator and the left vertical tail (see Figure 8.9).

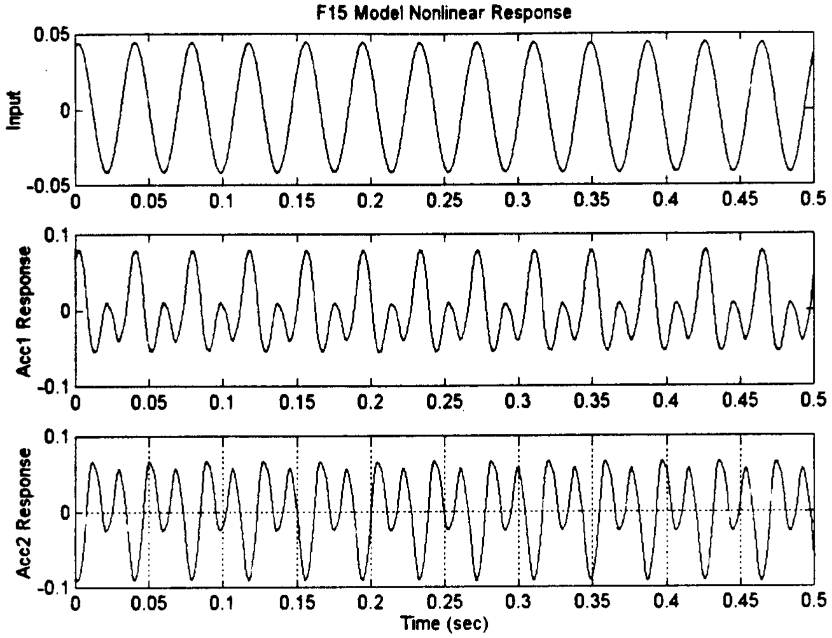

Figure 8.8. Excitation frequency f=26.0 Hz. Actuators on horizontal stabilators with symmetric excitation

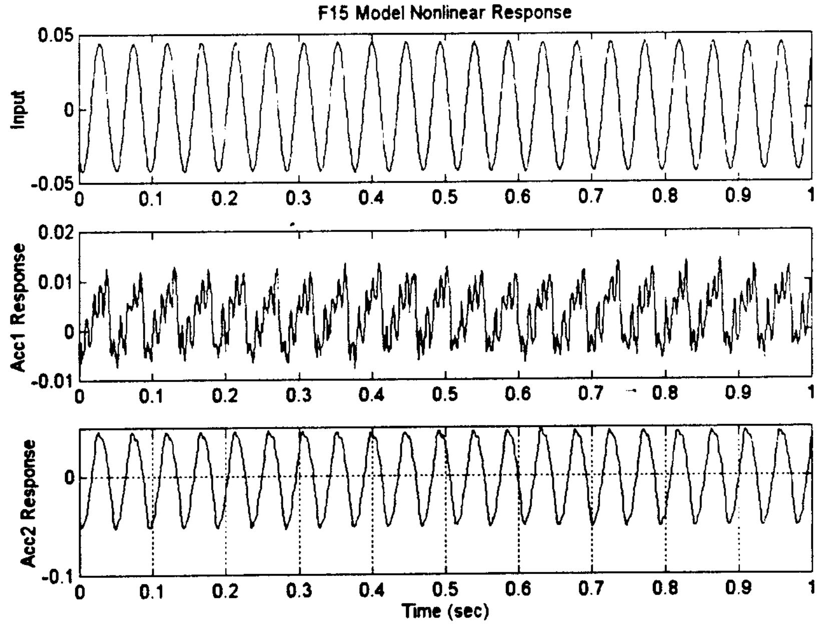

Figure 8.9 Excitation frequency f=21.5 Hz. Actuators on a horizontal stabilator and a vertical tail with symmetric excitation

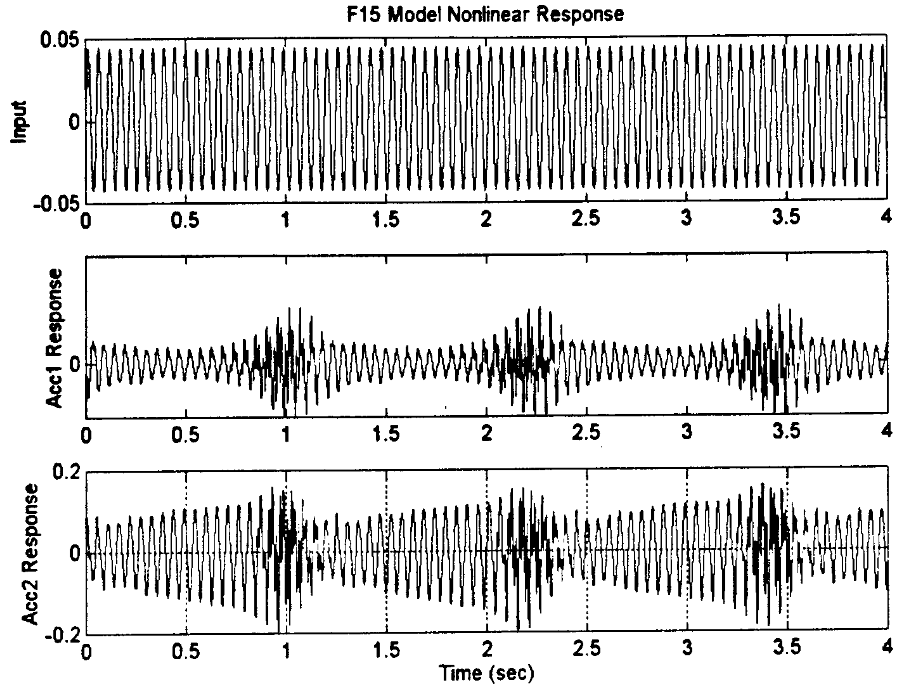

Figure 8.10. Excitation frequency f=18.4 Hz. Actuators on horizontal stabilators and vertical tails with symmetric excitation

When the excitation frequency is 18.4 Hz and applied to all actuators on the vertical tails and horizontal stabilators, a typical nonlinear frequency modulation is detected as shown in Figure 8.10. This nonlinear effect can be confirmed in frequency domain as shown in Figure 8.11. A zoomed frequency (10 Hz - 26 Hz) analysis is shown in Figure 8.12.

As stated before, when the excitation frequency is around 18.4 Hz, a typical nonlinear frequency modulation was detected. We have repeated the experiments to obtain this nonlinear phenomenon, and Poincare Maps of the nonlinear response are detected experimentally. In Figure 8.13, we have shown the "Poincare Maps" of the signals from the accelerometers from the left and right vertical tails.

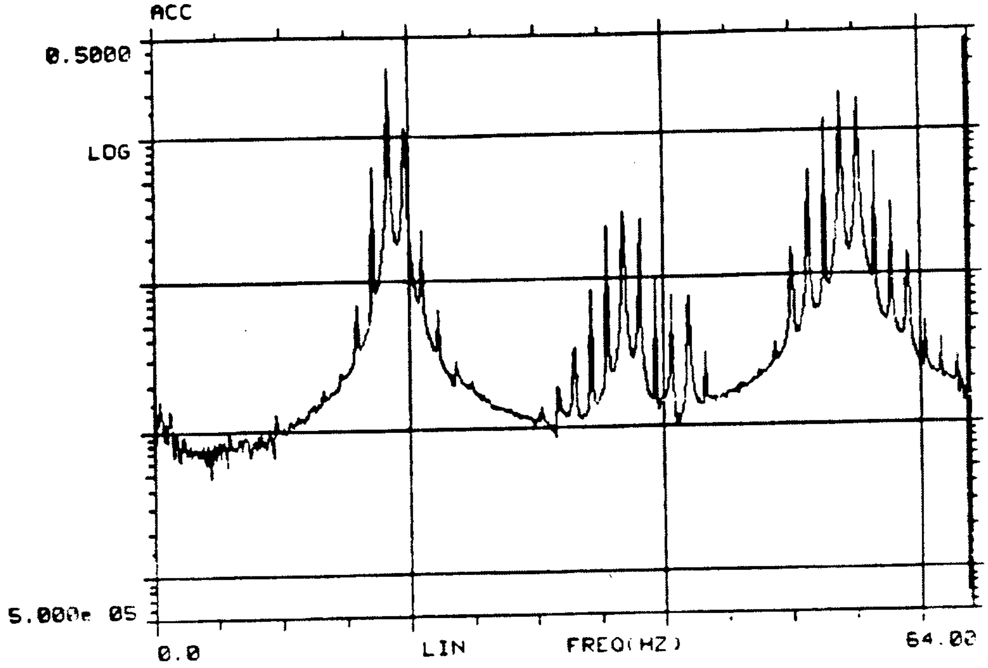

Figure 8.11. Frequency analysis of frequency modulation

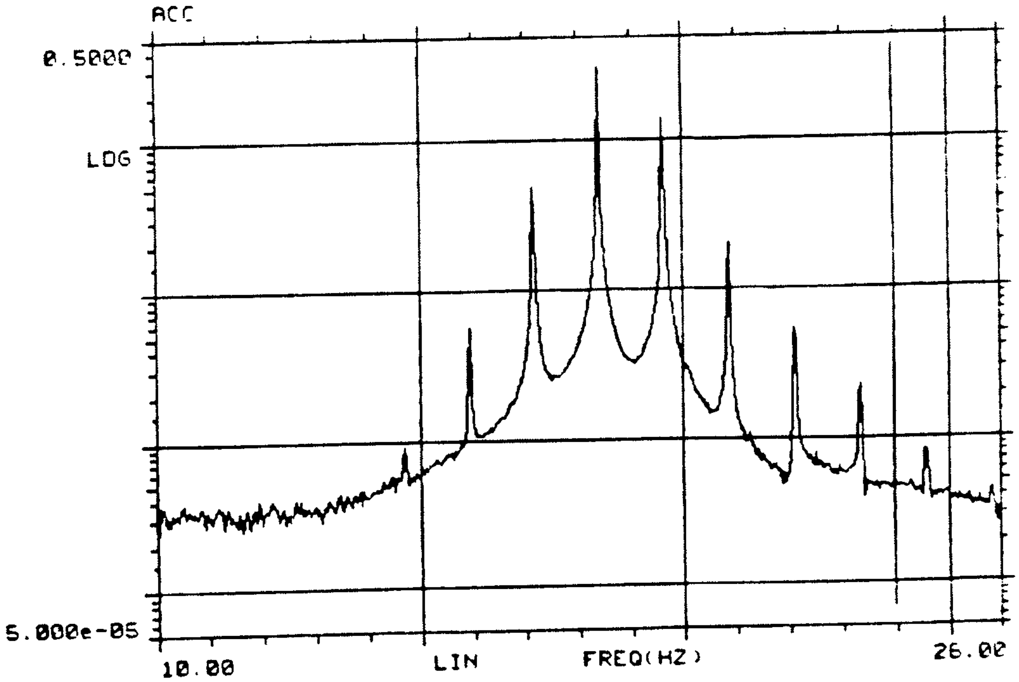

Figure 8.12. Zoomed Frequency analysis

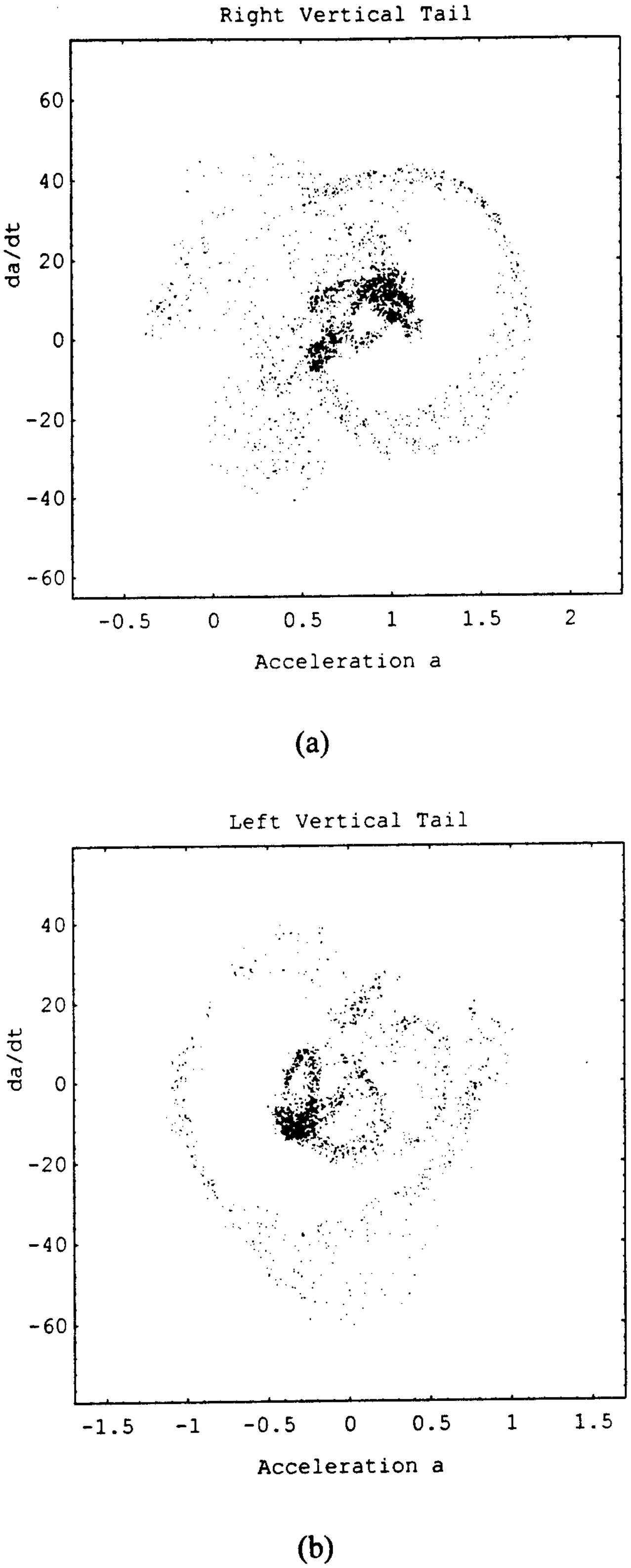

Figure 8.13. "Poincare Maps". (a) From Right Vertical Tail, (b) From Left Vertical Tail

Since we have used accelerometers as our dynamic sensors, the Poincare Maps shown in Figure 8.13 are not of the conventional map in the state space sense. We actually used acceleration as the horizontal axis and the time derivative of the acceleration as the vertical axis. A total of 3,031 points is used in each "Poincare Map." The "Poincare Map" shown in Figure 8.13 indicated the chaotic behaviors of the dynamic response.

IX. AEROELASTIC SCALE MODEL DESIGN AND CONSTRUCTION

IX.1. Rigid Body Part of Scale Model: Fuselage and Wings

The rigid part of the wind tunnel scale model consists of the fuselage and the wings. This part of the model was constructed from a precut model of the F-15 aircraft made by Combat Models Inc. The precut foam based model was used only to provide the geometrical dimensions. The tail section of that model was removed to allow the attachment of an aeroelastically scaled empenage.

Reinforcements were added to the center section of the fuselage. A fiberglass matting and an aluminum tube provide the main load carrying structure for the model. As shown in figure 9.1, the tube runs the length of the center fuselage and is the structural member to which the aeroelastically scaled tail section attaches. Finally, a steel piece was designed to allow connection on the tube on one side and connection to the wind tunnel stinger on the other side. The fiberglass matting was installed to provide a good surface for distributing the stresses that are generated at the connection between the tube and the fuselage.

The exterior of the fuselage was also reinforced. This reinforcement was made of carbon fiber strips as shown on figure 9.1. Finally, some fiberglass was overlaid to the top and bottom of the entire model. Two-hour epoxy was used for all the lay-ups and was left to cure for twenty-four hours.

The last step in finishing the rigid part of the model was to smooth the contours of the wings and the fuselage. This smoothing was realized by coating the model with many layers of spackle and fine sanding of each layer. When the desired level of smoothness was obtained, some gray sandable primer was sprayed on the model. At this step, all small imperfections of the model became apparent and the model was sanded again. Finally, the model was painted with a gray paint.

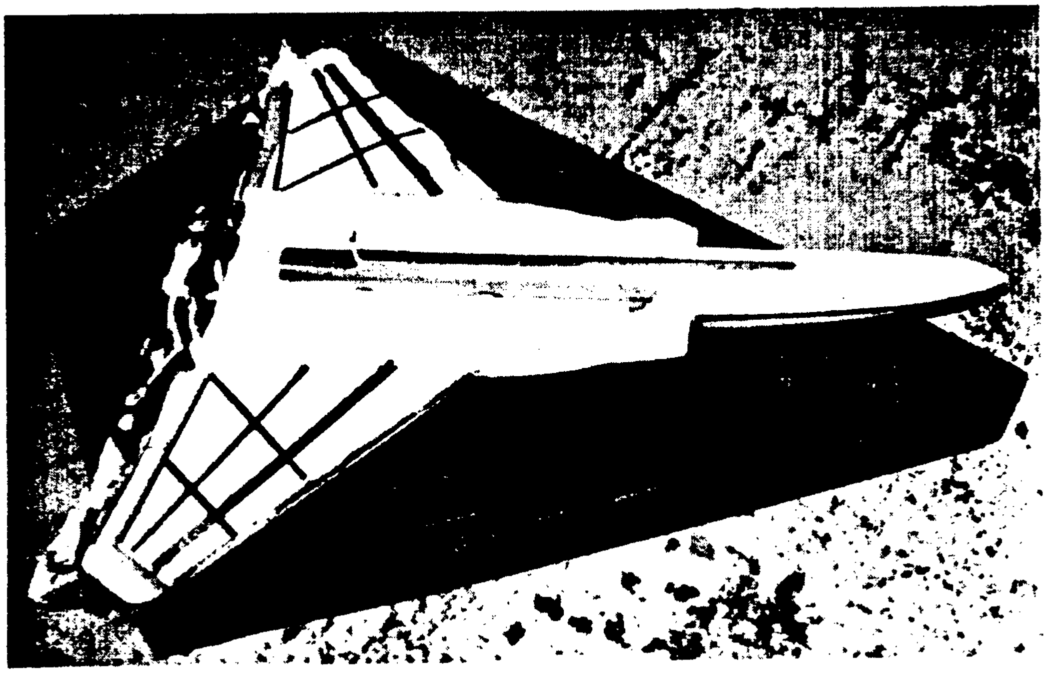

Figure 9.1. Inside of the Rigid Fuselage

IX.2. Frequency Matched Model (1 to 1 frequency ratio)

This model was built by using a trial and error method to obtain a tail section which frequencies matched to one of the full-scale tail section. The different models that were made are shown on figure 9.2. These models began with wood, PVC and composite materials to finish with aluminum, brass and composite materials.

The final version vertical tails, shown in figure 9.3, are made of two layers of fiberglass woven cloth and epoxy matrix composite plate. Some graphite epoxy composite strips are used to stiffen the structure and represent the spars inside the full scale vertical tails. Finally, the tip pods are made of tubes filled with some lead masses. The horizontal stabilators are made from three layers of fiberglass woven cloth and epoxy matrix composite plates with some tip tubes to adjust the frequencies. The boom structure is made of aluminum channels that are connected to each other by some copper rings simulating the engine fixtures. In this final version, the transfer of energy from the horizontal to the vertical tails resulted in a manner similar to the full-scale F-15 aircraft.

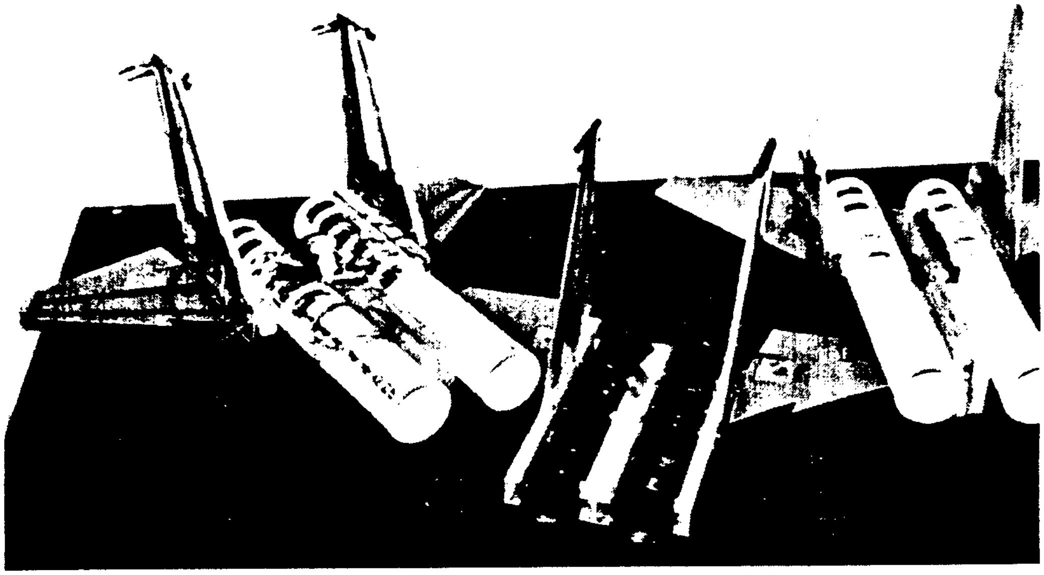

Figure 9.2. Evolution of the Frequency Matched Models

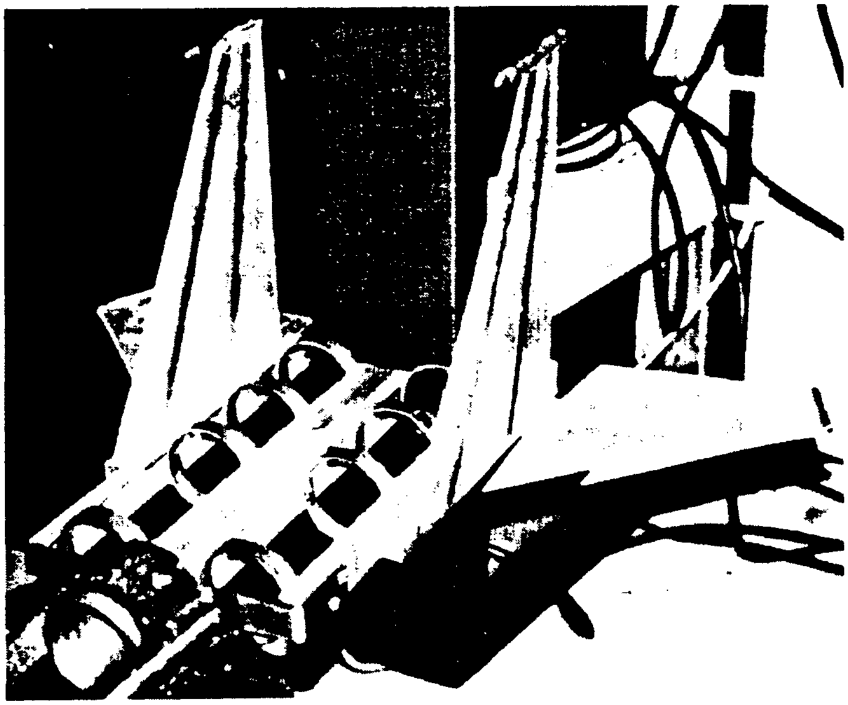

Figure 9.3. Frequency Matched Model and Connection to Rigid Model

IX.3. Scale Model (4 to 1 frequency ratio)

This complete design of the 4 to 1 frequency ratio scale model was completed based on a finite element approach using Matlab. The resulting design is shown on figure 9.4.

The scaled vertical tails are made of fiberglass cloth and epoxy matrix composite. There are nine plies at the root and each vertical tail is tapered regularly until only it reaches two plies at its tip. Two carbon fiber strips are bonded to the plate to simulate the spars of the actual vertical tail. Finally, tubes made of brass, for the 6" pod, and copper, for the 2" pod, are mounted on the tip of the vertical tails. The scaled 6" pod is filled with some lead masses to match the frequencies. This model has all the characteristics of the actual vertical tail including the two closed modes around 40 Hz.

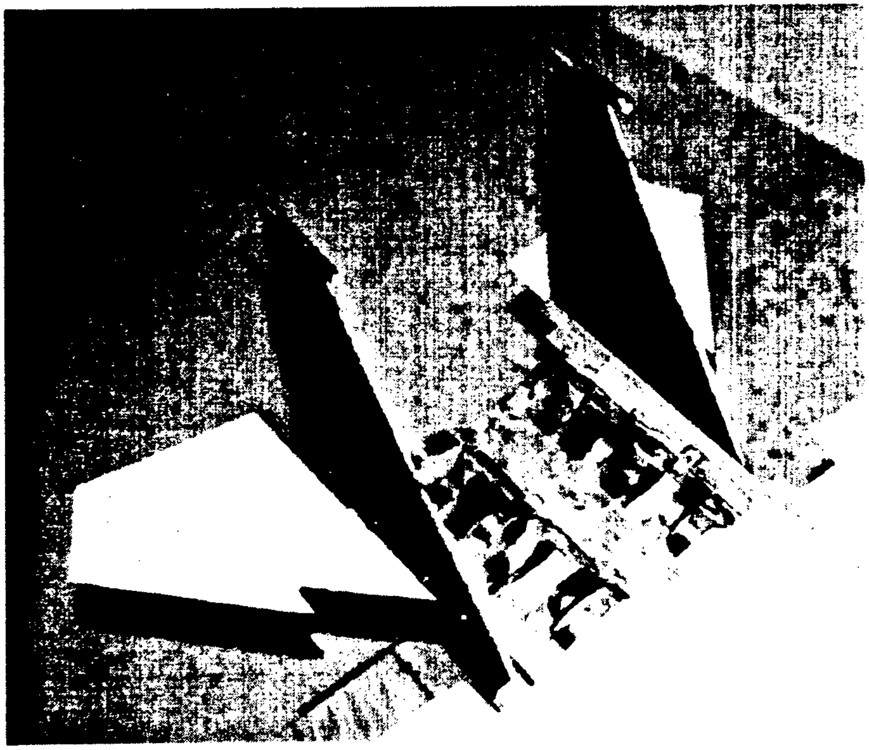

Figure 9.4. Froude Scale Model mounted on Rigid Body Fuselage

Each horizontal stabilator is made of a composite plate of six plies of fiberglass cloth embedded in epoxy matrix. Further, to obtain an improved simulation of the boundary conditions as well as a realistic transfer of energy from the horizontal to the vertical tails, a steel circular rod is embedded into the composite to represent the main spar of the horizontal tail. It will also provide the attachment point to the vertical tail substructure. Finally, the boom assembly is made of aluminum channels, thicker than the one of the 1 to 1 frequency matched model, and the engine fixtures are made of the same copper rings.

IX.4. Final Assembly

When all the different parts of the scaled model were designed and built, the 1/16-scaled model of the F-15 was assembled together. The results of this assembly are shown on figures 9.5 and 9.6.

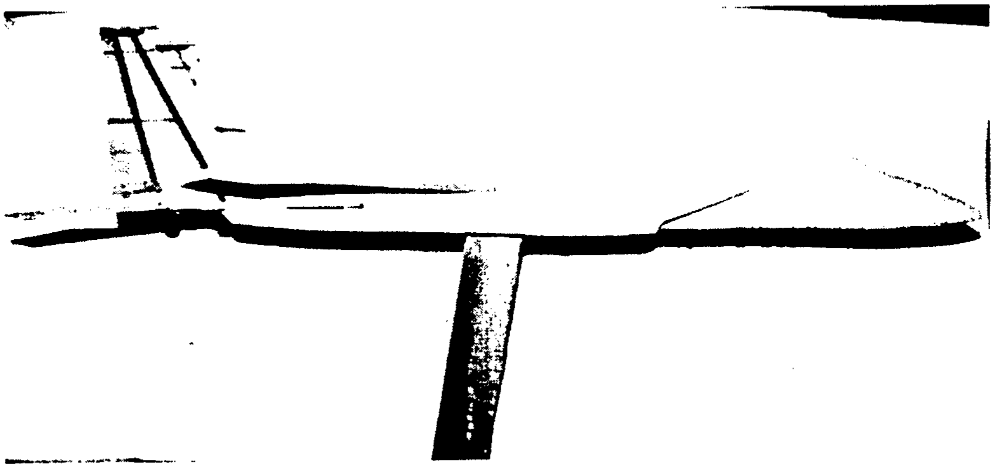

Figure 9.5. Side View of Assembled Model at 0° AOA.

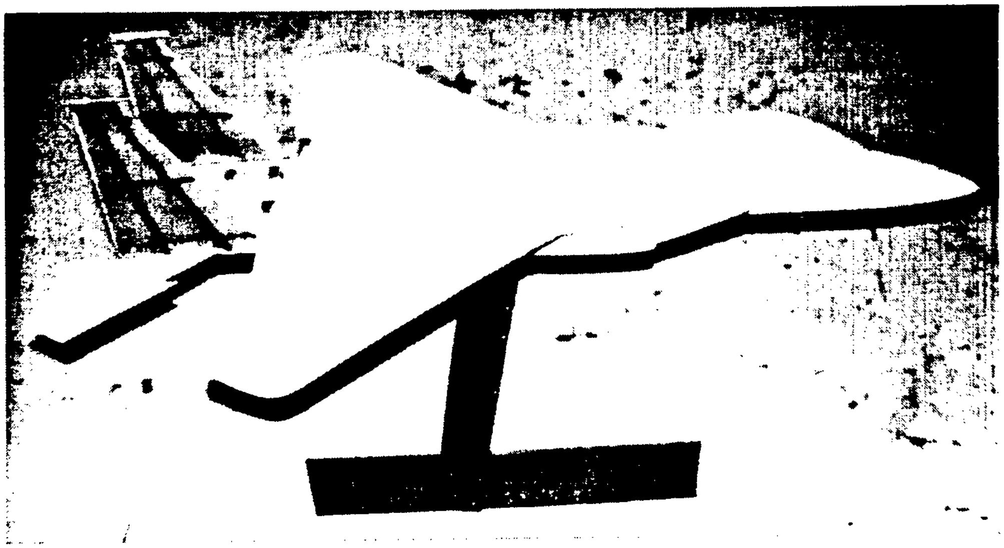

Figure 9.6. 1/16 Scale Model and Wind Tunnel Stinger

IX.5. Structural Integrity Test

Prior to testing in the wind tunnel, the structural integrity of the model has to be established to prevent break-up of the model during testing. This test will be performed by placing the model on the top of a car. Then, driving the car up to the wind tunnel test speeds will insure that the model is strong enough to endure the airloads that will be created in the wind tunnel. The car mount has been designed as is illustrated in figure 9.7.

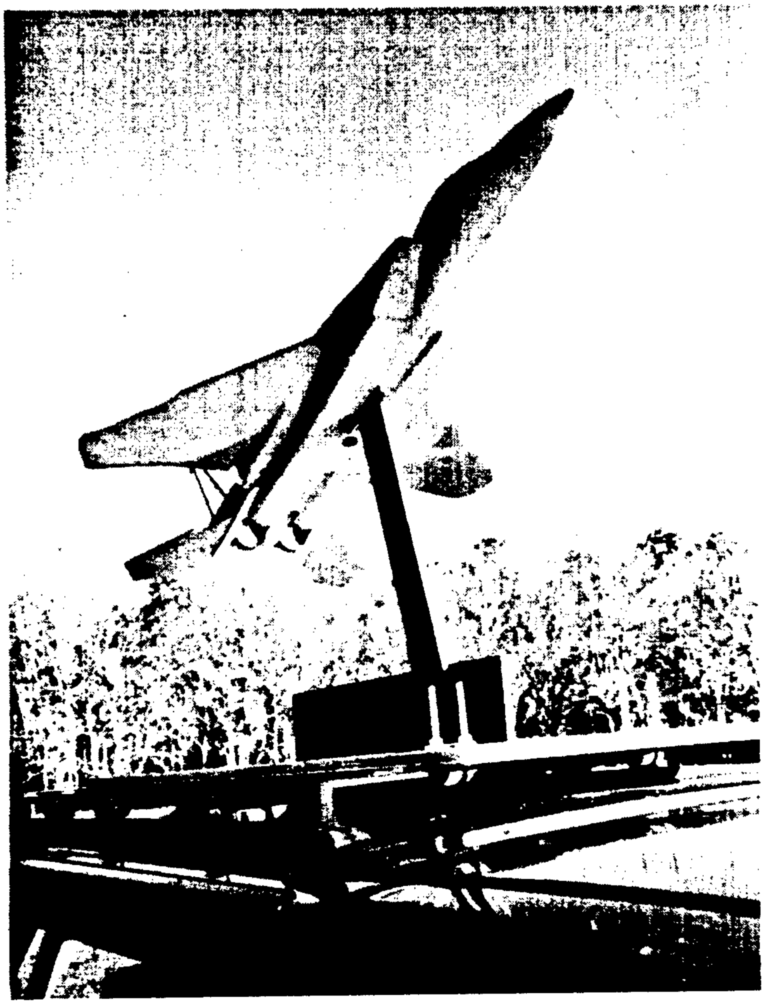

Figure 9.7. Structural Integrity Test Mount

X. WIND TUNNEL TESTS FOR CONTROL AUTHORITY STUDY

X.1. 1/16th Scale Model Installation In The Wind Tunnel And Experimental Setup

The scale model was mounted in the GTRI low speed wind tunnel as illustrated by Figures 10.1 and 10.2.

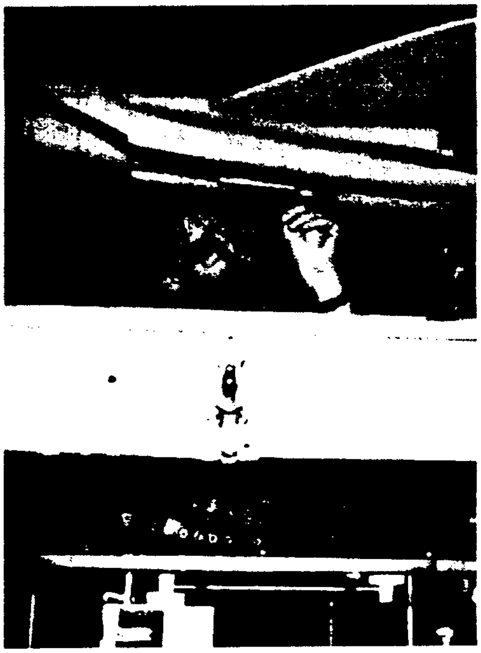

Figure 10.1. Scale Model Installation in the Wind Tunnel

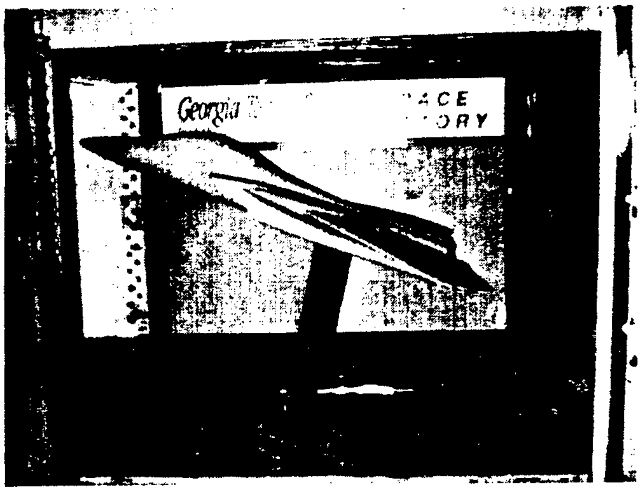

Figure 10.2. Tailless Scale Model at $\alpha = 22°$

The equipment used in the tests consisted of:

- A PC Computer and the dSPACE DSP based system used for real time control implementation, data acquisition, post processing and analysis.
- Two analog filters used for anti-aliasing purpose.
- A signal generator used as random signal generator for plant modeling.
- Two piezo drivers used to amplify the signal fed to the piezoceramic actuators.
- Three accelerometers and their associated signal conditioners used as sensors.
- An oscilloscope used for monitoring the different signals.
- Two pressure transducers and their associated signal conditioners to measure the pressure on the vertical tails.

The experimental setup is shown on figures 10.3 and 10.4.

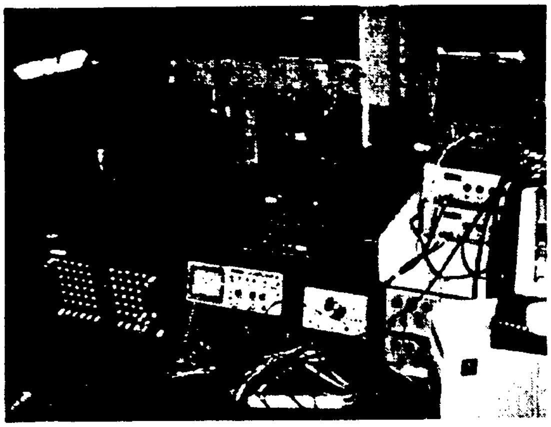

Figure 10.3. Experimental Setup

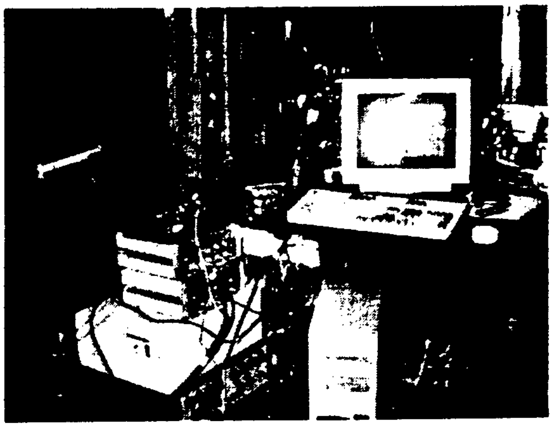

Figure 10.4. Experimental Setup (cont.)

X.2. Study Of The Buffet Effects On The Vertical Tails

This study was performed on the 1 to1 frequency ratio model. An accelerometer was positioned on the each vertical tail on the trailing edge just below the tip pod. These accelerometers were connected to analog to digital conversion ports of the DSP system for data acquisition.

X.2.a. Fixed Dynamic Pressure (q) Test.

For this first experiment, the value of the dynamic pressure that was chosen was q = 7 psf. This value of the dynamic pressure corresponds to an airspeed of 79.8 ft/s in the wind tunnel. (It is to be noted that this airspeed corresponds to a speed of about 750 knot for the full scale aircraft. Even though this speed would be supersonic for the full scale aircraft, it was far below the Mach number in the wind tunnel). The results of this test are illustrated by figure 10.5.

For angles of attack above 15°, there is a dramatic change in RMS of the vertical tail tip acceleration which is due to buffeting. From these data, it was decided to run the following tests at 22° angle of attack.

X.2.b. Fixed Angle of Attack (α) Test.

In the second experiment, the angle of attack at which the 1/16th scale model is mounted is fixed. As stated previously, the value of the angle of attack that was chosen was $\alpha = 22°$. The first data point was obtained with the wind tunnel motor on and the clutch not engaged to obtain the q = 0 psf condition. Then data were taken by increasing the wind tunnel dynamic pressure by increments of 0.5 psf from 4 psf up to 8 psf. The results of this test are illustrated in figure 10.6.

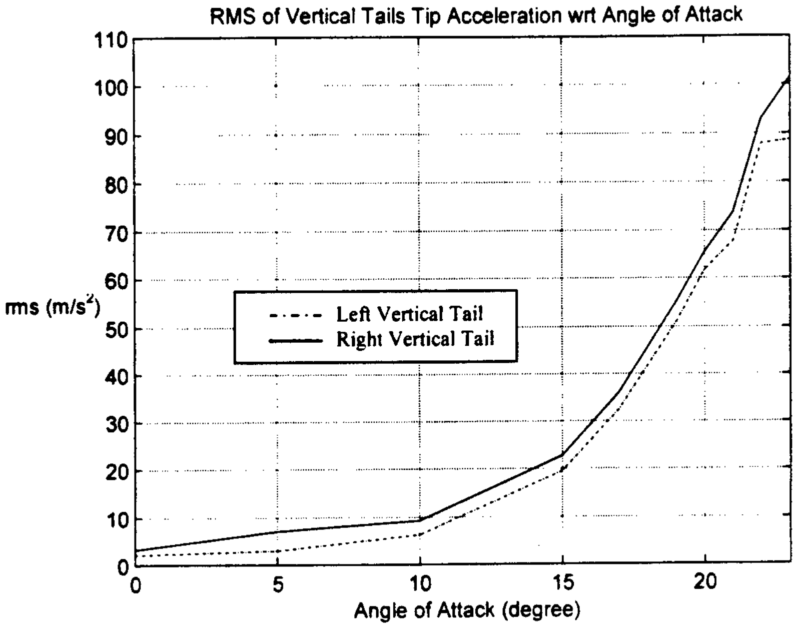

Figure 10.5. RMS of Vertical Tail Tip Acceleration for Increasing Angle of Attack at q = 7 psf.

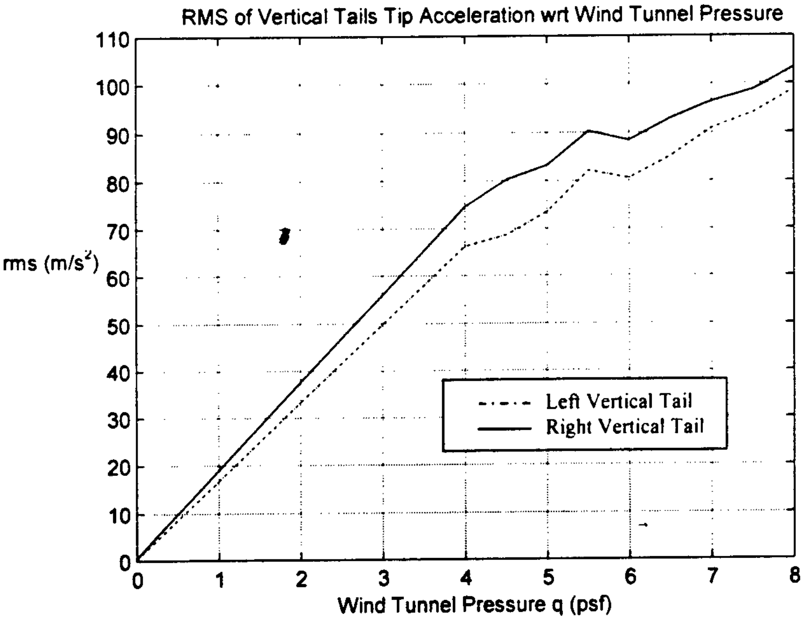

Figure 10.6. RMS of Vertical Tail Tip Acceleration for Increasing Dynamic Pressure at α = 22°.

From these data, it was chosen that future experiments will be conducted at 7 psf which also was the speed at which the first fixed dynamic pressure test was run.

X.2.c. Identification of the modes excited by the buffet flow.

This experiment was performed with the wind tunnel dynamic pressure set at q = 7 psf. The scale model was mounted at an angle of attack α = 22°. The accelerometer attached to the left vertical tail was fed to channel 1 and the one attached to the right vertical tail was fed to channel 2. The auto-power spectrums shown in figure 10.7 illustrate that frequencies between 25 and 90 Hz are dominant. These correspond to the first torsion mode, the second bending mode and the second torsion mode. The first bending mode has a natural frequency below the range of dominant frequencies. This mode will also be considered in the active vibration control experiment.

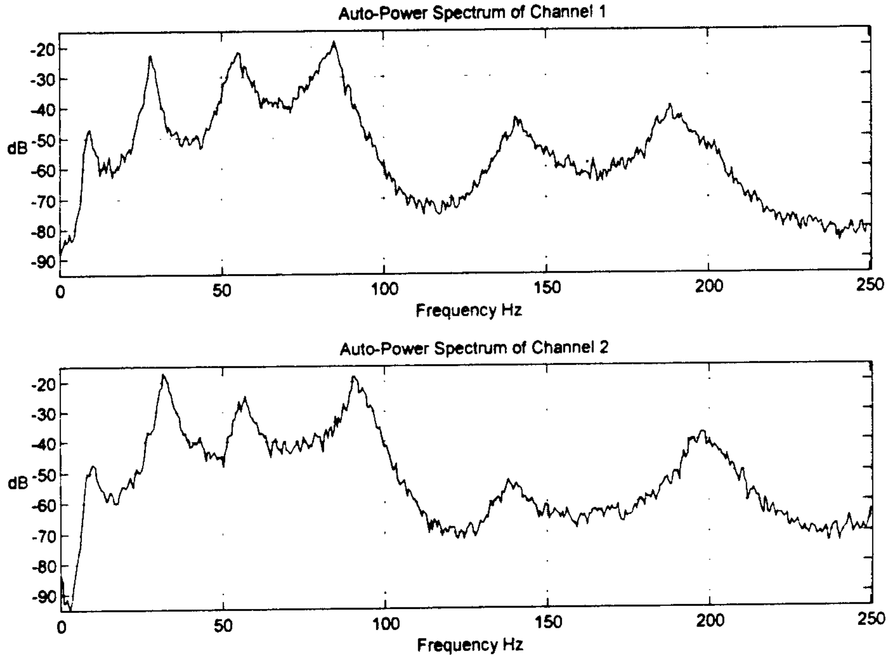

Figure 10.7. Auto-Power Spectrums of the Left Vertical Tail (Channel 1) and Right Vertical Tail (Channel 2) at q = 7 psf and α = 22°

X.3. Instrumentation for Estimating the Control Authority Needed.

Following the results of the test described in section X.2.b, we instrumented the 1 to 1 frequency ratio model with piezoceramic wafer actuators. These actuators were Morgan Matroc PZT-5H plates 1.9” in length, 0.85” in width and with a thickness of 0.02”. On each vertical tail, three pairs of those piezo wafers were bonded. Each pair was bonded such that it would produce pure bending moments along its edges. Two pairs were mounted at the root of the tails, parallel to the elastic axis, to control the bending modes. The third pair was mounted above the two bending actuation pairs at an angle of about 35° with respect to the elastic axis to control the torsion modes. Finally, some small lead masses were added inside the tip pods to obtain the desired natural frequencies that were altered by adding the piezoceramic actuators. The configuration of these actuators is illustrated by figures 10.8 and 10.9.

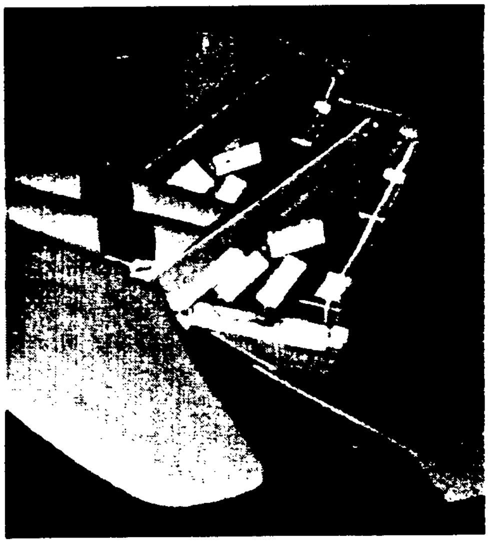

Figure 10.8. Instrumented Vertical Tails Mounted on the Scale Model

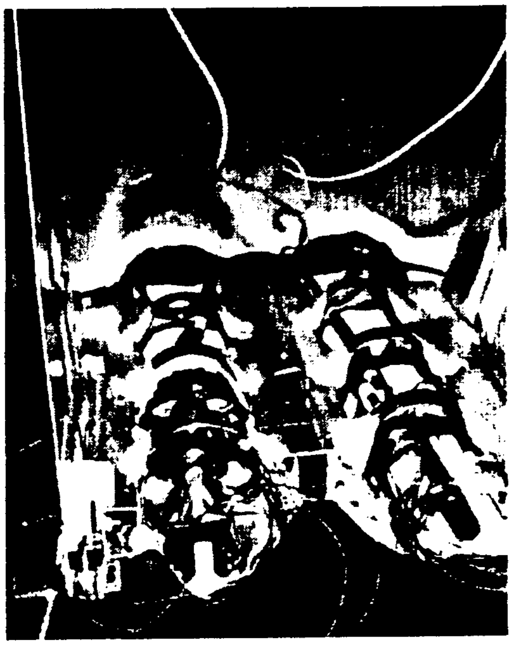

Figure 10.9. Wiring of the Instrumented Vertical Tails

X.4. Experimental Investigation of the Control Authority Needed to Alleviate the Buffet Induced Vibrations.

The first task of this investigation was to determine the flow characteristic and the response of the vertical tails of the instrumented model. We placed the two pressure transducers on the outboard trailing edge tips of the two vertical tails while the accelerometers were located on the inboard of the vertical tails. Then, the model was mounted at an angle of attack of $\alpha = 22°$. Simultaneously, the wind tunnel was set to run at $q = 7$ psf. The auto-power spectrums of pressures and accelerations are presented in figures 10.10 and 10.11.

Then, it was decided to actuate the left vertical tail only to assess the control authority needed to alleviate the vibrations induced by the buffet flow in the first four modes of that vertical tail. The first and fourth modes would be controlled using the actuators at the root while the second and third modes were controlled using the upper wafer pair.

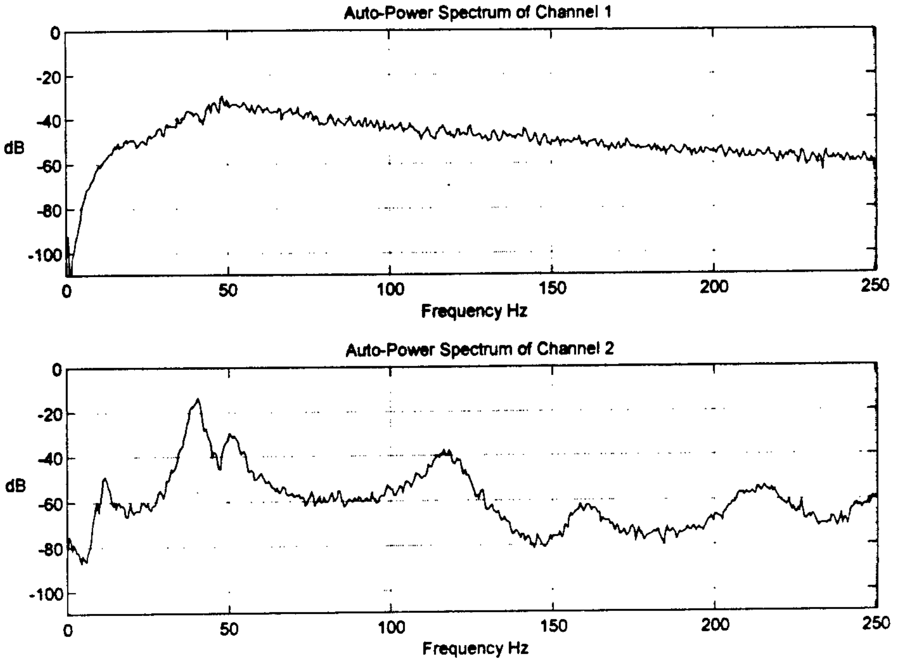

Figure 10.10. Auto-Power Spectrums of the Pressure (Channel 1) and Acceleration (Channel 2) of the Left Instrumented Vertical Tail

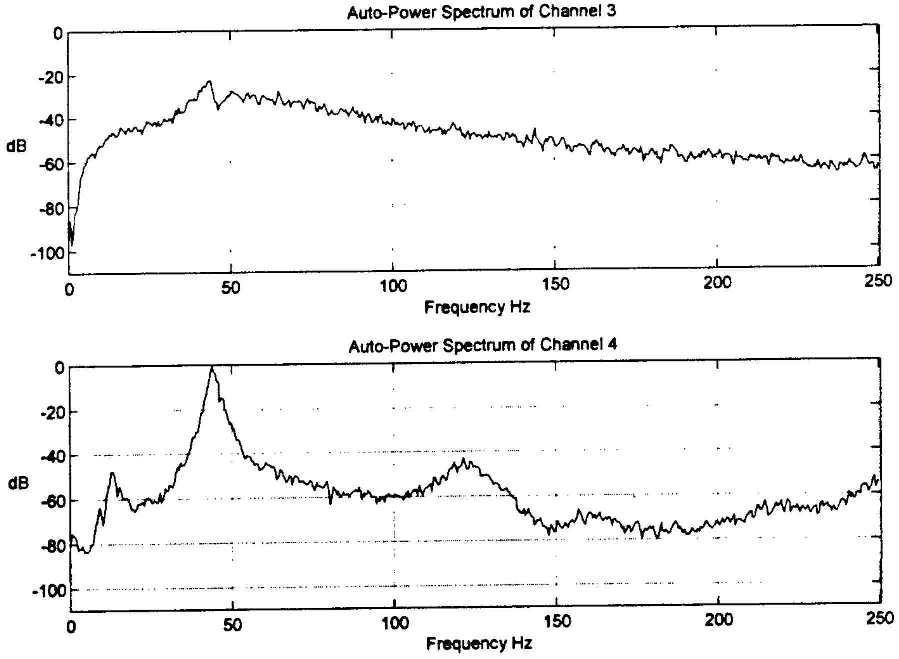

Figure 10.11. Auto-Power Spectrums of the Pressure (Channel 3) and Acceleration (Channel 4) of the Right Instrumented Vertical Tail

First, the transfer function between these lower wafers and the accelerometer mounted on the inboard trailing edge tip of the vertical tail was determined. Then, a controller was designed with two compensators in parallel. Each compensator follows the theory of acceleration feedback control with a crossover point based design. Once this control was designed, it was implemented with no airspeed.

Then, a second transfer function was obtained by vibrating the vertical tail using the upper actuator pair while controlling the first and fourth modes with the lower wafers. This transfer function was taken between the upper piezoceramic actuators and the accelerometer mounted on the inboard trailing edge tip of the vertical tail. Also using acceleration feedback control with cross-over condition, a controller was designed to damp the vibrations of the second and third modes. Then, both controllers were implemented simultaneously without any airspeed.

These controllers were designed such that the amplitude of reduction in each mode would be about a factor of two. The result of the wind tunnel validation of these controllers at a dynamic pressure of $q = 7$ psf is shown on figure 12. For this experiment, the model was mounted at a 22° angle of attack. All four controlled modes were reduced by a factor close to two. The maximum voltage at the input of the piezo driver was reached more than once during the experiment.

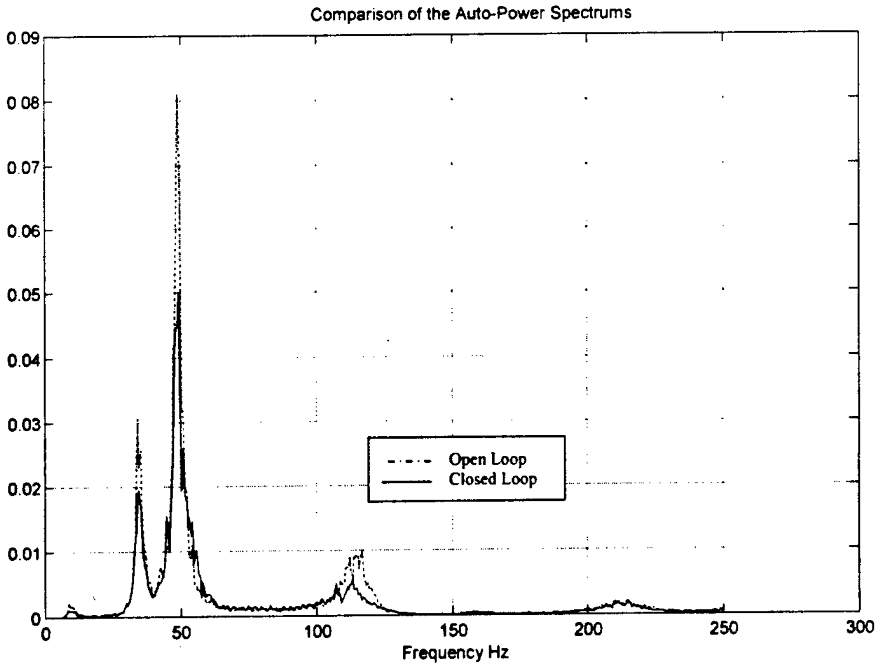

Figure 10.12. Comparison of Open Loop and Closed Loop
Auto Power Spectrum of the Acceleration of the Tip of the Left Vertical Tail

XI. WIND TUNNEL TESTS FOR ACTIVE TAIL BUFFET ALLEVIATION

XI.1. Design And Building of Final Aeroelastic Scaled Model

The control authority wind tunnel tests showed that there exists a characteristic frequency associated with the maximum buffet load. As illustrated in Figure 11.1, for our 1/16th scaled model at $\alpha=22°$ and $q_\infty=7$psf, this frequency is around 53 Hz. Based on a characteristic length given by the full-scale fin mean aerodynamic chord (81 inches) scaled to 1/16th and a free stream velocity of 23.75 m/s (equivalent to a dynamic pressure of 7 psf at 1000 ft altitude) , the reduced frequency associated with that maximum buffet load is 0.29.

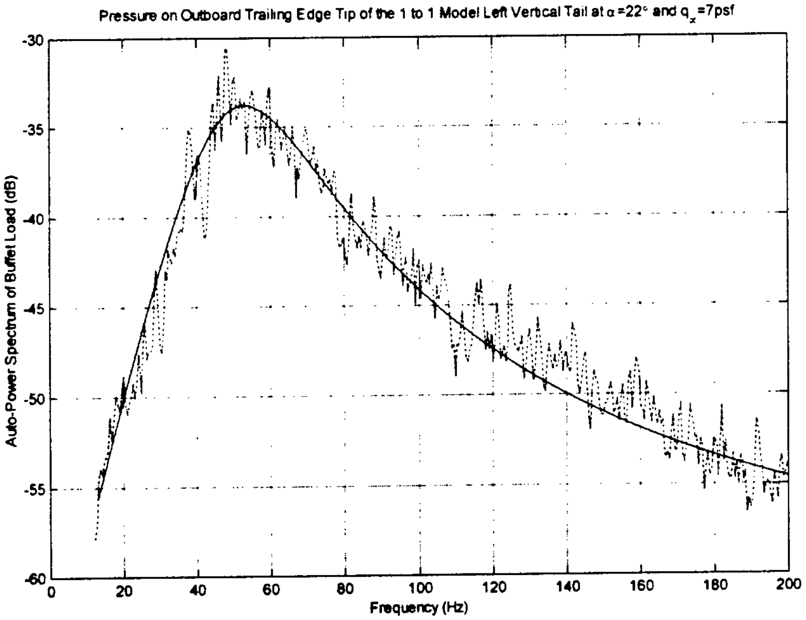

Figure 11.1. Auto-Power Spectrum of the Buffet Load on the Outboard Trailing Edge Tip of the 1 to 1 Scale Model Left Vertical Tail at $\alpha=22°$ and $q_\infty=7$psf.

The result of the MacAir experiments reported by Triplett (Ref. X.1) on a 13% scaled model shows a frequency associated with the maximum buffet load around 30 Hz at a free stream dynamic pressure of 12 psf. By scaling the full-scale fin mean aerodynamic chord and using a free stream velocity of 30.94 m/s (equivalent to a free stream dynamic pressure of 7 psf at 600 ft altitude), we obtain a reduced frequency associated with the maximum buffet load of about 0.26.

Furthermore, the results of some earlier Georgia Institute of Technology tests reported by Komerath et al. (Ref. X.2) indicated a frequency associated with the maximum buffet load of about 150 Hz for a 1/32th scale model at a free stream velocity of 30.48 m/s and of about 13 Hz for a 1/7th scale model at a free stream velocity of 12.19 m/s. By scaling the full-scale fin mean aerodynamic chord, the reduced frequency associated with the maximum buffet load for both of the experiments is about 0.31.

Since the reduced frequencies associated with the maximum buffet load agree within a few percent for all the experiments, we determined that it was very important for the active tail buffet alleviation tests to scale the model such that the reduced frequency is conserved. It is also important to note that these reduced frequencies would mean that the frequency associated with the maximum buffet load for a full-scale aircraft flying at 20,000 ft at Mach 0.6 would be around 26 Hz. This frequency does not coincide with any natural frequency of the full-scale empennage. In fact, it is located between the first bending mode around 10 Hz and the first torsion mode around 37 Hz.

The Georgia Tech Research Institute low speed wind tunnel performs optimally with our 1/16th scaled model between free stream dynamic pressures of 5 and 13 psf. To operate in this optimal range, the frequencies of the model should be between 2 and 2.5 time larger than the full-scale, which would be equivalent to running the wind tunnel with a free stream dynamic pressures in the range of 7 and 11 psf. To operate in the middle of the optimal range for the wind tunnel, the scale model of the empennage was designed to have natural frequencies 2.25 times larger than the full-scale tail subassembly. This model would then operate at a free stream dynamic pressure of 9 psf to conserve the reduced frequencies of the flow and structure. This dynamic pressure is equivalent to a free stream velocity of 26.9 m/s that translates to a free stream velocity of 191.5 m/s for the full-scale aircraft or about Mach 0.6 at 20,000 ft.

Using a finite element model with specified span-wise and chord-wise dimensions, corresponding to 1/16th of the full-scale vertical tails, we iterated over the thickness dimensions to obtain natural frequencies at a ratio of 2.25 to 1 with respect to the full-scale aircraft. The resulting scaled model of the vertical tails was built from a wet lay-up of Bondo plain weave fiberglass fabric and Bondo epoxy resin. Each vertical tail has 8 layers of fiberglass at the root and 5 layers at the tip. In addition some carbon fiber strips were added to represent the two main spars of the vertical tails. Finally, brass tubes of appropriate diameters were bonded to the tip to simulate the tip pods. Two similar sets of vertical tails were built. The vertical tails set one was constructed for pressure measurements and is illustrated in Figure 11.2. The second set of vertical tails was built for control experiments.

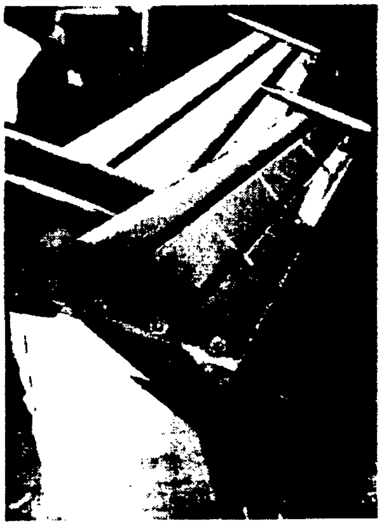

Figure 11.2. The first set of vertical tails for pressure measurements.

XI.2. Wind Tunnel Validation of the New Scaled Model

The first task of the wind tunnel tests was to validate our new scaled model. For this task, the model was outfitted with the first set of vertical tails. First, buffet load and response measurements were taken. Then a flow visualization experiment involving tufts attached to the model was performed.

XI.2.a Buffet Load and Dynamic Response Measurements

To perform the dynamic response measurements, an accelerometer was attached on the inboard trailing edge tip of the vertical tail. Simultaneously, the load measurements were obtained from a pressure transducer, a microphone, mounted on the outboard trailing edge tip of the vertical tail. The wind tunnel model of the aircraft assembly was set at an angle of attack of 20 degrees. During this experiment, five different free stream velocities were investigated. These velocities were ranging from 21 m/s to 33 m/s every 3 m/s. The results of these measurements are shown in Figures 11.3 and 11.4.

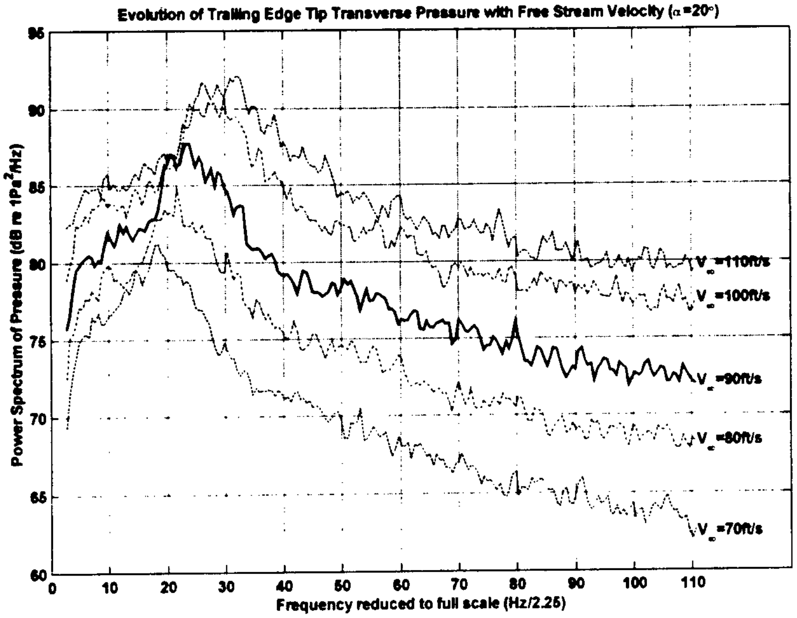

Figure 11.3. Evolution of Auto-Power Spectrum of the Outboard Trailing Edge Tip Pressure at α=20° for Free Steam Velocities ranging from 21 to 33 m/s.

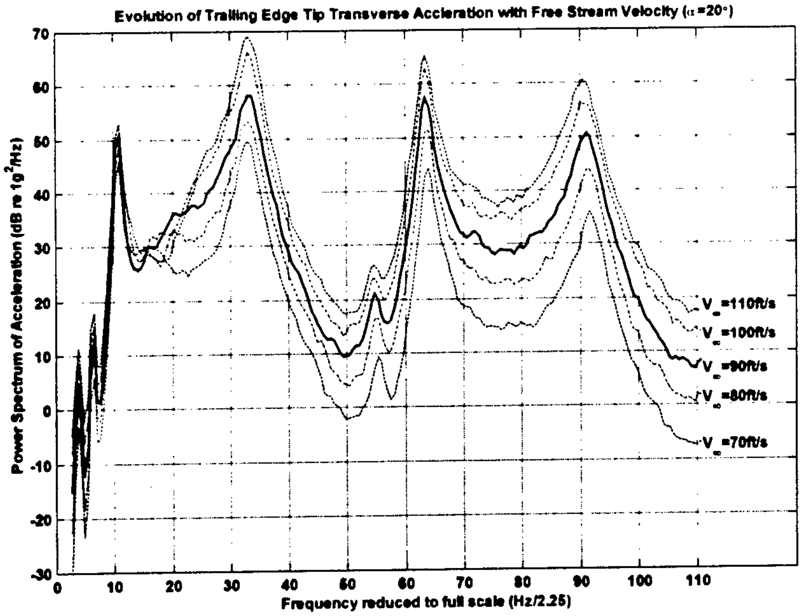

Figure 11.4. Evolution of the Auto-Power Spectrum of the Trailing Edge Tip Acceleration at α=20° for Free Steam Velocities ranging from 21 to 33 m/s.

As is illustrated in Figure 11.3, the frequency associated with the maximum buffet load evolves linearly with free stream velocity. This result confirms that the reduced frequency associated with the maximum buffet load remains constant. Furthermore, for the free stream velocity of 90 ft/s, which is about 27.4 m/s, the frequency scaled to the full-scale aircraft, associated with the maximum buffet load, is about 24 Hz. This frequency is very close to the frequency predicted in Section 1 of 26 Hz for a free stream velocity of 26.9 m/s.

As seen in Figure 11.4, while the overall pressure magnitude increases with free stream velocity, the response at the first bending mode of the vertical tail, around 10 Hz, changes very little. At the same time, the response at the second torsion mode, around 91 Hz, increases very rapidly with rising free stream velocity. The behaviors at the other modes are in between these two extremes. This phenomenon is due to the fact that the pressure peak increases in magnitude and moves toward higher frequencies as free stream velocity increases.

XI.2.b Flow Visualization for Sensor Location

For this part of the experiment, a series of tufts were attached to the model. The first series was divided into five rows of light and short tufts on the left wing to observe the state of the flow on that wing. Three long tufts were mounted along the left side of the fuselage, one above the engine inlet, one slightly aft of the leading edge of wing fuselage interface and one on the engine outlet in front of the vertical tail root. Further, three medium length tufts were attached to the bottom trailing edge of the wing. Finally, three pairs of tufts were mounted at the leading edge of the left vertical tail.

The model was mounted at an angle of attack of 20 degrees and the wind tunnel free stream dynamic pressure was set at 9 psf. The results are illustrated in Figure 11.5. The tufts on the wing show that the flow is detached from the leading edge to about two third of the chord as well as on the outboard third of the span. The tuft located above the engine inlet shows a strong vortex. The second long tuft shows that the vortex is detached from the fuselage and that a very strong current flows outboard from the fuselage. The third long tuft originating from the root of the engine outlet shows that the flow goes outboard of the vertical tail and present indication of vortex along the fin by circular movements. This result is confirmed by the three tufts on the vertical tail, which also have circular motion along the chord of the fin.

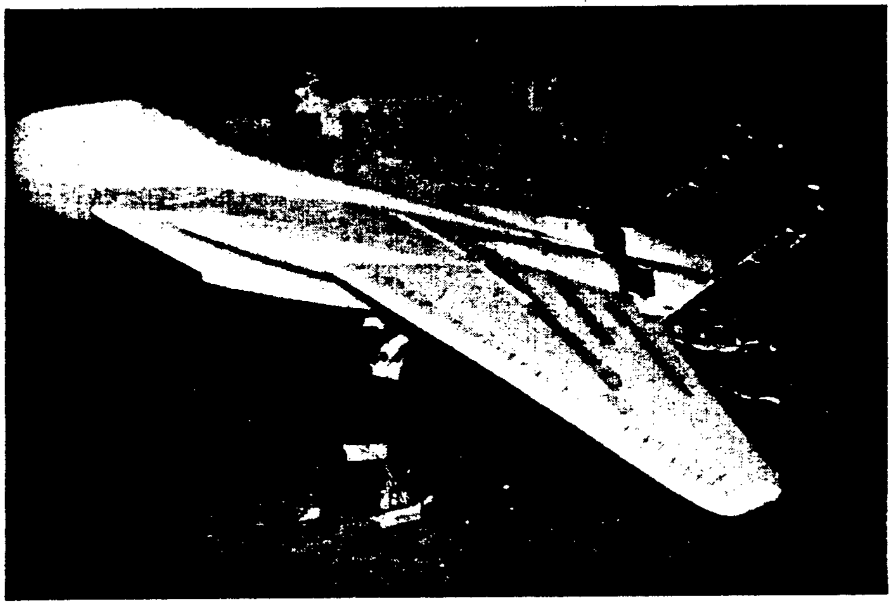

Figure 11.5. Flow Visualization Experiment at $\alpha=20°$ and $q_\infty=9psf$.

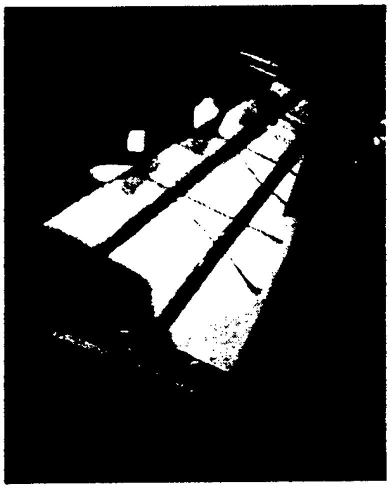

Figure 11.6. Tufts on both Sides of the Left Vertical Tail

Figure 11.6 illustrates the fact that the angles at which the tufts align are about the same on each side but varies by about 17 degrees from one side to the other. Since the outboard tufts are lower than the inboard tufts, this is an indication that a counter-clockwise, seen from the rear, vortex immerses the left vertical tail.

XI.3. Control Sensor Placement.

For most control experiments, the location of the sensor is dictated by the fact that all modes of interest must be observable by the sensor. Since the vertical tail behaves as a cantilever tapered plate and since the sensor that is used for acceleration feedback control is an accelerometer, the optimum locations are either on the leading edge or trailing edge tip of the vertical tail. From the flow visualization experiment, we determined that the core of the vortex is outboard of the vertical tail. As a result, to disturb the flow as little as possible, the sensor was located on the inboard side of the vertical tail. For similar reasons, it is also more desirable to locate the sensor on the trailing edge of the tail.

Since this was the location initially retained to validate the scaled model, the response of the control sensor is illustrated in Figure 11.4. This figure demonstrates that all four principal modes, below 100 Hz, are observable. These modes are the first bending mode at 10 Hz, at 33 Hz, at 63 Hz and at 91 Hz.

XI.4. Wind Tunnel Buffet Response Study

The goal of this phase was to determine at which attitude the worse disturbances are encountered. Since we assume linearity of the structure, the dynamic response of the vertical tail was measured instead of the pressure. This set of experiments is divided into two parts. First, a fine survey was conducted for angles of attack ranging from 0 to 23 degrees. Then, a second survey was conducted for different angles of attack and free stream dynamic pressures in the neighborhood of the worse buffet conditions.

XI.4.a Angle of Attack Study

The first test was performed to determine which was the angle of attack at which the worse disturbances are encountered. As discussed in Section XI.1, the experiment was run at a free stream dynamic pressure of 9 psf. The results of this experiment are illustrated in Figure 11.7.

This experiment shows that the angle of attack that displays the maximum tip response is about 20 degrees. This agrees with the results reported by Komerath et al. (Ref. X.2) during their tests, however it does not agree exactly with Triplett (Ref. X.1) results that reported a worse case for an angle of attack of 22 degrees. The decrease in vibrations above 20 degrees is due to the fact that the flow on the wing is completely separated which destroys the coherence of the buffet vortices. It is also interesting to notice that the vibrations below 12 degrees increase slowly and almost linearly with respect to the angles of attack. However from 12 to 20 degrees the amplitude of vibrations is increased by a factor of 10 very rapidly. This is due to the buffet induced vortices increase in strength which immerse more and more of the vertical tail.

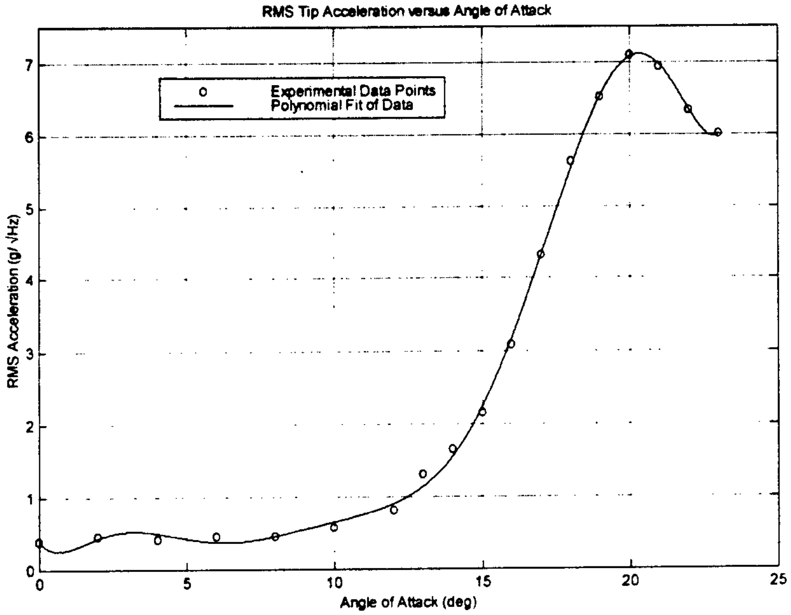

Figure 11.7. Root Mean Square of the Trailing Edge Tip Acceleration versus Angle of Attack at q_∞=9psf.

XI.4.b Angle of Attack and Free Stream Velocity Study

This test was performed to determine the behavior of the disturbance in the neighborhood of the worse attitude, 20 degrees angle of attack, at a free stream dynamic pressure of 9 psf. This experiment used acceleration data from the sensor to visualize the disturbance. The model was set at five different angles of attack, 14, 17, 20, 21 and 23 degrees. For each angle of attack, the wind tunnel was run at five different free stream dynamic pressures, 5, 7, 9, 11 and 13 psf, which correspond to the defined free stream velocity of 26.9 m/s with additional point in the +25% to –25% of operational free stream velocity range. From these experimental data, an envelope of the disturbance was extrapolated and is illustrated in figure 11.8.

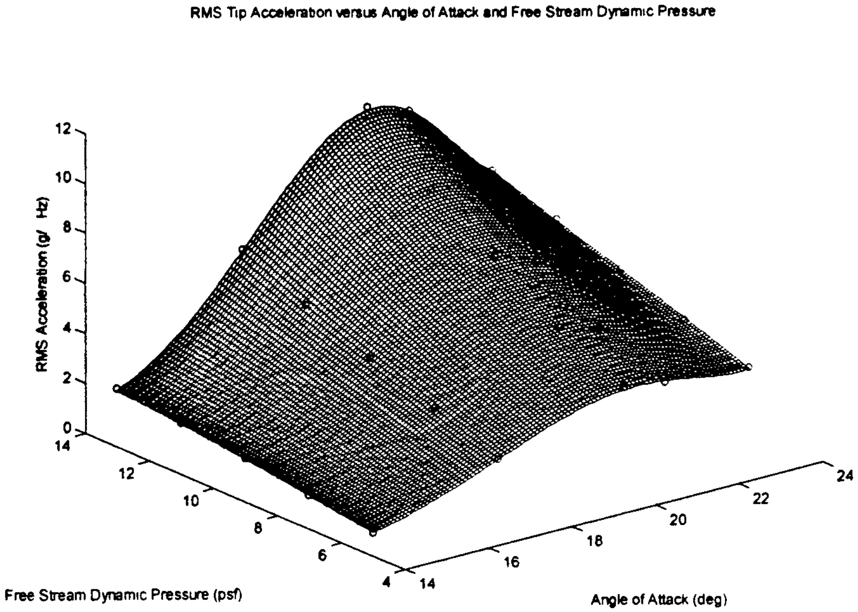

Figure 11.8. Envelope of Root Mean Square of the Trailing Edge Tip Acceleration versus Angle of Attack and Free Stream Dynamic Pressure (o: Experimental Data Points).

The results, illustrated in Figure 11.8, confirm that at all free stream velocities the maximum disturbance occurs at an angle of attack close to 20 degrees. Furthermore, the rate at which the disturbance increases is also maximum along the 20 degrees line. As a result, in active tail buffet alleviation studies, we study the effectiveness of the controller for different free stream velocities at 20 degrees angle of attack.

XI.5. Actuators Placement and Mounting

At this point, the left vertical tail of the second set of vertical tails that was made for control experiments was instrumented with two pairs of piezoceramic stack based actuators. The first pair of actuators was located to obtain large bending actuation authority. The best location was identified by using a PVDF film sensor and recording its response while the tail was excited with an impact hammer at the control sensor location as discussed in Section V. By reciprocity, wherever the largest response in the bending modes was observed, the largest bending actuator authority would be obtained. As a result, this first pair was placed at the root of the vertical tail along its mid-chord line. Similarly, the second pair of piezoceramic stack actuators was placed for torsion control.

Using the same method as for the bending control actuators, this pair of stack based actuators was bonded at 35degrees with respect to the mid-chord line above the first pair.

As illustrated in Figures 9.a and 9.b, during the wind tunnel experiments the stack based actuators were covered with masking tape both for safety purposes and to reduce the flow perturbation generated by those actuators.

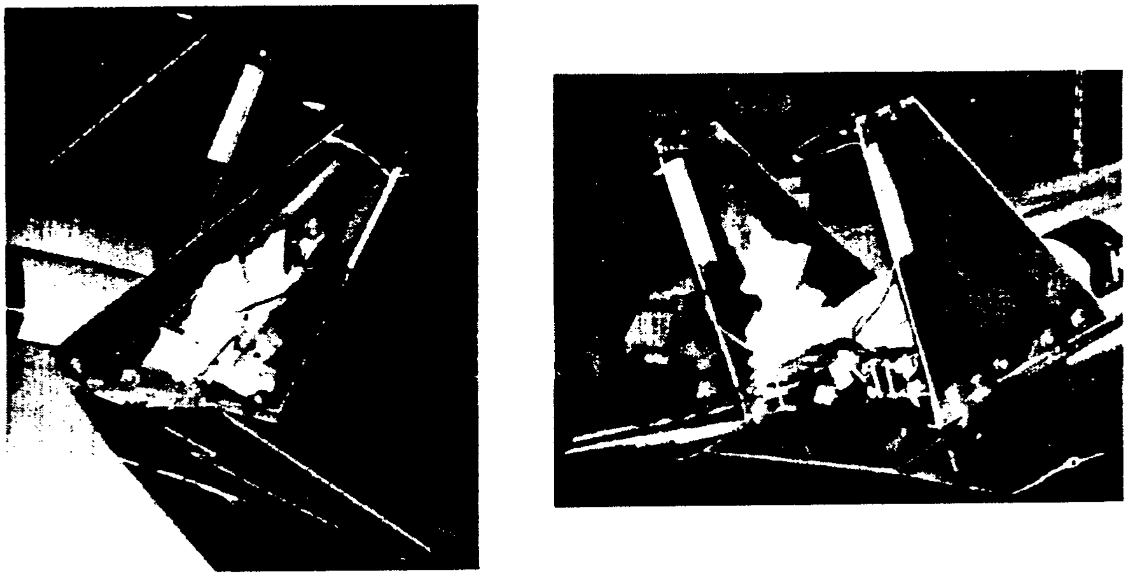

Figure 11.9. Outboard(a) and Inboard(b) Views of the Control Experiment Vertical Tails

XI.6. Control Plant Model and Control Parameters Extraction

The first task associated with designing a controller is to obtain a mathematical representation of the system to be controlled. This representation is usually referred to as a "plant". For acceleration feedback control, this plant model should be in the form of a transfer function matrix between the actuator arrays and the sensors. This is due to the fact that acceleration feedback control principally adds active damping to the structure.

For our purpose, we only consider that we have two actuator arrays and a single control sensor. To obtain the plant model, first an experimental transfer function is obtained between the input voltage to each actuator array and the control sensor response voltage. Then using a combination of system identification techniques such as single pole fitting and complex circle fitting around the poles, the parameters of each of the transfer functions are extracted. Finally, as is illustrated in Figures 10 and 11, the experimental transfer functions and the modeled transfer functions are displayed on top of each other.

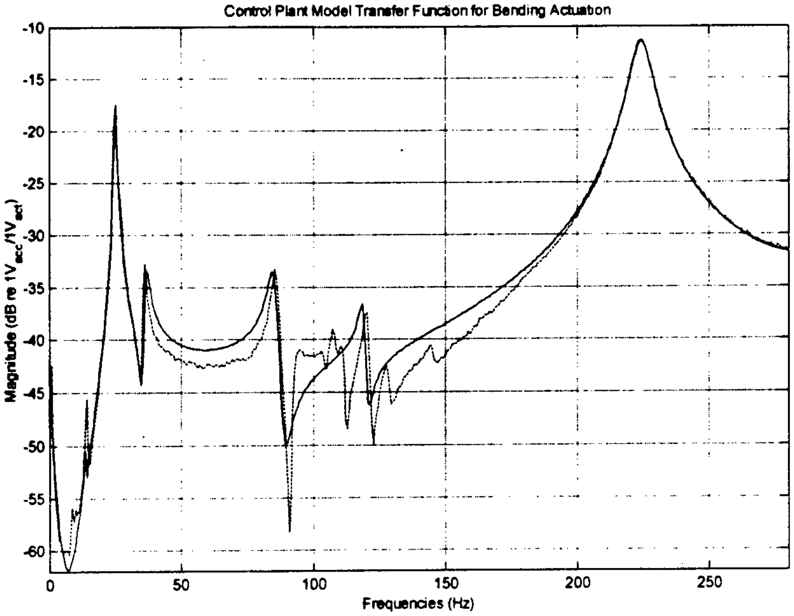

Figure 11.10. Experimental and Modeled Transfer Functions between the Control Accelerometer Response Voltage and the Input Voltage to the Bending Actuators.

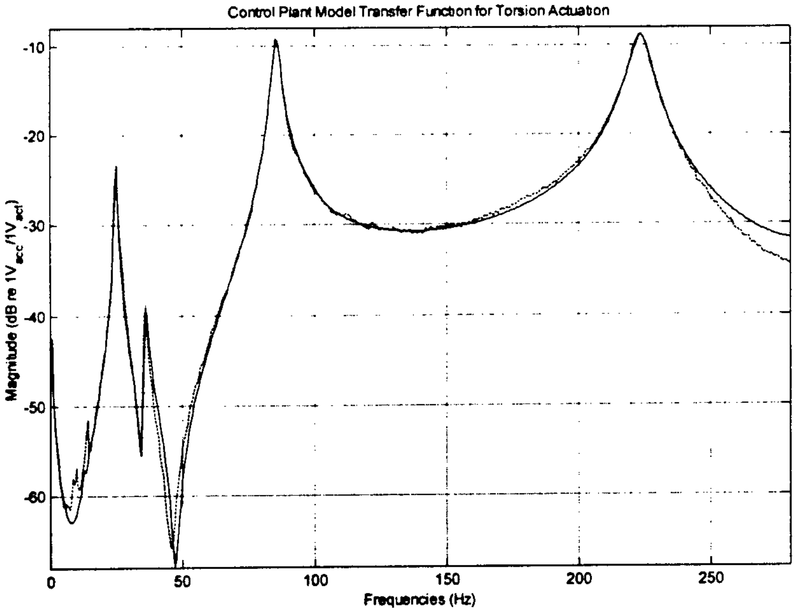

Figure 11.11. Experimental and Modeled Transfer Functions between the Control Accelerometer Response Voltage and the Input Voltage to the Torsion Actuators.

It is to be noted at this point that the addition of the two pairs of stack based actuators has almost suppressed the second bending mode passively. Hence, for the following control experiments, we will concentrate on suppressing the first bending mode with the bending array and the first and second torsion modes with the torsion array.

XI.7. Actuator Arrays Authority Assessment

In order to assess the authority of the controller, some response data from the wind tunnel needs to be acquired using the second set of vertical tails. The model was set at 20 degrees angle of attack and the wind tunnel was run at the operating dynamic pressure of 9 psf. The response of the control sensor was measured and the auto-power spectrum of the response computed. In parallel, the experimental transfer functions of the plant were converted to auto-power spectrums for a flat maximum input voltage of 7 V. The results of these two operations are displayed together as illustrated in Figure 11.12.

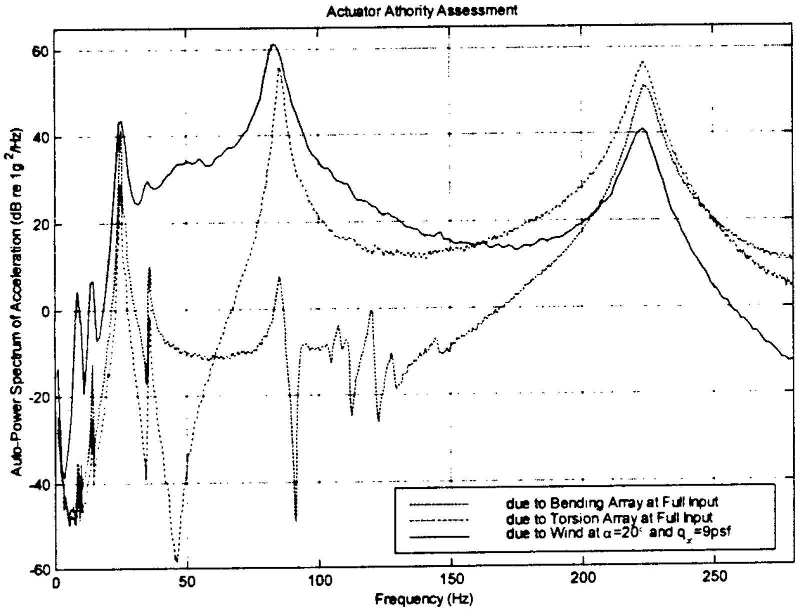

Figure 11.12. Actuator Arrays Authority Assessment Plots

Since the auto-power spectrums of the acceleration response of the control sensor due to the wind and due to the bending array are about the same, the bending array has enough control authority to suppress this particular mode. For the first torsion mode, the torsion array produces a slightly smaller response than the wind, however this differences is not large enough to require an extra actuator. Finally, for the second torsion mode, both of the actuator arrays produce a larger response than the wind hence there will not be any difficulty to suppress this mode using either of the actuator arrays. Since the torsion array has a larger authority on the second torsion mode, we will use these actuators to suppress this mode.

XI.8. Controller Design using Acceleration Feedback Control

Once the plant model has been developed and the actuator authority checked, the controllers themselves must be designed. For this experiment, the type of controller that was selected was acceleration feedback control (AFC). Furthermore, the type of design for AFC that was retained was the H_2 optimal design presented in Section VI.3.

For the control of the first bending mode, using the parameters extracted earlier for the bending array, a single degree of freedom acceleration feedback controller was designed. As discussed in Section VI.3, only one design parameter is necessary to obtain the controller. In this case this parameter was selected to be the amount of damping in the controller. In order to avoid clipping of the control signal, the damping of the controller was selected to be seven times larger than the damping of the first bending mode of the vertical tail. The transfer function of this controller is illustrated in Figure 11.13.

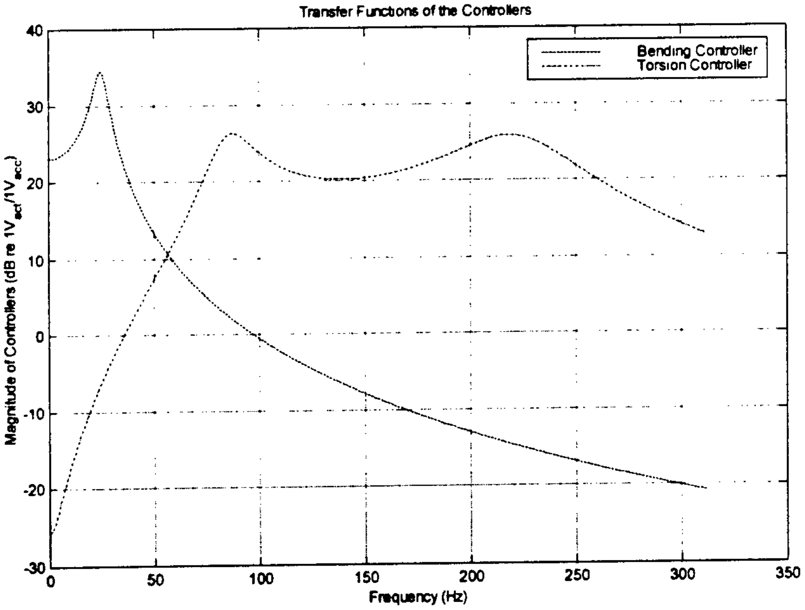

Figure 11.13. Magnitude of the Transfer Functions of the Controllers between the Voltage Input to the Actuators Piezo Driver and the Control Sensor Voltage

The second controller was designed for the active damping of the first and second torsion modes using the torsion array. In this case, two separate single degree of freedom controllers are designed, one for each mode, using the parameters extracted earlier for the torsion array. As for the control of the first bending mode, only one parameter is needed for each controller. Following the same argument as before, the damping of each compensator was chosen to be seven times larger than the damping of the associated mode. The transfer function of this controller is also illustrated in Figure 11.13.

Once the controllers are designed, their stability and effects on other modes are checked. This task is performed by plotting the root locus plot associated with each controller. The root locus plot of the bending controller is illustrated in Figure 11.14. From this figure, it is to be noted that none of the roots move toward the right hand plane and hence the controller is stable. Furthermore, the roots associated with the first and second torsion modes, which have imaginary part ±550 and ±1400 respectively, are left unchanged by the controller. From this fact, we are assured that the torsion controller will behave properly in the presence of the bending controller.

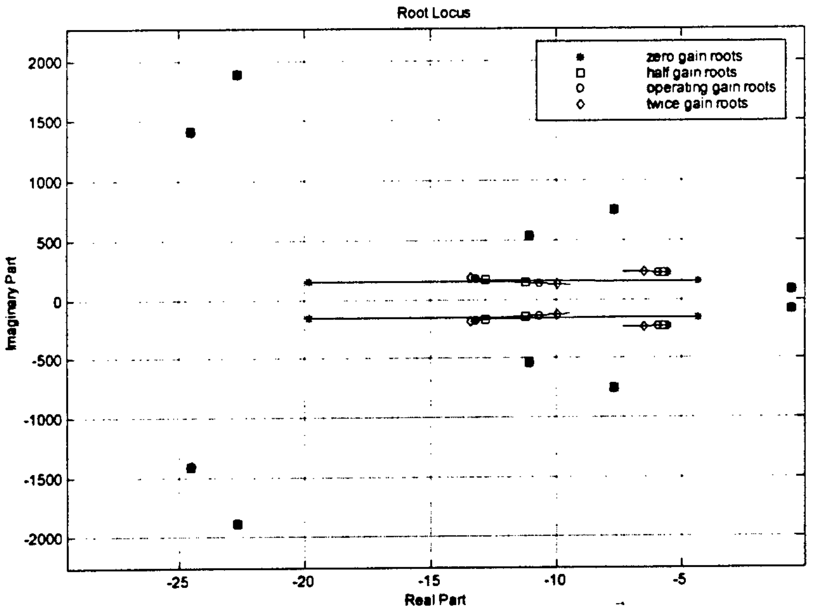

Figure 11.14. Root Locus Plot for the Bending Controller

Similarly, the root locus plot of the torsion controller is illustrated in Figure 11.15. First, the roots associated with the first bending mode, which have imaginary part ±200, is left unchanged by the controller. Hence the bending controller will behave properly in the presence of the torsion controller. Furthermore, even though certain roots seems to move toward the right hand plane for large values of the gain, at the operating conditions, no instabilities are noticed.

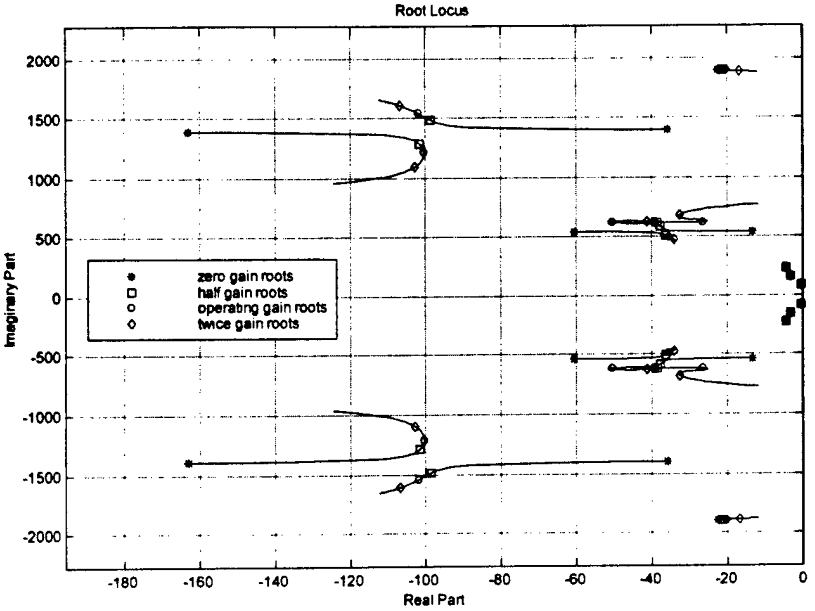

Figure 11.15. Root Locus Plot for the Torsion Controller

Since both root locus plots do not show any instability and each controller does not affect the parameters of the other controller, the controllers can be implemented simultaneously.

XI.9. Controller Implementation using a Digital Signal Processor

The first step of the implementation is the wiring of the experiment. As illustrated in Figure 11.16, the control accelerometer on the inboard trailing edge tip of the vertical tail is connected to a PCB signal conditioner. In turn, the output of the signal conditioner is connected to both an analog to digital (A/D) channel of the dSPACE system for control implementation and to another A/D channel through an anti-aliasing filter for data acquisition.

Four different digital to analog (D/A) channels are used to carry the control signals. Each channel is connected to an input channel of a piezo driver. The two piezo driver units are used to both set DC biases and amplify the control signals. Finally, each output of the piezo drivers is connected to a stack actuator.

The experimental setup for the active damping of the buffet induced vibrations is illustrated in Figure 11.17.

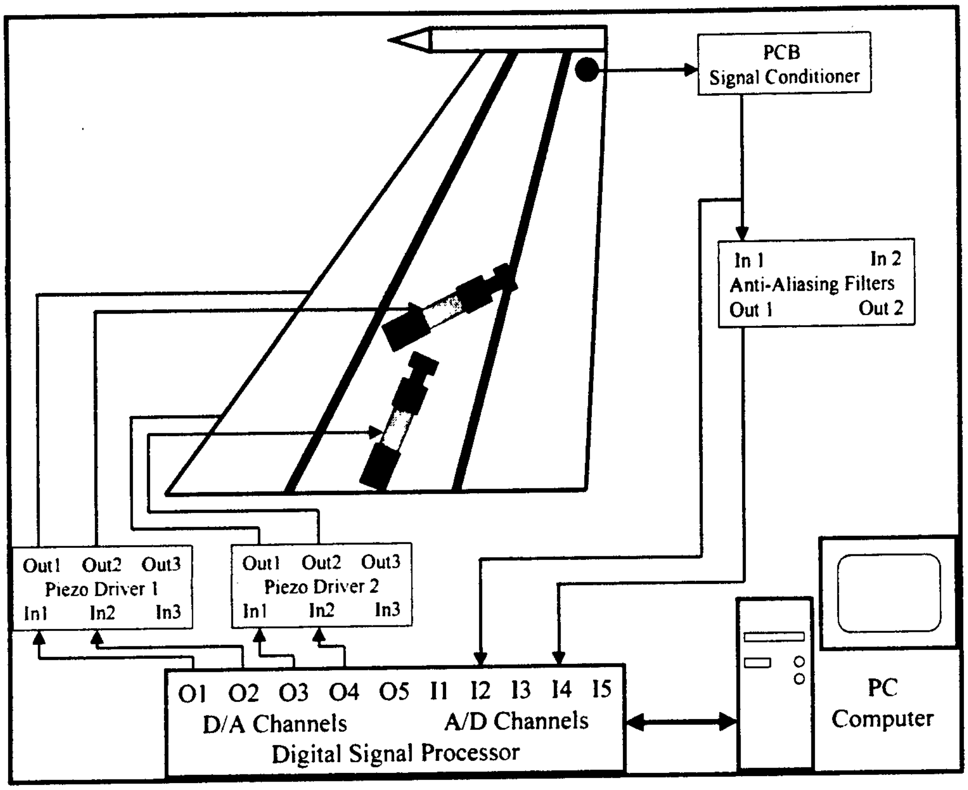
PCB
Signal Conditioner
In 1
In 2
Anti-Aliasing Filters
Out 1
Out 2
Out1
Out2
Out3
Piezo Driver 1
In1
In2
In3
Out1
Out2
Out3
Piezo Driver 2
In1
In2
In3
O1 O2 O3 O4 O5 I1 I2 I3 I4 I5
D/A Channels
A/D Channels
Digital Signal Processor
PC
Computer

Figure 11.16. Wiring for the Active Buffet Alleviation Experiment

The controllers are implemented on a dSPACE system. The system is made of five A/D converters, five D/A converters and two digital signal processors (DSP). The first DSP is dedicated to the process of the input and output channels, and then sends the data to the second DSP. The second DSP, which runs faster, is used for the implementation of the controllers.

The coding of the overall control experiment is done using block programming with the Matlab extension called Simulink. As an example, the controllers are entered in the Simulink file as transfer function blocks. The file is then converted to the DSP machine language and downloaded to the dSPACE system. Once the system starts, the controllers are effective.

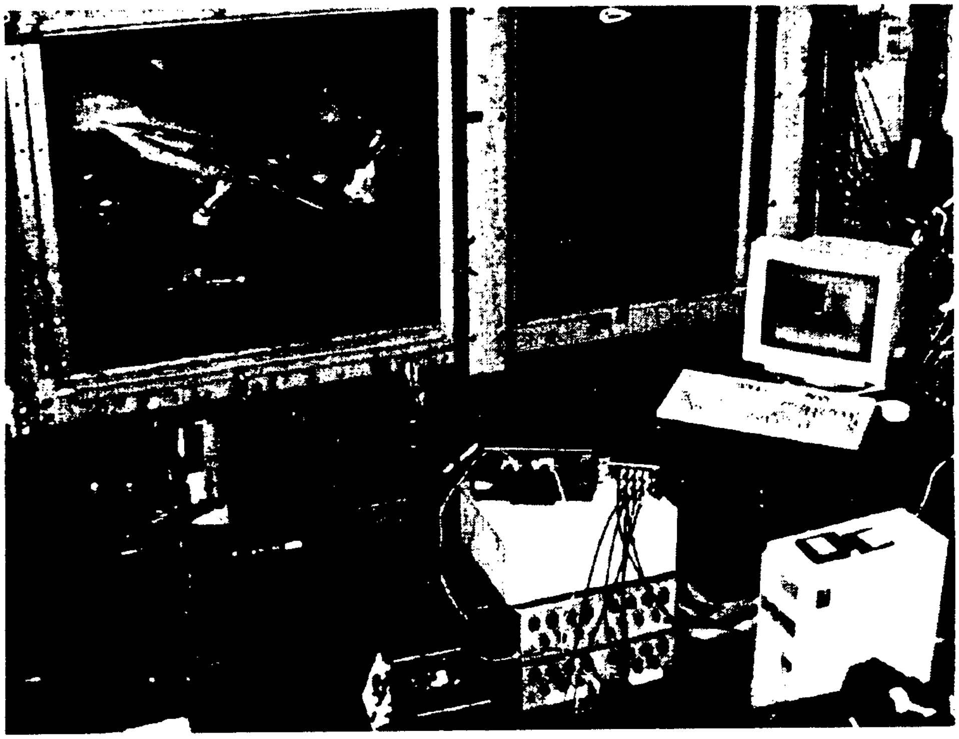

Figure 11.17. Experimental Setup for the Active Buffet Alleviation Experiment

XI.10. Active Buffet Alleviation Validation

To validate the controllers, three different experiments were carried out. First, a control experiment was run at the predetermined operating condition of 20 degrees angle of attack and 9 psf of free stream dynamic pressure. Then, for a free stream dynamic pressure of 9 psf, the angle of attack was varied from 0 to 23 degrees. Finally, four different angles of attack were selected and the free stream dynamic was varied from 5 to 13 psf.

XI.10.a Operating Condition Control Experiment

The conditions at which this experiment was conducted were dictated by the arguments discussed in Sections 1 and 4. The operating free stream dynamic pressure of 9 psf was set to reflect a full-scale aircraft flying at Mach 0.6 at an altitude of 20,000 ft. The angle of attack of 20 degrees was chosen to validate the controller at the worse buffet conditions for the given free stream velocity.

The auto-power spectrums of the uncontrolled and controlled trailing edge tip acceleration are illustrated in Figure 11.18. This figure 11.shows that each of the controlled frequency has its auto-power spectrum reduced by a factor of at least 5. Furthermore, in the case of the first bending mode and second torsion mode, the responses are suppressed to a level equivalent to the one that would be obtained in the absence of the modes. The reduction of the first torsion mode is somewhat less spectacular, however the amplitude of the mode is reduced by 80%.

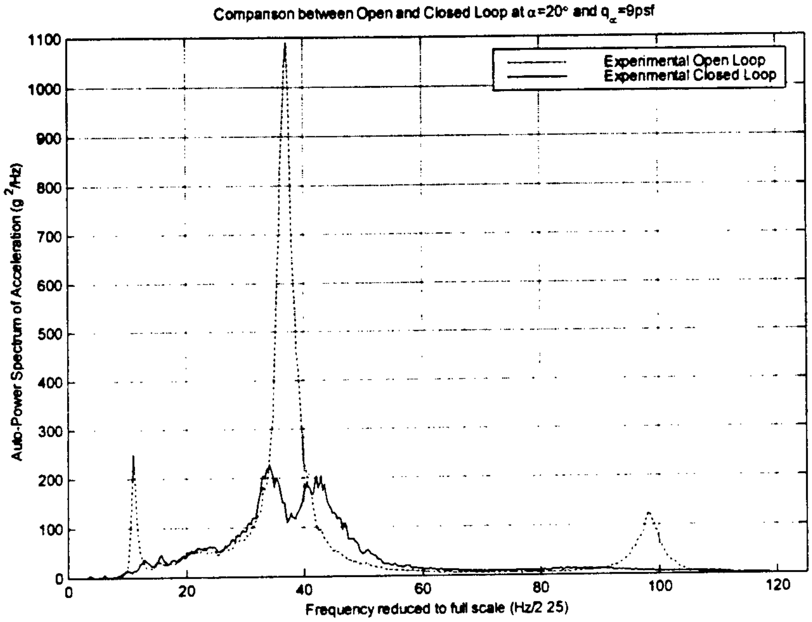

Figure 11.18. Comparison Between Open and Closed Loop Auto-Power Spectrum of Trailing Edge Tip Acceleration at α=20° and q_∞=9psf.

XI.10.b Angle of Attack Sweep Control Experiment

Once the controller has been validated at its operating point, its effectiveness must been check at different conditions. For this second experiment, the operating free stream dynamic pressure of 9 psf was kept. However, the angle of attack was varied from 0 to 23 degrees. For small angles of attack, the angle was changed by two degrees between every run. However, above 12 degrees, the sweep was made for every degree. The root mean squares of the trailing edge tip acceleration are illustrated in Figure 11.19.

This control experiment shows that the root mean square of the trailing edge tip acceleration is reduced by up to 30% below 15 degrees and by about 20% at 20 degrees. These differences are due to the much larger buffet disturbance pressure at the worse angle of attack. However, as is discussed previously, even with 20% reduction in RMS, the peaks associated with each mode are reduced by a factor of at least 5. Finally, this experiment shows that the controllers are effective on the whole range of angles of attack.

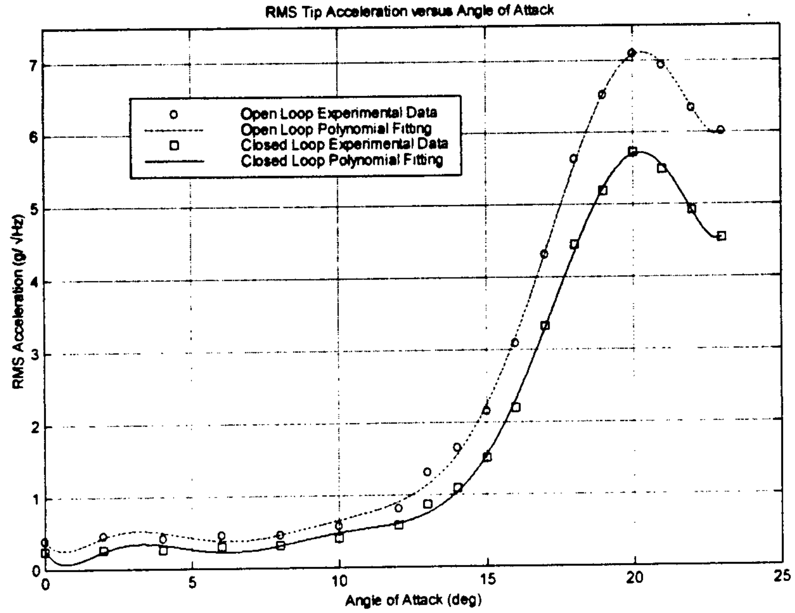

Figure 11.19. Uncontrolled and Controlled Root Mean Square of the Trailing Edge Tip Acceleration versus Angle of Attack at q_∞=9psf.

XI.10.c Free Stream Dynamic Pressure Sweep Control Experiment

Since the controller has been validated on the whole range of angles of attack for the operating free stream dynamic pressure of 9 psf, its effectiveness must be checked for different free stream velocities. For that purpose, different angles of attack were selected. 14, 17, 20 and 23 degrees angles of attack cover the different regimes that the scaled model encounters. For each angle of attack, the free stream dynamic pressure is varied from 5 to 13 psf. Uncontrolled and controlled data are recorded for every 2 psf. The root mean squares of the trailing edge tip acceleration are illustrated in Figure 11.20.

As before, the results show that as the disturbance increases the effectiveness of the controllers decrease. However, even at a free stream velocity 25% higher than the operating free stream velocity, the minimum RMS reduction is still 17%. These results prove that the controllers are stable and effective over the full buffet domain which means angles of attack ranging from 14 to 23 degrees and free stream velocity ranging from –25% to +25% of the full-scale equivalent of Mach 0.6 at 20,000 ft.

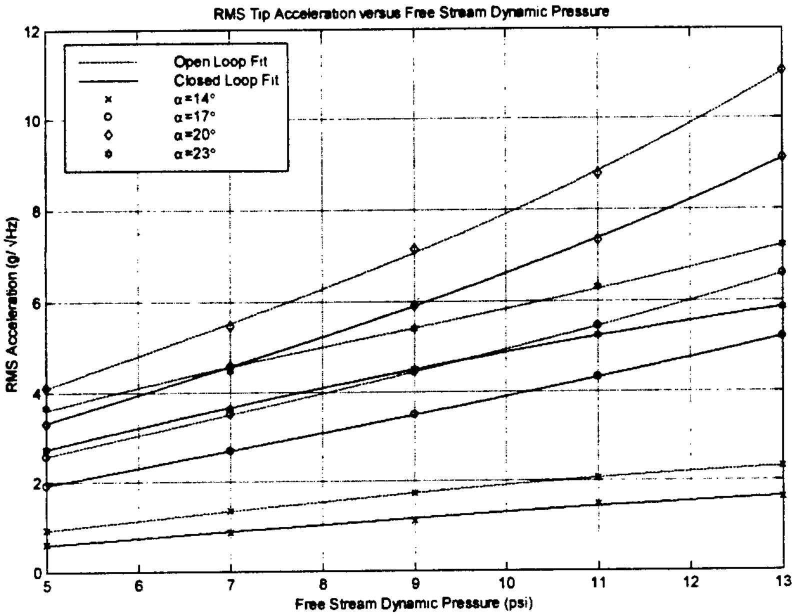

Figure 11.11.20. Uncontrolled and Controlled Root Mean Square of the Trailing Edge Tip Acceleration versus Free Steam Dynamic Pressure for Four Angles of Attack.

Reference:

XI.1 Triplett, W.E., “Pressure Measurements on Twin Vertical Tails in Buffeting Flow”, Journal of Aircraft, V. 20, N. 11, 1983, pp. 920-925

XI.1 Komerath, N.M., Schwartz, R.J. and , Kim, J.M. “Flow over a Twin-Tailed Aircraft at Angle of Attack, Part II: Temporal Characteristics”, Journal of Aircraft, V. 29, N. 4, 1992, pp. 553-558

XII CONCLUSIONS

In this research and development program, we have clearly shown that the tail buffet induced vibrations can be controlled using smart structure concepts. The theoretical and experimental investigations have shown that it is possible to obtain the required control authority for tail buffet alleviation by using piezoceramic stack based actuators. This was accomplished (a) by designing an effective actuator assembly, (b) by developing procedures to optimally place the sensors and actuators on the vertical tail sub-assembly, (c) by designing controllers using acceleration feedback control concepts and (d) by developing procedures to implement these controllers using digital signal processor based systems and specially written algorithms. The effectiveness of multi-mode controllers was validated by (a) testing the full-scale laboratory sub-assembly under excitation provided by a shaker, (b) large deformation control of vibrations by using a structural dynamically similar scale model of the vertical tail sub-assembly and (c) wind tunnel tests on a 1/16th scale model with aeroelastically tailored vertical tail sub-assembly.

Before implementing this development in an operational F-15 and performing flight tests, the following research and development tasks are suggested. Some wind tunnel tests should be conducted to obtain a complete pressure (load) profile of the tail assembly disturbance. This loading should then be used to simulate and optimize further the control of displacements and accelerations in the vertical tail. Tail buffet alleviation controllers should also be designed and validated in a wind tunnel for dynamic maneuver loading. Another important task would be to "scale-up" the control scheme to suppress large deformation vibrations on the full-scale vertical tail sub-assembly of the F-15 aircraft.

Appendix 1: References

[1] Ashley, H., Rock, S.M., Digumarthi, R., Channey, K. and Eggers, A.J., *"Active Control for Fin Buffet Alleviation"*, WL-TR-93-3099, 1994.

[2] Bayon de Noyer, M. and Hanagud, S., *"Single Actuator And Multi-Mode Acceleration Feedback Control"*, Adaptive Structures and Material Systems, ASME, AD, Vol. 54, 1997, pp. 227-235.

[3] Bayon de Noyer, M. and Hanagud, S., *"A Comparison of H_2 Optimized Design and Cross-Over Point Design For Acceleration Feedback Control"*, AIAA/ASME/ASCE/AHS, Struct., Struct. Dyn., Mater., V 4, 1998, pp. 3250-3258, AIAA-98-2091.

[4] Bean, D.E., Greenwell, D.I., and Wood, N.J., *"Vortex Control Technique for the Attenuation of Fin Buffet"*, J. of Aircraft, Vol. 30, N. 6, 1993, pp.847-853.

[5] Bean, D.E., and Wood, N.J., *"Experimental investigation of twin-fin buffeting and suppression"*, J. of Aircraft, v. 33, n. 4, 1996, pp. 761-767.

[6] Ferman, M.A., Liguore, S.L., Smith, C.M., and Colvin, B.J., *"Composite Exoskin Doubler Extends F-15 Vertical Tail Fatigue Life"*, 34th Structures, Structural Dynamics, and Materials Conf., v. 1, 1993, pp. 398-407.

[7] Gee, K., Murman, S. M. and Schiff, L. B., *"Computation of F/A-18 tail buffet"*, J. of Aircraft, v 33, n. 6, 1996, pp. 1181-1189.

[8] Goh, C. J. and Caughey, T. K., *"On the stability problem caused by finite actuator dynamics in the collocated control of large space structures"*, International Journal of Control, Vol. 41, No. 3,1985, pp. 787-802.

[9] Goh, C. J. and Yan, W. Y., *"Approximate Pole Placement for Acceleration Feedback Control of Flexible Structures"*, Journal of Guidance, Vol. 19, No. 1, 1996, pp. 256-259.

[10] Hanagud, S. et al., "F-15 Vertical Tail Modifications: Definition of Design Environment", Final Report, Contract no. F09603-85-G-3104-0030, 1995.

[11] Hauch, R.M., Jacobs, J.H., Ravindra, K., and Dima, C., *"Reduction of vertical tail buffet response using active control"*, J. of Aircraft, v. 33, n. 3, 1996, pp. 617-622.

[12] Hebbar, S.K., Platzer, M.F., and Frink, W.D., *"Effect of Leading-Edge Extension Fences on the Vortex Wake of an F/A-18 Model"*, J. of Aircraft, v. 32, n. 3, 1995, pp 680-682.

[13] Juang, J. N. and Phan, M., *"Robust Controller Designs for Second-Order Dynamic Systems: A Virtual Passive Approach"*, Journal of Guidance, Control and Dynamics, Vol. 15, No. 5, 1992, pp. 1192-1198.

[14] Klein, M.A., and Komerath, N.M., *"Reduction of Narrow-Band Velocity Fluctuation Over an Aircraft Model"*, 15th Applied Aerodynamic Conf., 1997, AIAA 97-2266.

[15] Komerath, N.M., Schwartz, R.J. and , Kim, J.M. *"Flow over a Twin-Tailed Aircraft at Angle of Attack, Part II: Temporal Characteristics"*, Journal of Aircraft, V. 29, N. 4, 1992, pp. 553-558

[16] Lazarus, K.B., Saarmaa, E., and Agnes, G.S., *"Active smart material system for buffet load alleviation"*, Proc. SPIE, v. 2447, 1995, pp. 179-192.

[17] Meyn, L. A. and James, K. D., "*Full-scale wind-tunnel studies of F/A-18 tail buffet*", J. of Aircraft, v. 33, n. 3, 1996, pp. 589-595.

[18] Moore, J.W., Spangler, R.L., Lazarus, K.B. and Henderson, D.A., "*Buffet load alleviation using distributed piezoelectric actuators*", Industrial and Commercial Applications of Smart Structures Technologies, ASME, AD v. 52, 1996, pp. 485-490.

[19] Moses, R.W., "*Vertical-tail-buffeting alleviation using piezoelectric actuators: some results of the actively controlled response of buffet-affected tails (ACROBAT) program*", Proc. SPIE, v. 3044, 1997, pp. 87-98.

[20] Nitzsche, F. ,Zimcik, D.G., and Langille, K., "*Active control of vertical fin buffeting with aerodynamic control surface and strain actuation*", 38th Structures, Structural Dynamics, and Materials Conf., v. 2, 1997, pp. 1467-1477.

[21] Pettit, C.L., Brown, D.L., Banford, M.P., and Pendleton, E., "*Full-Scale Wind-Tunnel Pressure Measurements of an F/A-18 Tail During Buffet*", J. of Aircraft, v. 33, n. 6, 1996, pp. 1148-1156.

[22] Sim, E. and Lee, S. W., *"Active Vibration Control of Flexible Structures with Acceleration Feedback", Journal of Guidance*, Vol. 16, No. 2, 1993, pp. 413-415.

[23] Triplett, W.E., "*Pressure Measurements on Twin Vertical Tails in Buffeting Flow*", Journal of Aircraft, V. 20, N. 11, 1983, pp. 920-925